Controlled Source Audio Magnetotelluric (CSAMT) Surveys in the Tucson Mountains

Geophysics Field Camp 2012
LASI-12-1
May 15, 2012

John B. Fleming

Husna D. Hafit

Khaliza B. Khalid

Jesse G. Martinez

Jonathan A. Powell

Xin Ren

Mohamad Ridzuwan

Ben K. Sternberg

Abstract

Controlled Source Audio-Magnetotellurics (CSAMT) surveys were conducted in 2012 in the Tucson Mountains as a continuation of the 2010 and 2011 Laboratory for Advanced Subsurface Imaging (LASI) field studies in this area. This geologic setting was chosen for its high-resistivity impermeable volcanic layer overlaying porous sedimentary layers. This type of structure has potential for water resources and as a reservoir for compressed air energy storage (CAES). The data from 2,500 meters of CSAMT survey lines generated 900 meter-deep resistivity versus elevation cross-sections and six plan maps of the depth and elevation to the buried conductive layer. Our results are generally in agreement with the geologic cross sections developed by Lipman (1993) and previous TEM data that confirmed the presence of a deep conductive layer beneath a resistive volcanic sequence.

Acknowledgements

Table of Contents

1. Introduction

In the Spring semester of 2012, the GEN/GEOS 416/516 *Field Methods in Geophysics* class performed geophysical surveys in the Tucson Mountains (Figure 1.1 and Figure 1.2). The 2012 surveys are a continuation of previous Controlled Source Audio Magnetotellurics (CSAMT) surveys. Previous GEN/GEOS 416/516 classes have carried out other surveys in this area including: gravity, magnetic, CSAMT, and Transient Electromagnetic (TEM). Collecting the CSAMT data involved running a series of 500 meter long profile lines with a receiver connected to porous pot electrodes at 100 meter intervals and a magnetic-field sensor in the center of each profile. A distant transmitter generates the plane wave that is the signal source for these surveys. A map showing the locations of the transmitters with respect to the receivers is shown in Figure 1.3. Because conductive cultural interference can greatly affect CSAMT data, cultural features have been mapped and plotted in Figure 1.4. Three receiver profile lines were set up in the Tucson Mountains but only two produced usable data. Line 3 was parallel to the eastern most north-south trending steel post barbed wire park boundary fence. Line 3 data were ultimately not used due to the fence's unknown levels of influence on the CSAMT data.

Geophysical data gathered within the Tucson Mountains will be used for studying potential water resources and potential Compressed Air Energy Storage (CAES). Tucson Mountain Park is a Wilderness Area. That means any future drilling for energy and/or water resources must be done outside the park boundaries and horizontally to penetrate beneath the park. In this report we have found evidence that supports the theory that the Tucson Mountains are a result of the movement of the Tucson Mountains from the

summits of the Santa Catalina Range to their present location west of Tucson (McCoy, 1964).

1.1 Geographic Location

The study area is a rectangle with UTM bounds from 3560433N to 3565710N and longitude from 492566E to 497207E. Figure 1.1 shows the study area on a topographic map of the Tucson Mountain and Figure 1.2 shows an orthoimage of the study area.

Survey Map
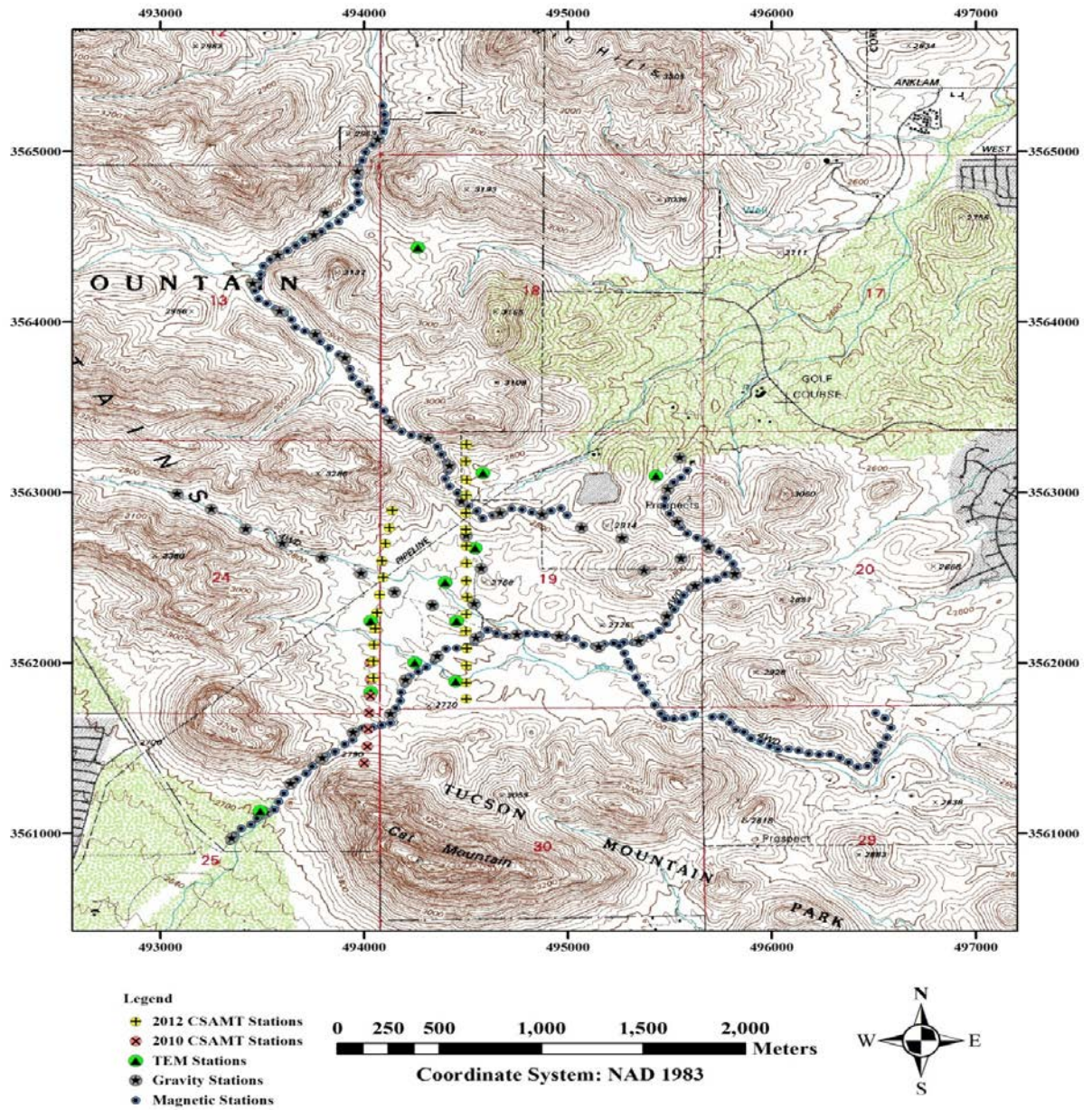
Figure 1.1: Topographic map of the study area with all stations.
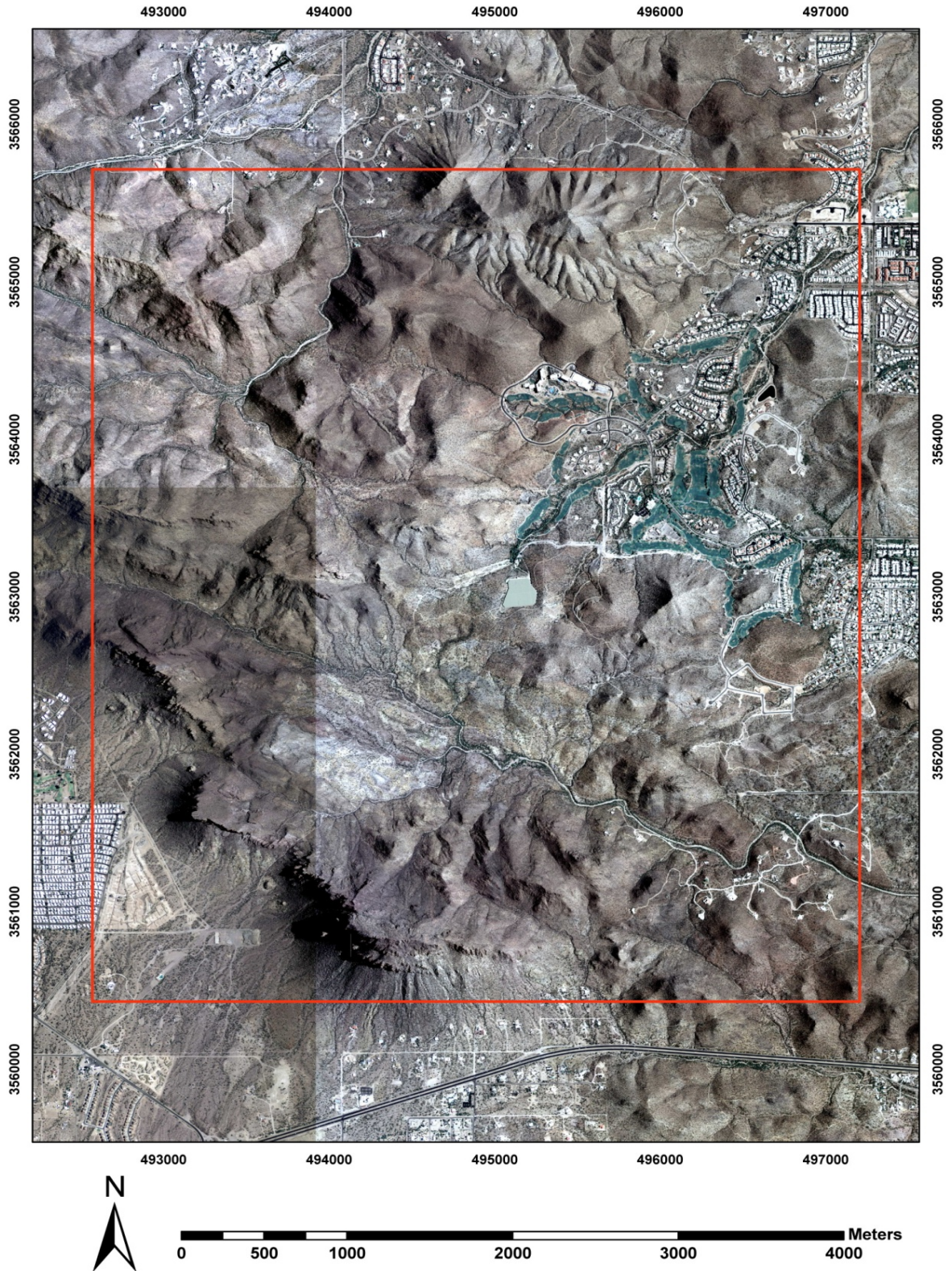
Figure 1.2: The orthoimage of the study area.

Figure 1.3: Transmitter 1 & 2 locations. Image obtained using Google Earth.
Transmitter 2 was used for all the data collected in 2012. Transmitter 1 was used for the
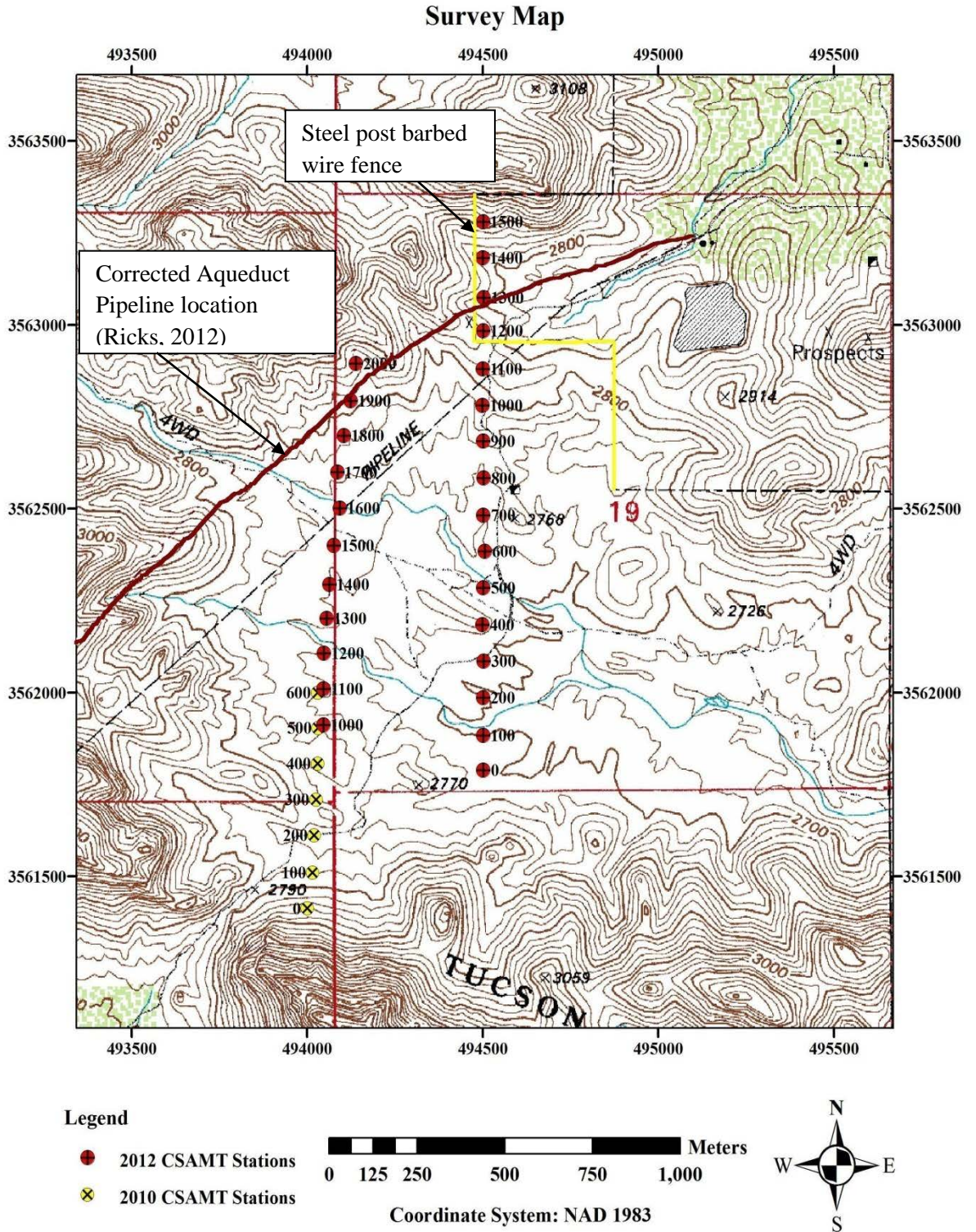2010 data.

Survey Map

Figure 1.4: Cultural Interference along 2012 CSAMT Lines. Interference results from the Tucson Aqueduct Pipeline and Barbed Wired Park Boundary fence.

1.2 The Geology of the Tucson Mountains

The Tucson Mountains are in the Basin and Range Province of the Western United States. This range in Southern Arizona covers an area of approximately 320 km^2. These mountains originally were volcanoes located in the Santa Catalina Range but weathering and block faulting has reduced their height and transferred portions of the ancient rhyolite caldera to the current location of the Tucson Mountains. Tucson Mountain Chaos is a unit of mixed rock sandwiched between the Cretaceous Amole Arkose and the Tertiary Cat Mountain Rhyolite (McCoy, 1964). This chaotic unit was formed during Basin and Range extension. South of Ajo Road it is 3 meters thick, while to the north it is more than 120 meters thick (McCoy, 1964). Block faulting caused the upper rhyolite units containing the ancient caldera to break away from the underlying granite. Basin and Range extension along a detachment fault subsequently moved the Tucson Mountains to their present location, creating the Tucson Mountain Chaos underneath.

The age of volcanism for the Tucson Mountains is in the range of Jurassic to Tertiary-Larimide (Lipman and Sawyer, 1985). The Tucson Mountains are now separated from neighboring ranges by basins that are filled with alluvium which has been weathered from the ancient peaks. The composition of the Tucson Mountains is dominantly volcanic with rhyolite being the most common igneous rock mapped (Lipman, 1993).

The main geologic units exposed in the area of the Tucson Mountains, summarized from Lipman, 1993, are from youngest to oldest (Figure 1.5 and 1.6):

A) **Quaternary alluvium (Qal, Qf)**: Correspond to gravel, sand, and silt filling the bottom and the slopes of the valleys. This unit includes alluvial-fan, alluvial and colluvial sedimentary deposits.

B) **Tertiary volcanic and intrusive rocks (Tv, Ti)**: This sequence includes erosional remnants of a dacitic volcanic field in the northern Tucson Mountains, a stratified sequence of basaltic andesitic lavas and rhyolitic tuff along the east edge of the area, a dacitic-rhyolitic lava dome cluster along the south edge of the map area and small dikes and irregularly shaped small intrusions.

C) **Caldera-fill volcanic rocks (TKv, Kv)**: These units correspond to an interleaved caldera-filling mafic to silicic lava flow, tuffs and volcaniclastic sediments, preserved mainly in the southeastern and northern flanks of the Tucson Mountains. The southeastern rocks are considered younger than those in the northern flank on the basis of potassium-argon (K-Ar) dates.

D) **Caldera-related Intrusions (Tki, Kg)**: Dikes, sills, small regular intrusions that range in composition from andesitic to silicic dikes, and the large granodioritic-granitic Amole pluton in the northern Tucson Mountains, which are considered to be associated with magmatic resurgence of the caldera and post-caldera volcanism.

E) **Cretaceous Cat Mountain Tuff (Kc, Kcm)**: This is the main volcanic unit and corresponds to a thick intracaldera rhyolitic ash-flow tuff (72-74% of SiO_2) that varies greatly in welding and crystallization character laterally and vertically. This unit interfingers complexly with multiple horizons of lenticular and more irregular masses of chaotic mega-breccia. The tuff contains 10-30% phenocryst of quartz, altered feldspar,

and biotite. The total thickness of the Cat Mountain Tuff, including the interleaved breccias, increases from only about 100 m in the southernmost part of the area to at least 4 to 5 km in the northern part of the mountain range.

F) **Other Cretaceous rocks (Ks, Ktc)**: Corresponds to stratigraphically coherent pre-caldera Cretaceous rocks, which include a crystal-rich, gray welded rhyolitic tuff and a sedimentary package composed of siltstone, conglomerate and volcanic sandstones.

G) **Jurassic and Triassic sedimentary and volcanic rocks (JT)**: This package includes interleaved red-brown sandstone and siltstone, dark-red-brown conglomerate containing abundant andesitic detritus, a basalt flow, and two rhyolithic ash-flow sheets.

H) **Paleozoic-sedimentary rocks (Pz)**: Occur as clasts of limestone, dolomite, sandstone and quartzite in the mega-breccia member of the Cat Mountain Tuff.

Precambrian rocks (pC): Occur as clasts in the mega-breccia in the Cat Mountain Tuff, and are mainly composed of muscovite-bearing granites with potassium feldspar, and quartz-sericite schist.
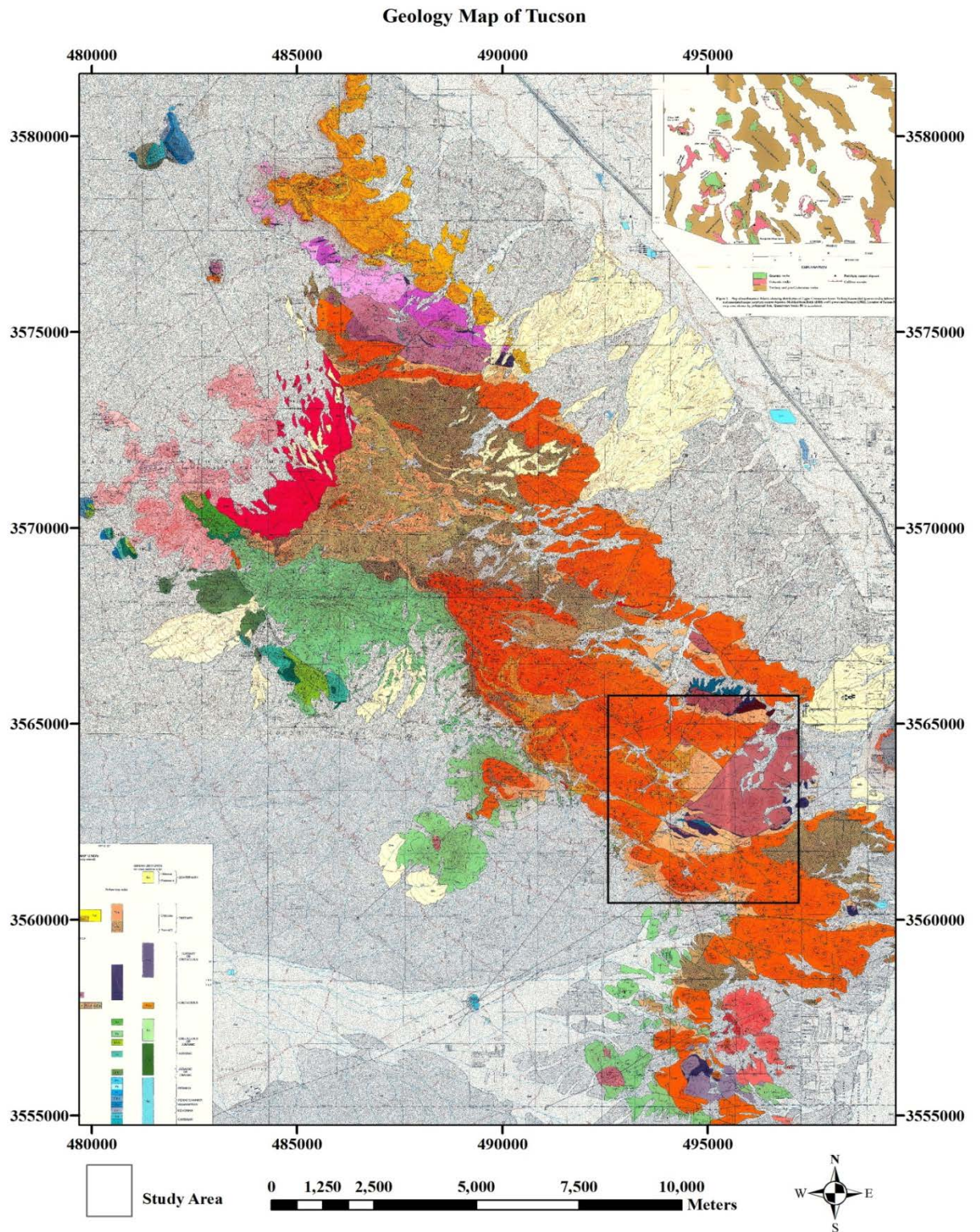
Figure 1.5: Geologic Map of the Tucson Mountains Caldera, Southern Arizona.

U.S. DEPARTMENT OF THE INTERIOR
U.S. GEOLOGICAL SURVEY

LIST OF MAP UNITS

SURFICIAL DEPOSITS

Qal	Alluvium (Holocene)
Qc	Colluvium (Holocene)
Qf	Alluvial-fan deposits (Holocene and Pleistocene)
Qfo	Older alluvial-fan deposits (Pleistocene and older?
Qu	Quaternary deposits, undivided

MIDDLE TERTIARY ROCKS (MOSTLY OLIGOCE

Intrusions

Tai	Intrusive andesite
Tdi	Intrusive dacite
Tri	Intrusive rhyolite

Volcanics of Tumamoc Hill

Tba	Basaltic andesite
Tr	Rhyolitic ash-flow tuff
Tdr	Dacitic-rhyolitic lava flows

Safford Dacite

Tsf	Lava flows
Tsv	Vent intrusions
Tss	Vent spatter

Volcaniclastic deposits

Tst	Tuffaceous rocks
Tsm	Mudflow deposits
Tvs	Volcaniclastic sedimentary rocks
Tc	Tertiary colluvium (Oligocene and Eocene?)

Intrusions

Dikes and irregular intrusions

TKai	Andesite
TKap	Porphyritic andesite
TKs	Porphyritic silicic dikes
Kgp	Porphyritic granodiorite

Amole pluton

Kaa	Aplite
Kag	Granite
Kad	Granodiorite

Postcollapse volcanic rocks

Southeastern postcollapse volcanics

TKb	Tuff of Beehive Peak
TKbi	Vent intrusion
TKa	Andesite of John F Kennedy Park
TKd	Dacite of Twin Hills
TKdl	Lower flow
Kab	Andesite of Bilby Road

Volcanics of Yuma Mine

Kyap	Porphyritic andesite
Kya	Aphanitic andesite

Aphanitic rhyolite and dacite

Kyr	Flow
Kyrb	Flow breccia
TKvs	Volcaniclastic sedimentary rocks
TKv	Postcollapse volcanic rocks, undivided

Caldera-forming rocks

Cat Mountain Tuff

Kci	Intrusive rhyolitic tuff
Kcw	Densely welded rhyolite
Kcp	Partly welded rhyolite
Kcn	Nonwelded to partly welded rhyolite

Megabreccia member [1]

Kcm	Megabreccia, undivided
Kcmt	Megabreccia, mainly clasts of Cretaceous tuff of Confidence Peak
Kcma	Megabreccia, mainly clasts of Cretaceous(?) andesite and dacite
Kcms	Megabreccia, mainly clasts of Cretaceous sedimentary rocks
Kcmg	Megabreccia, mainly clasts of Jurassic-Cretaceous Glance Conglomerate
Kcmr	Megabreccia, abundant clasts of Jurassic(?) flow-layered rhyolite
Kcmb	Megabreccia, abundant clasts of Jurassic or Triassic Recreation Red Beds
Kcmp	Megabreccia, abundant clasts of Paleozoic sedimentary rocks
Kcu	Cat Mountain Tuff, undivided

PRECALDERA ROCKS

Cretaceous rocks

Ks	Sandstone and shale (Upper Cretaceous)
Ktc	Tuff of Confidence Peak (Upper Cretaceous)
Kb	Amole Arkose (Cretaceous)
KJvc	Volcanic conglomerate (Lower Cretaceous? or Jurassic)
Ku	Cretaceous sedimentary rocks, undivided

Jurassic and Triassic(?) rocks

Ja	Andesite porphyry (Jurassic)
Jt	Rhyolite ash-flow tuff (Jurassic?)
Js	Sandstone (Jurassic?)
Jlt	Lithophysal ash-flow tuff (Jurassic?)
Jb	Basaltic lava flow (Jurassic?)
JTr	Recreation Red Beds (Jurassic or Triassic)
JTu	Jurassic and Triassic(?) sedimentary rocks, undivided

Paleozoic sedimentary rocks

Prv	Rainvalley(?) Formation (Permian)
Pc	Concha Limestone (Permian)
Ps	Scherrer Formation (Permian)
PPh	Horquilla Limestone (Permian and Pennsylvanian)
Me	Escabrosa Limestone (Mississippian)
Dm	Martin Formation (Devonian)
Ca	Abrigo Formation (Cambrian)
Cb	Bolsa Quartzite (Cambrian)
Pau	Paleozoic sedimentary rocks, undivided

Precambrian rocks

Yg	Porphyritic granite (Middle Proterozoic)
Xp	Pinal Schist (Early Proterozoic)
pCu	Precambrian rocks, undivided

Contact—Long dashed where approximately located, short dashed where gradational. Where contact is indefinite, no line is shown between map units

Unconformity along the Tucson Mountains caldera wall and floor—Dashed where approximately located; dotted where concealed or occupied by intrusive rocks

Quartz vein

Fault—Dashed where approximately located; dotted where concealed or occupied by intrusive rocks; queried where inferred. Bar and ball on downthrown side

Approximate limit of contact-metamorphic hornfels—Shown on cross section only

Quaternary block slump—Hachures on downthrown side

Strike and dip of bedding
25   Inclined

Vertical

Horizontal

Strike and dip of foliation and flow layering in volcanic rocks
30   Inclined

Vertical

Horizontal

15   Direction and strike of flow lineation (elongate pumice in welded tuff)

159±0.5   K-Ar Sample locality—In millions of years (Bikerman and Damon, 1966; ages recalculated to current IUGS constants)

60.8±0.2 $^{40}Ar/^{39}Ar$ Sample locality—In millions of years (L.W. Snee, unpub. data, 1991)

[1]Conspicuous megablock of Kcmt, Kcma, Kcms, Kcmg, Kcmr, Kcmb, or Kcmp shown by symbol t, a, s, g, r, b, or p, respectively, within other megabreccia subunits.

Figure 1.6: Legend of Geologic Map
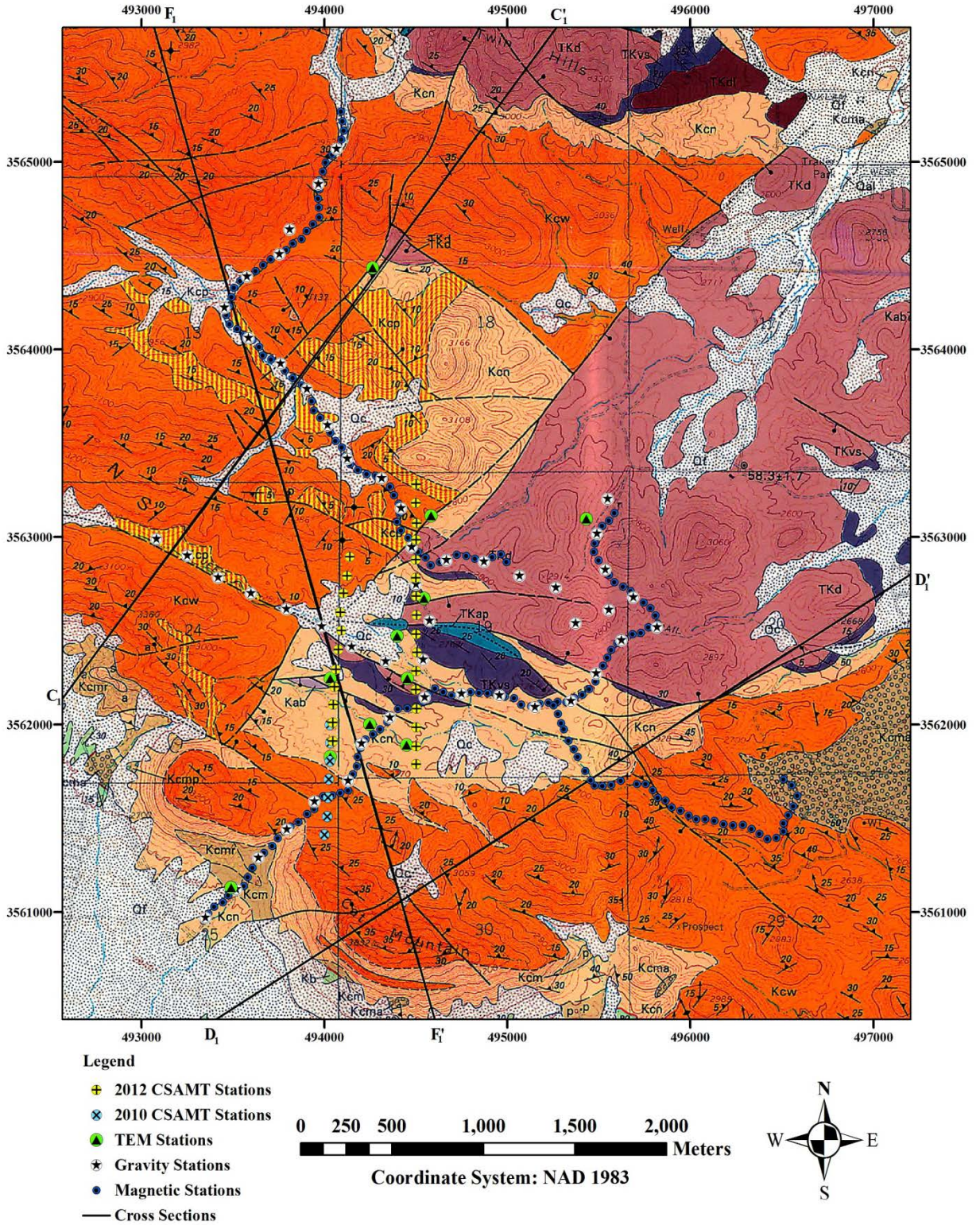
15

Survey Map

Figure 1.7: Positions of all stations within study area on the geologic map.

2. Controlled Source Audio Magnetotelluric (CSAMT) Method

CSAMT is a low-impact, non-intrusive, surface-based geophysical method which provides resistivity information about the subsurface. The CSAMT method involves transmitting a controlled signal over a range of frequencies into the ground from a transmitter site at one location, and measuring the received electric and magnetic fields at the receiver site in the area of interest. The ratio of horizontal electric field (Ex) and orthogonal magnetic field (Hy) are used for calculating the resistivity structure of the earth. The resistivities calculated from scalar CSAMT data are affected by the pore fluids and sediment porosity under the ground. More details of the CSAMT method can be found at the Zonge International website:

http://www.zonge.com/PDF_Papers/Intro_CSAMT.pdf.

For this work, the electric fields (Ex) were measured using 100-meter receiver dipoles, and the magnetic field (Hy) was measured using a single orthogonal magnetic field coil.

The laboratory for Advanced Subsurface Imaging (LASI), in conjunction with Zonge International, Inc., acquired Controlled Source Audio Magnetotelluric (CSAMT) data along two lines; a 1000-meter transect (Line 1) and a 1500-meter transect (Line 2) in the Tucson Mountains. Figures 2.1 and 2.2 show the location of the survey transects, and Tables 2.1, 2.2 and 2.3 show the station coordinates. The survey results mainly depend on the signal frequency (which is related to depth) and on the subsurface resistivity. In general, when the signal frequency is lower, the depth of investigation is greater, and when the frequency is higher, the depth of investigation is reduced. For this work, the maximum depth of investigation is about 100 m below sea level.

Survey Map
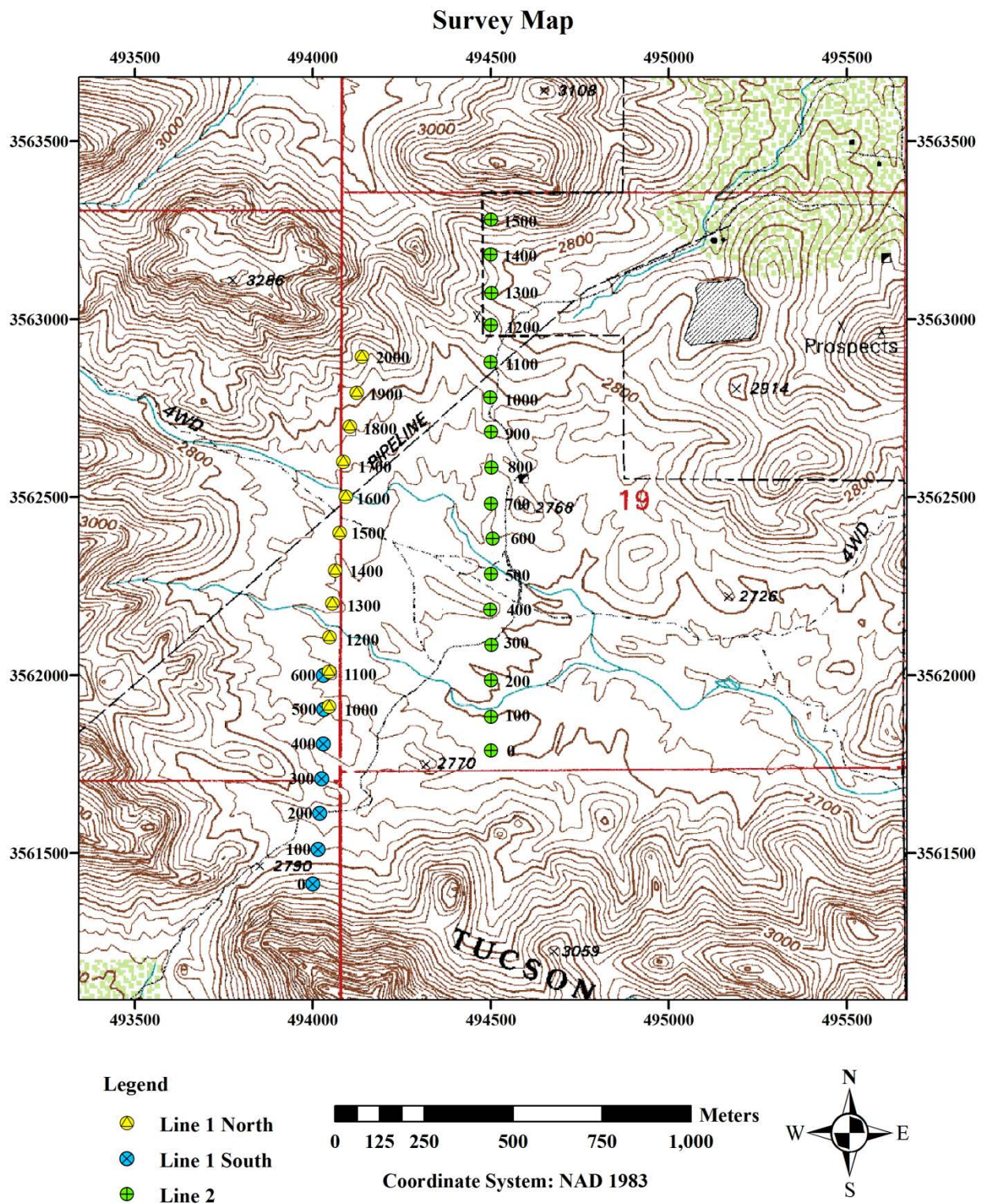
Figure 2.1: Location of CSAMT stations overlaid on top of the local topographic map of Tucson.

Survey Map
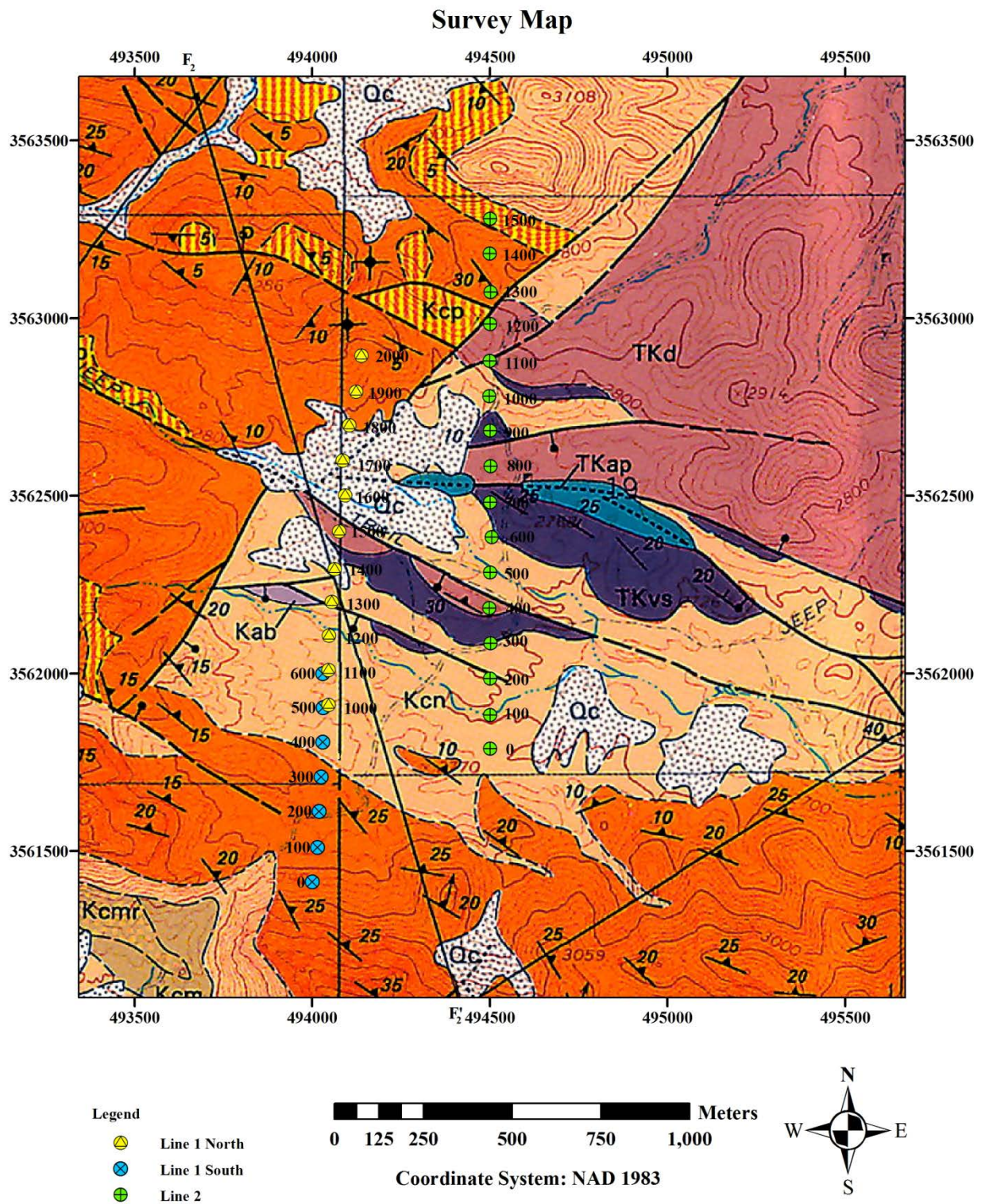
Figure 2.2: Location of CSAMT stations overlaid on top of geological map of Tucson Mountain.

Station No.	Easting	Northing	Elevation
1000	494046	3561912	837
1100	494046	3562010	837
1200	494048	3562107	833
1300	494055	3562202	833
1400	494063	3562294	835
1500	494076	3562400	845
1600	494093	3562501	844
1700	494086	3562599	849
1800	494105	3562699	845
1900	494124	3562793	852
2000	494139	3562895	864

Table 2.1: Station coordinates and elevation for Line 1 North.

Station No.	Easting	Northing	Elevation
0	494001	3561413	871
100	494016	3561511	848
200	494025	3561612	840
300	494026	3561706	842
400	494034	3561808	841
500	494030	3561900	840

Table 2.2: Station coordinates and elevation for Line 1 South (2010 Fieldwork)

Station No.	Easting	Northing	Elevation
0	494502	3561789	829
100	494501	3561883	827
200	494501	3561986	821
300	494503	3562085	830
400	494499	3562185	839
500	494502	3562285	830
600	494506	3562384	830
700	494502	3562482	837
800	494503	3562583	837
900	494501	3562684	844
1000	494499	3562781	854
1100	494500	3562880	861
1200	494501	3562984	863
1300	494503	3563074	860
1400	494500	3563182	860
1500	494501	3563280	881

Table 2.3: Station coordinates and elevation for Line 2

3. Hardware

This description of the operation of the CSAMT system is adapted from the Zonge International website and the details can be found at http://www.zonge.com/Equipment.html . At the transmitter site, insulated copper wires (14 Gauge) were grounded at each end to electrodes about 700 m apart. The electrodes consisted of electrical conduit and were pounded about 0.20 m - 0.40 m into the soil. The electrodes were then watered to decrease the contact resistance between the stakes and the ground. The copper wires were connected to the transmitter electronics. The Zonge GGT-30, current controlled transmitter, is capable of 30 kW of power output and was powered by a Zonge ZMG-30D diesel-powered motor generator. The Zonge XMT-32 was used as a transmitter controller. The CSAMT transmitter was located along a line 75° West of true North, at a distance of 8390 m from Line 1 and 8870 m from line 2. The transmitters were located at 32° 13' 14.07" N, 111° 08' 53.00" W and 32° 12' 50.53" N, 111° 08' 52.84" W.

At the receiver site, a Zonge GDP-32-II receiver was used to digitize and process the received signals from the transmitter. The 100 m dipoles were connected to ground at each end through non-polarizing electrodes. The non-polarizing electrodes use ceramic pots that were buried about 0.01 m in the soil and water added to the surrounding soil. Prior to transmission, the timing for the transmitter controller and the receiver were synchronized to provide an absolute phase reference for the survey. An RF filter was used to reduce interference. The Zonge ANT/6 magnetic field sensors are cylindrical coils with copper wire wound around a high-permeability core. These coils were placed on the ground, perpendicular to the grounded dipoles, and 15 m away from it.

4. Data Processing and Interpretation Programs

4.1 Programs

The CSAMT data obtained from the surveys were stored in the GDP32-II receiver and then downloaded and saved in its raw form, on a laptop computer. The raw data were stored and organized in preparation for processing using Zonge International's proprietary software, CSAVGW, SCS2D, and MODSECT, which produces the format required for Golden Software's Surfer program to render cross-sections depicting contours of the subsurface resistivity versus depth. The following sections describe each program used in this study. The information regarding each program's operations are adapted from Zonge International's website, http://zonge.com/DataPrograms.html, and Golden Software's website for the Surfer gridding and contouring program, http://www.goldensoftware.com/products/surfer/surfer.shtml.

4.2 CSAVGW v1.10t Processing

Raw data for each line (Line 1 North, Line 2) are compiled into respective continuous data sets creating one raw data file per line (.raw file). For each raw data set, a Station File (.stn) is created containing the GPS locations of each Porous Pot (POT). Dipole locations are assigned to the center of each POT interval. Each line file is trimmed or edited to remove values that have large statistical errors found by the CSAVGW software's statistical analysis software suite and, including the judgments by the data processor that were identified as being inconsistent with the trend. The result is a set of average apparent resistivity and impedance phase values for each transmitted frequency.

Figures 4.1 and 4.2 are examples of typical and anomalous data sets from all our collected data.

Figure 4.1 shows a typical dipole trend from our viable data, Line 2 Dipole 450. For each frequency transmitted, the receiver detects a fundamental frequency as well as multiple harmonics. This study typically used the fundamental frequency and the 3rd and 5th harmonic for each dipole.

The trend of the apparent resistivity curve reflects the resistivity of the subsurface structure. In general, we expect a low-resistivity, shallow alluvium layer at the surface, a highly resistive layer (volcanics), followed by deeper less-resistive sedimentary layers.

Figure 4.2 is an example of four anomalous trends from the northern section of Line 2, representing dipoles 1150 through 1450. Field notes from a follow-up cultural feature survey on 4/7/12 identified cultural features in the area including a 1.2 meter tall grounded barbed wire fence parallel to a portion of Line 2. The fence's location and orientation have been surveyed and confirmed, using GPS, to be parallel to the line and 23 meters due west. Across from Line 2 Dipole 1150, the fence becomes perpendicular and continues east. We also found that the actual position of the pipeline in this area that is plotted on USGS topo maps appears to be incorrect. After extensive consultation with the Bureau of Reclamation, we were able to determine the true position of the pipeline. The pipeline is constructed from concrete reinforced with steel rebar, surrounded by a steel liner (Ricks, 2012).

The data and 2D inversion modeling results from Line 3 were excluded from interpretation due to similar cultural interference. Three hundred meters of this single,

500-meter receiver line was parallel and 27 meters to the east of another north-south section of the steel post barbed wire fence. Also, the northern most dipole was within range to suspect interference. This environment was deemed not appropriate for CSAMT surveying. See Figure 1.4 for position of Line 2 dipoles, the pipeline, and the two north-south sections of the steel post barbed wire fence.
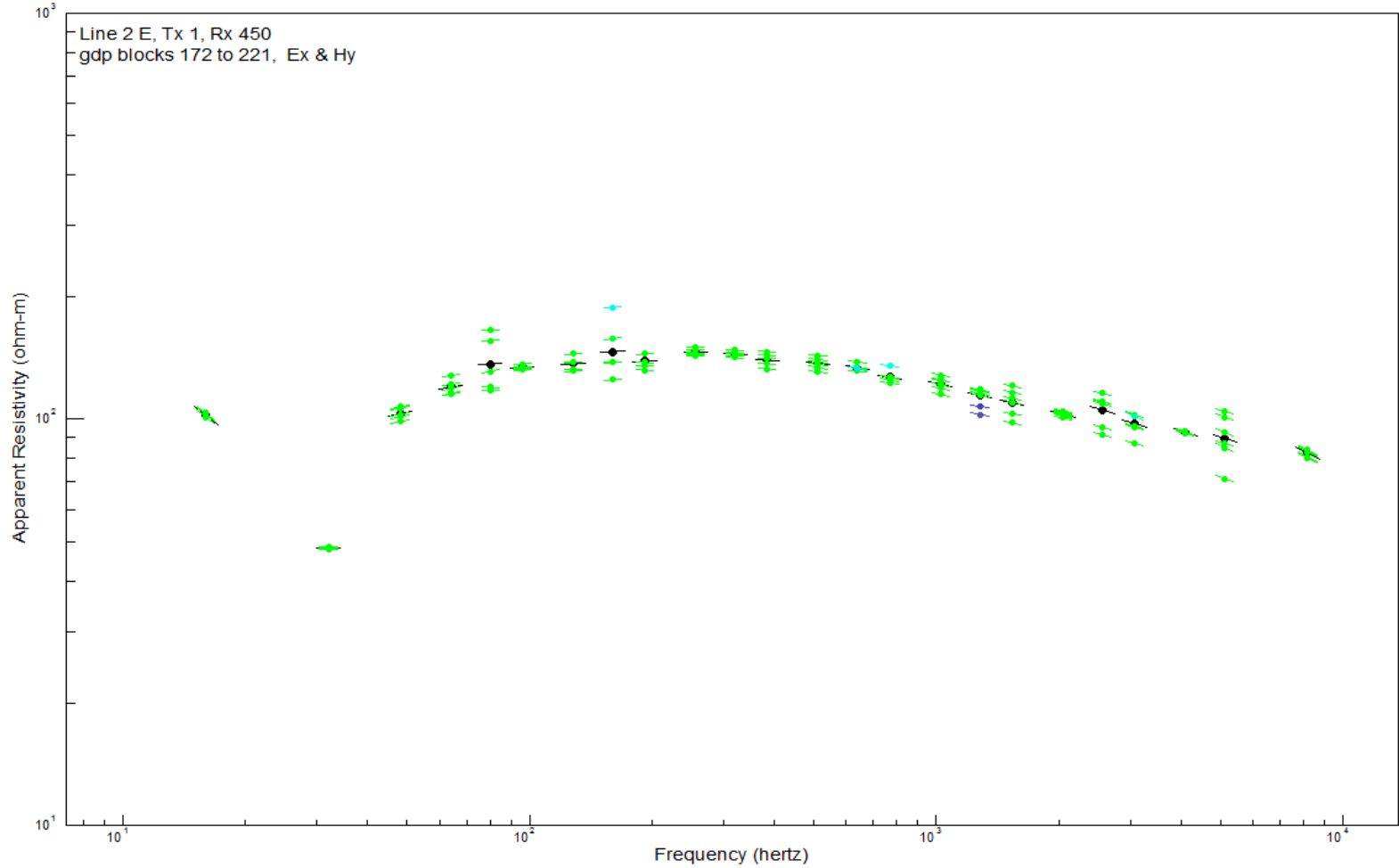
Figure 4.1: Line 2 Dipole 450, is an example of a typical concave down, dome-like trend from our data set. This matches our expectation of higher apparent resistivity layers bound above and below by lower resistivity layers. Frequency is inversely related to the depth of investigation.
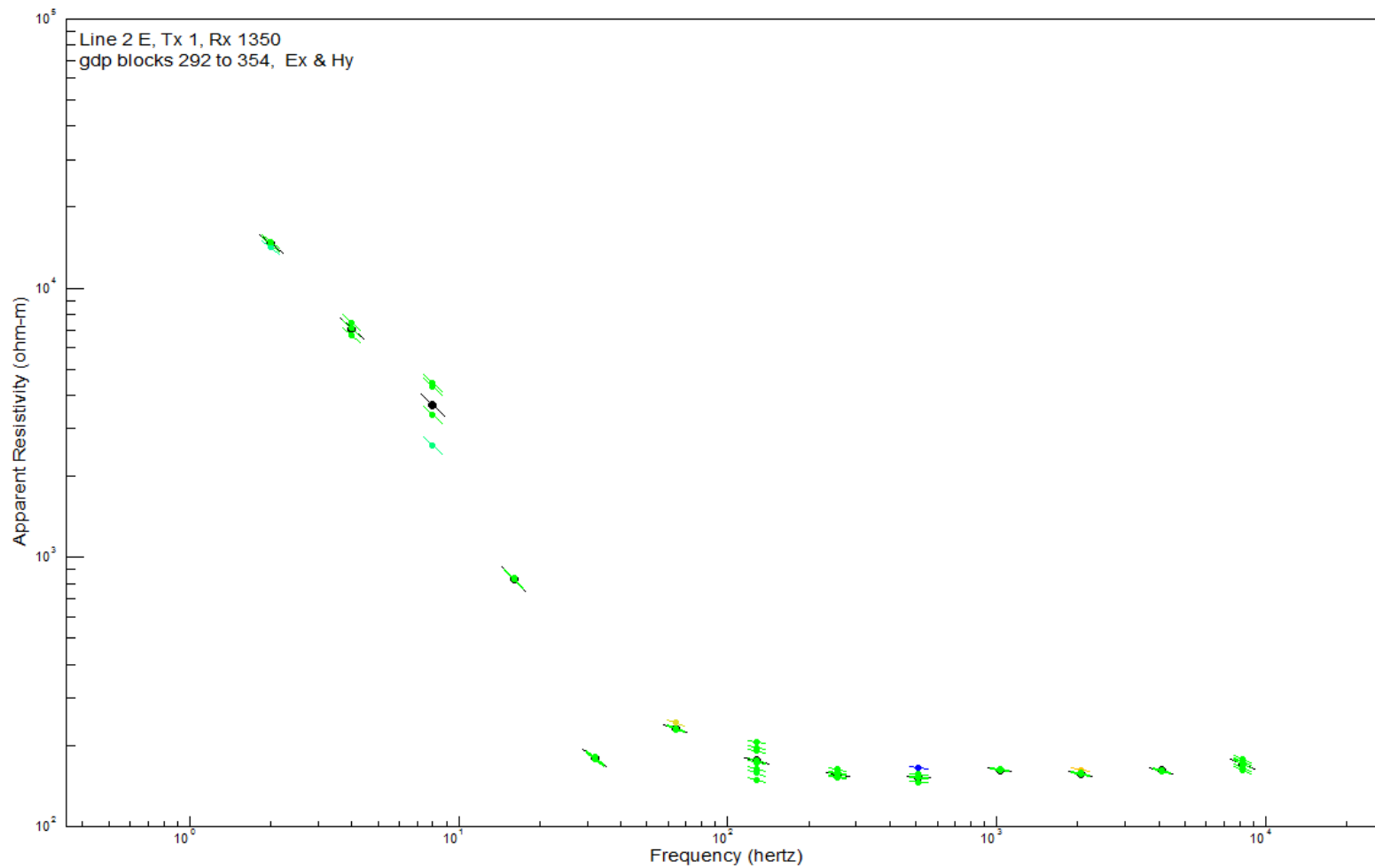
Figure 4.2: Line 2 Dipole 1350 is characteristic of the anomalous dipole trends present in dipoles 1150-1450, which was interpreted as interference from a parallel steel post barbed wire fence, 23 meters due west. This resulted in the exclusion of those dipoles from the data set.

Notable data point omissions include: typically the two or three data points from the highest frequencies of each dipole were eliminated due to their poor correlation with the overall dipole trend. We believe this is reasonable because the higher frequencies mainly resolve the surface alluvium, which is above the resistive volcanic layers and is not the focus of our study. Also, Line 1 Dipoles 1650 (Appendix 4.8) and 1750 (Appendix 4.9) were largely edited due to the sharp steps in apparent resistivity, again at the high frequencies.

All CSAMT data collected and processed in this study were collected with the GDP-32II outfitted with an RF filter. This was in response to initial incoherent data collected along Line 1, on 01/21/2012. Figure 4.3 shows the raw data prior to installation of the RF filter collected on 01/21/2012. Figure 4.4 shows our raw data from the same dipole location after the installation of the RF filter, which was collected the following day, 01/22/2012. The horizontal axis (Frequency) for the collected data without the RF filter is automatically plotted longer by the Zonge software due to the large range of values on the vertical axis (Apparent Resistivity). The raw apparent resistivity versus frequency data plots for each dipole interpreted in this study is attached in the appendix (Appendix 4.1-4.25).
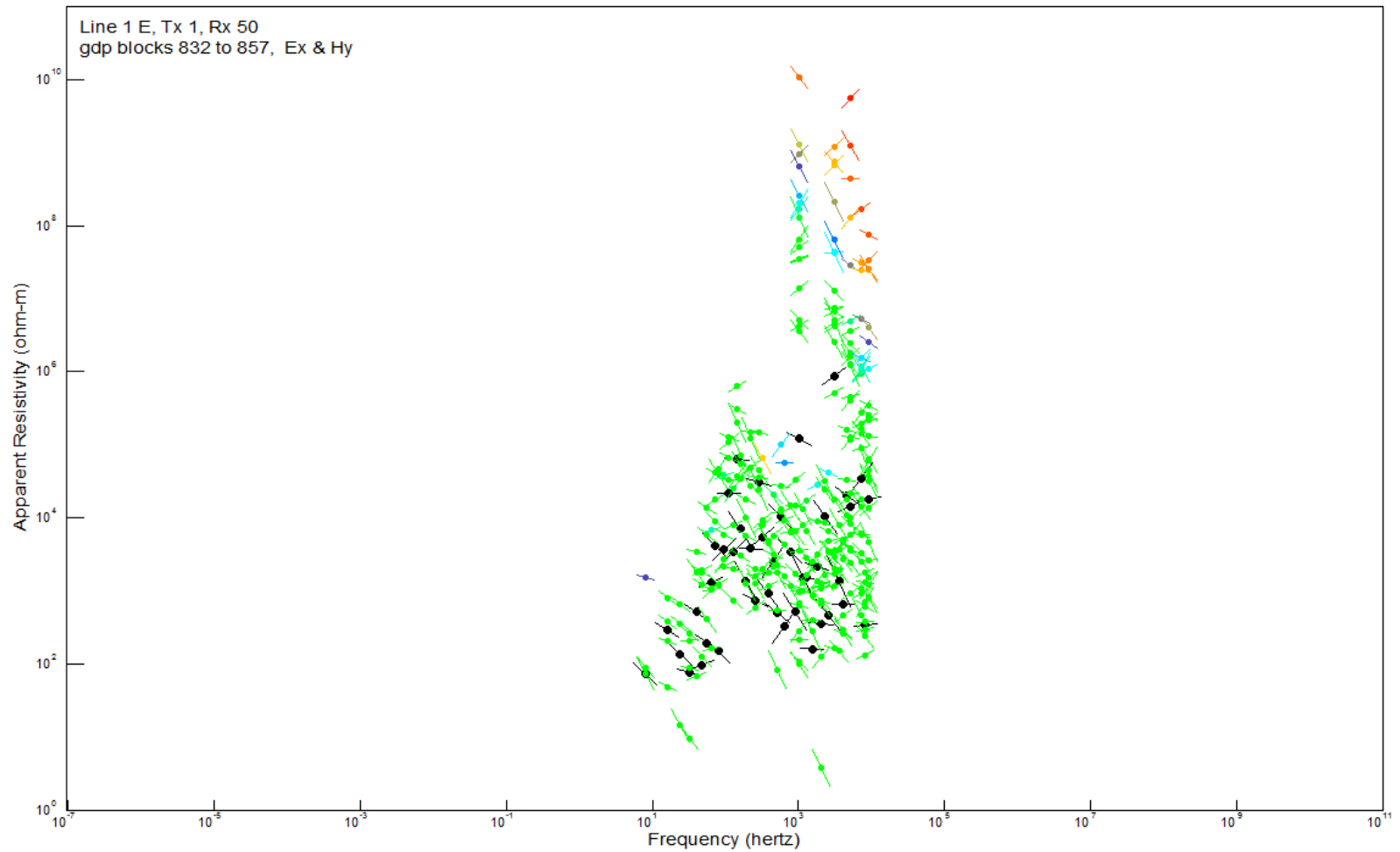
Figure 4.3: Raw Line 1 CSAMT data collected prior to the installation of an RF filter on the GDP-32 II receiver. Line 1 was re-surveyed using the same Dipole locations with an RF filter installed on the GDP 32-II (See next Figure). These data correspond to Dipole 1050 (Appendix 4.3). Scatter range: 50-10,000,000,000 Ohm-m.
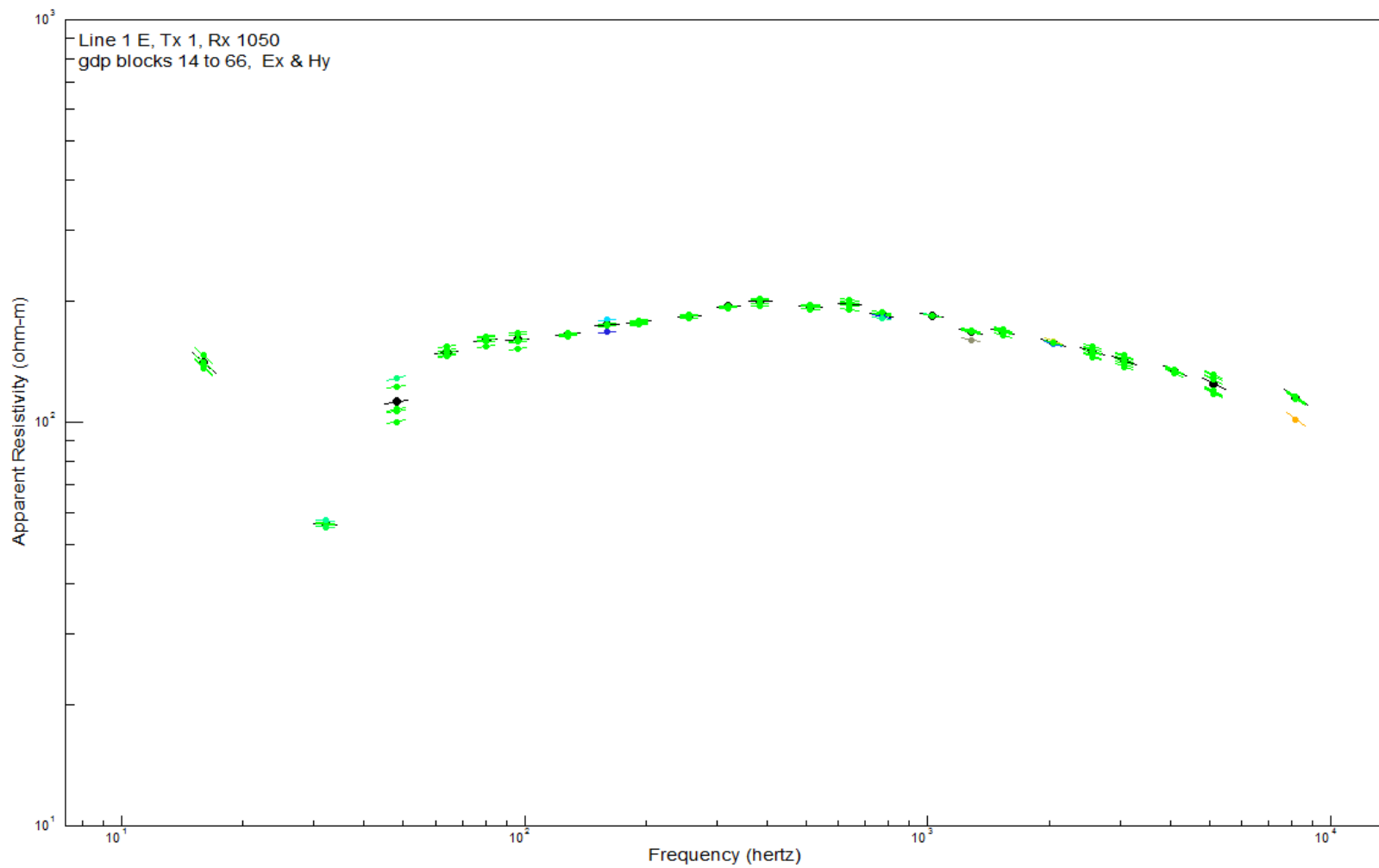
Figure 4.4: Line 1 raw sounding data, observing up to the 5th harmonic. Dipole 1050. This data set location is the same as in Figure 4.3, but with an RF filter installed. Scatter range: 15-1000 Hz and 40-200 Ohm-m.

4.3 SCS2D v3.30a Inversion Modeling

The resultant processed data (.avg file format), produced by the CSAVGW program, are then inverted to a Resistivity versus Depth model cross-section using SCS2D, a two-dimensional, smooth-model inversion program developed by Zonge International. SCS2D iteratively modifies the model-section-pixel resistivities until the apparent resistivity and impedance phase model becomes as close as possible to the measured data, given our pre-set deviation constraints for the model. Pre-set constraints include a background-model constraint, which constrains the deviation between the background model and inversion model, and a smoothness constraint, which constrains the pixel-to-pixel contrast in resistivity. The SCS2D program assigns initial constraints based upon the averaged data. The constraints for Line 1 North and Line 2 were manually set to be identical. Background-model deviation was set to "Low-variance," which biases the model towards the observed resistivity instead of an artificially smooth model. Averaged data were then inverted using the Bostick inversion method for resistivity versus depth. For each model pseudo cross-section, the SCS2D program calculates apparent resistivity and impedance phase using a 2-dimensional, finite-element algorithm to calculate the far-field CSAMT data.

We did not provide preliminary information regarding any known geologic structure to our model. The smooth-model automatically transforms the observed data to a resistivity model cross-section providing an image of the subsurface. The SCS2D program produces .mtm and .mtd files, which are compatible with the Zonge contouring program, MODSECT.

Included in the Appendix (Appendix 4.27-4.53, except 4.37) are the results from the SCS2D program for each dipole of Line 1 North and Line 2, including depiction of the omitted high-frequency data points and the best-fit model calculation. The slight variances in the finite-element model's best-fit model calculation is most likely due to the nature of smooth modeling, where the character of each dipole has an influence upon all other dipoles with varying strength depending upon the proximity to each other. Line 1 North and Line 2 inversion pseudo cross-sections are included (Appendix 4.26 and 4.37 respectively).

4.4 MODSECT v4.41q Contour Data Set

Utilizing Zonge's MODSECT program, which is designed to read Zonge inversion-model-section resistivity program files, .mtm and .mde produced by SCS2D, we created color-filled-contour plots for each line. Due to the flexibility and simplicity of Golden Software's Surfer program, we exported the MODSECT XYZ-data as script files, which are compatible with the Surfer program, from which we made our interpretations.

4.5 Golden Software Surfer v8.05 Contour Plot

Surfer software was used to create a contour map by interpolating between XYZ spatial data for the resistivity versus depth along Line 1 North and 2, as modeled by SCS2D and smoothed by MODSECT. We also used Surfer to grid and contour a plan map for our apparent resistivity inversion results from each line and, to model the upper and lower contact surfaces of the conductive layer between the resistive capping layer and underlying resistive layers, Figures 6.19 through 6.24.

5. Interpretation of CSAMT Data

5.1. Introduction

The CSAMT data from 2010, labeled as Line 1 South is used to interpret the conductive and resistive boundaries. It is also used to match with Line 1 North, produced from the CSAMT data in 2012. The resistivity cross sections for Line 1 South and North are compared with the Lipman geologic cross section F_1-F_1'(Lipman, 1993). Since the geologic cross section is not perfectly parallel with Line 1 South and North, a 90° projection from line 1 to the F_2-F_2'cross section line is made. For Line 2, only the first three stations are projected to the geologic cross section because the other stations are too far from F_2-F_2' cross section, and the distribution of the geologic units observed on the surface is also different (Figure 5.1). The geologic map (Lipman, 1993) is also used for interpreting fault location.
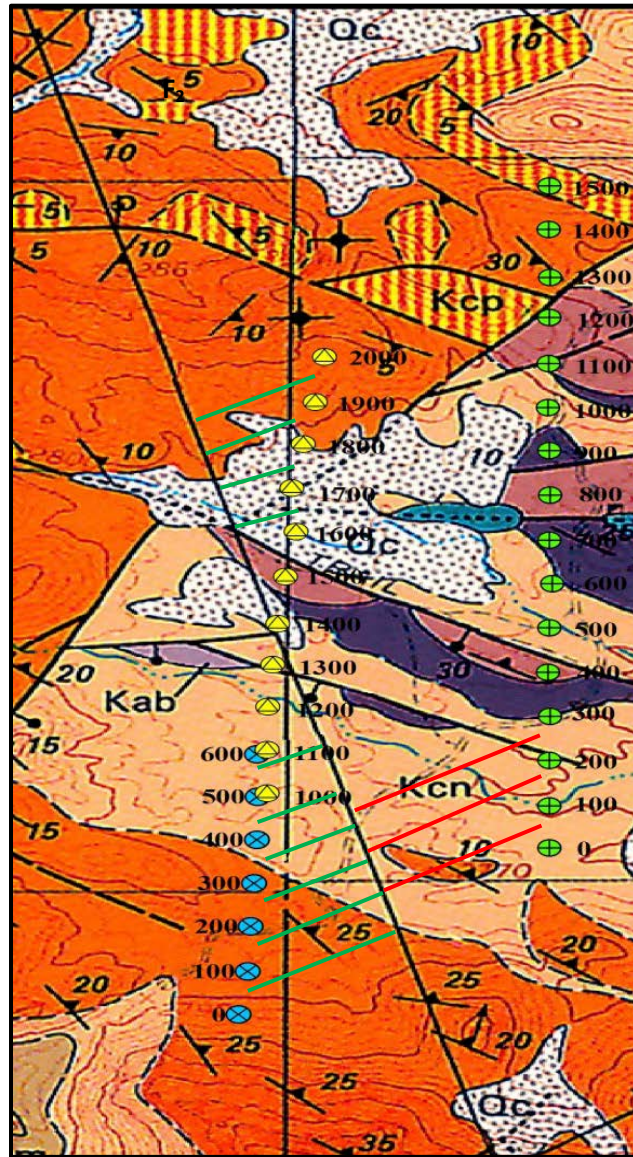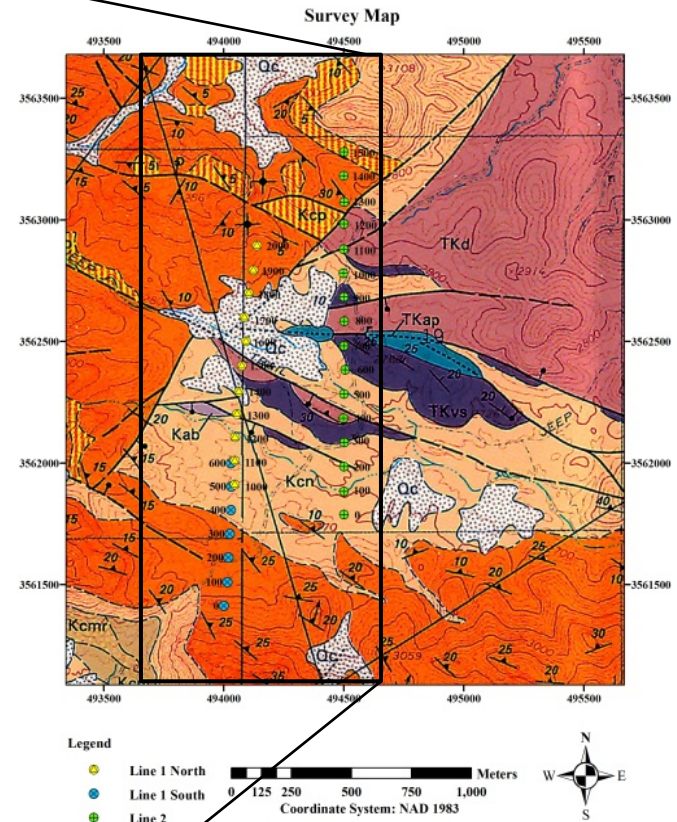
Figure 5.1: The zoomed geologic map shows the CSAMT stations for Line 1 and Line 2. The 90° projections from the stations to the F_2-F_2' cross section are shown.

5.2. Line 1 South

The resistivity cross section of Line 1 South is reproduced from the 2010 data. The value of the resistivity used for the boundary between conductive and resistive layers is chosen as 100 Ohm-m. This is because 100 Ohm-m falls in the transition range between volcanic rocks and sedimentary rocks as shown in Figure 5.2 and the expected resistivity of water-saturated rocks of this type is in the range of 10-100 Ohm-m (Loke, 1999).

The depth to the conductive layer at the north end ranges from 400m to 500m. The depth range of the boundary at the south end is ranging from 300 m to 400 m. The increase in depth from south to north agrees with the dip shown in geologic cross section F_1-F_1'. Figure 5.3 suggests that Kcw (densely welded rhyolite) is the most resistive layer and Ku (Cretaceous sedimentary rocks undivided) is the most conductive layer. The resistivity for Kcn (non-welded to partly welded rhyolite), Kcp (partly welded rhyolite), Kcm and Kcmr (Megabreccia members) fall between Kcw and Ku. In general, the resistivity cross section agrees with the geologic cross section, F_1-F_1' interpreted by Lipman. The impermeable volcanic layer with high resistivity sits on top of the low resistivity, permeable sedimentary layer.
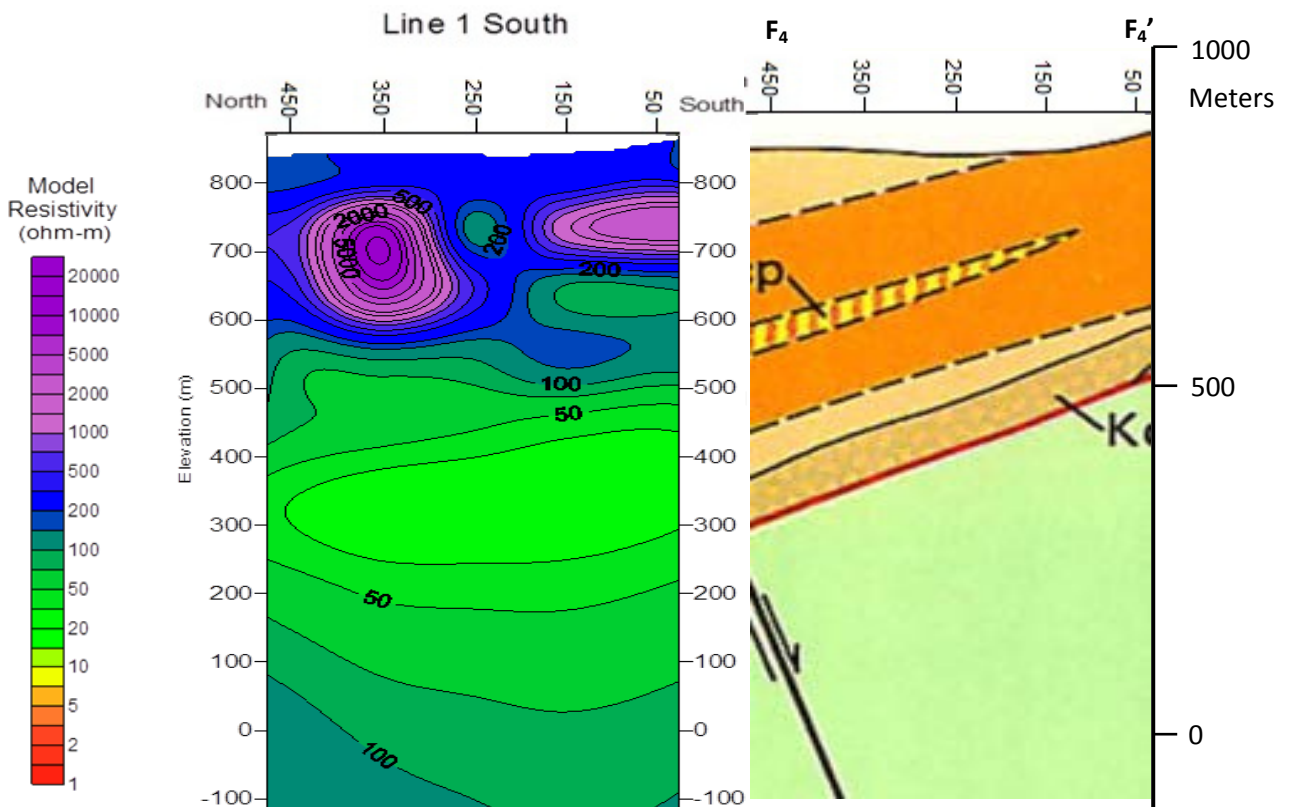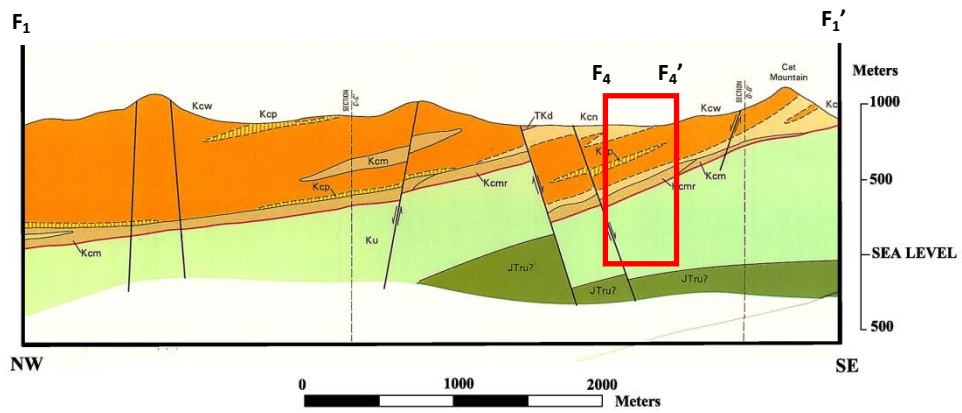
Figure 5.2: Red box (F$_4$-F$_4$') shows the location of Line 1 South on geologic cross section F$_1$-F$_1$'. Below shows a vertical comparison between resistivity cross section and geologic cross section on the same scale for Line 1 South.
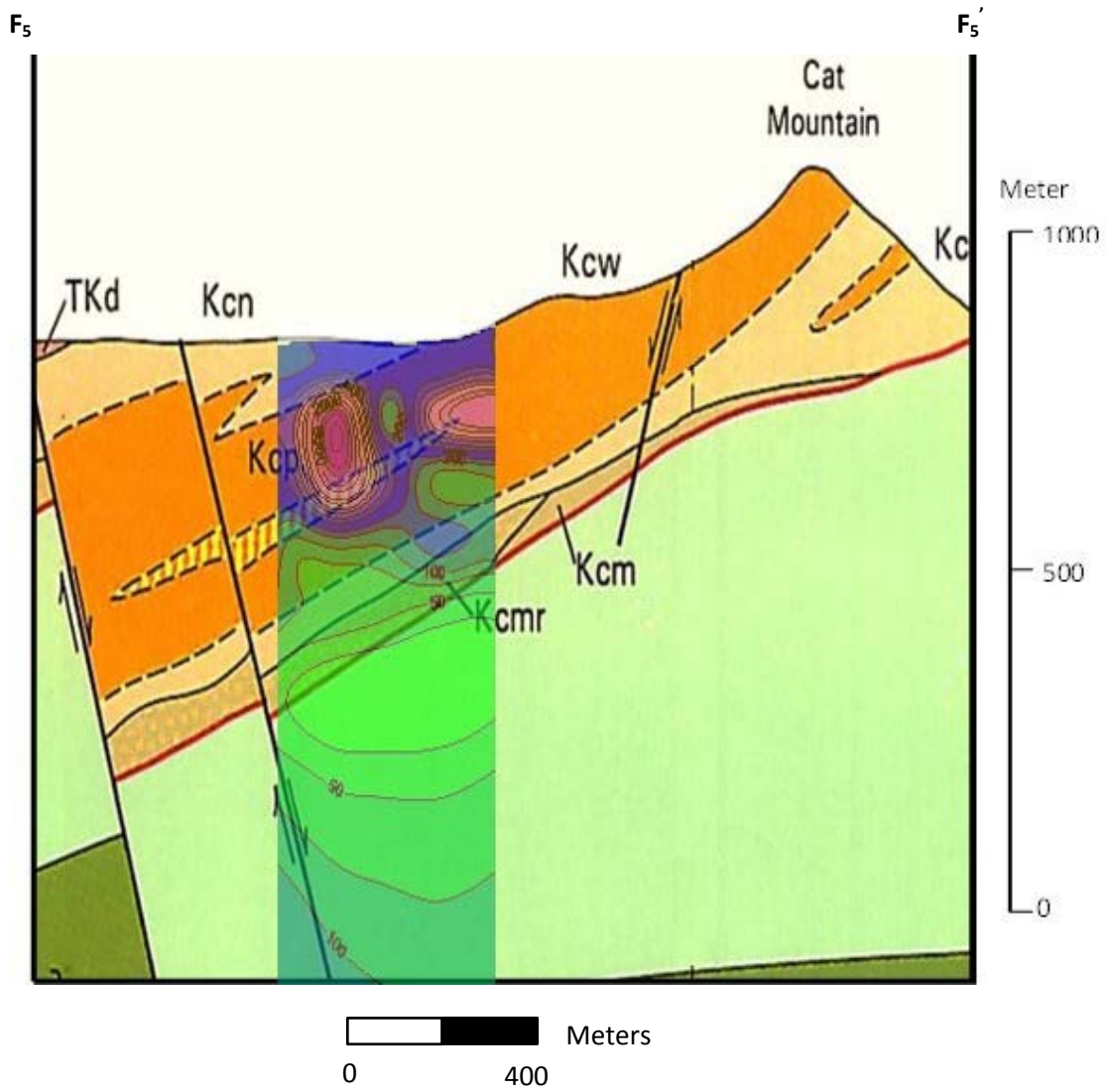
Figure 5.3: Overlain resistivity cross section of Line 1 South on geologic cross section F_5-F_5'.

5.3. Line 1 North

The depths to the conductive layer along Line 1 North range from about 200 to 500 meters (Figure 5.4). The resistivity cross section follows the shape of the postulated fault blocks as shown in the geologic cross section. Thus, the CSAMT data confirms the presence of the faults.

The prominent warm color representing low resistivity (<3 Ohm-m) at the northern end of the line is interpreted to be due to cultural interference. This resistivity value is too low for water-saturated sedimentary rocks units, which commonly have a minimum resistivity value in the order of 10 Ohm-m in this region. This very low resistivity region is interpreted to be due to the effect of the Tucson Water pipeline. The location of the pipeline is shown on Figures 5.5 to 5.7 as a yellow star. This steel pipeline is typically of the order of ten meters below the surface in this area and is three meters in diameter (Ricks, 2012).

Overall, the resistivity cross section of Line 1 North confirms the existence of the faults interpreted by Lipman in F_1-F_1' geologic cross section and the presence of low resistivity sedimentary rocks underneath the high resistivity volcanic rocks.
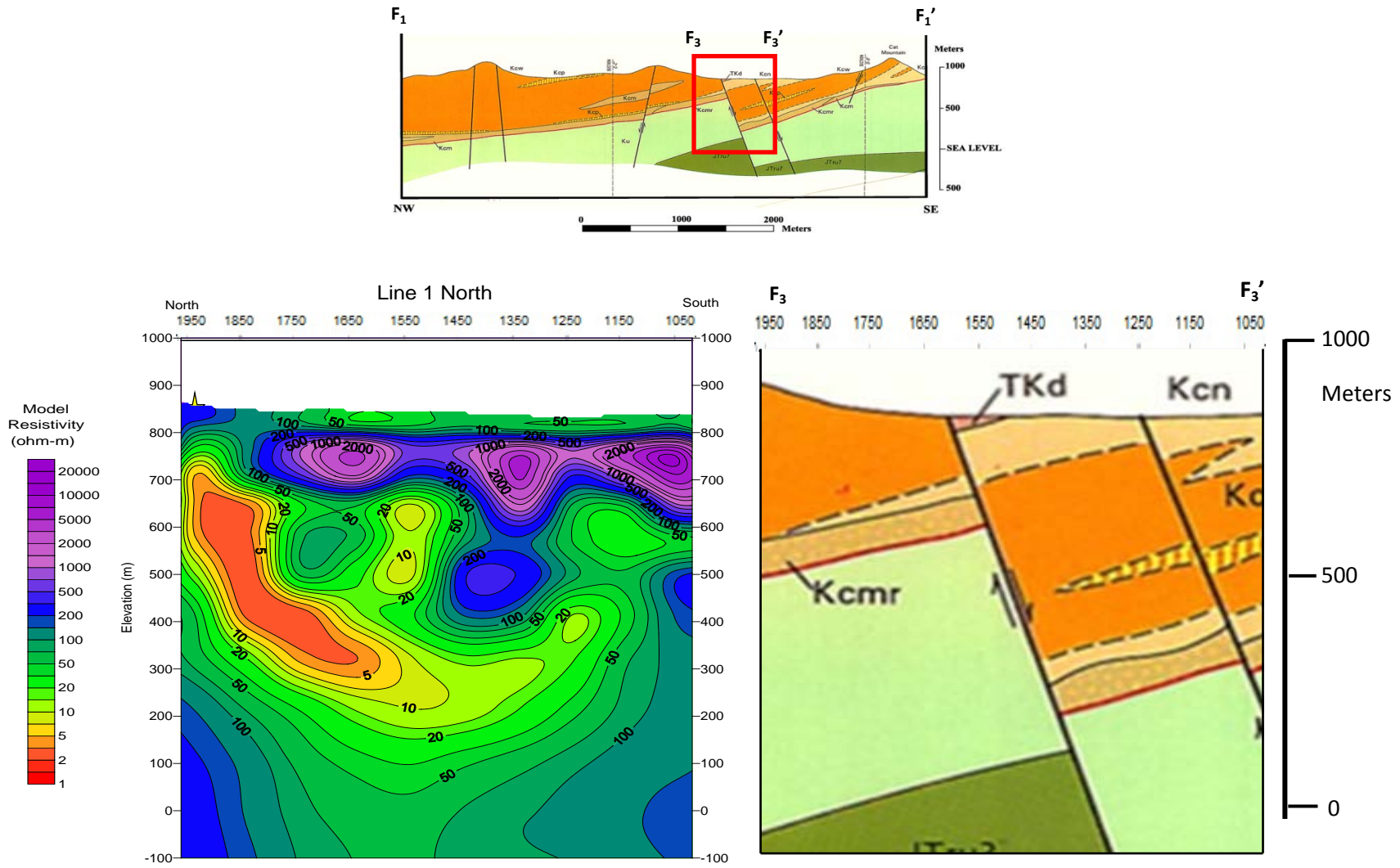
Figure 5.4 : Red box shows the location of Line 1 North (F₃-F₃') on geologic cross section. A star shows the location of the pipeline. Below shows vertical comparison between resisitivity cross section with geologic cross section on the same scale.
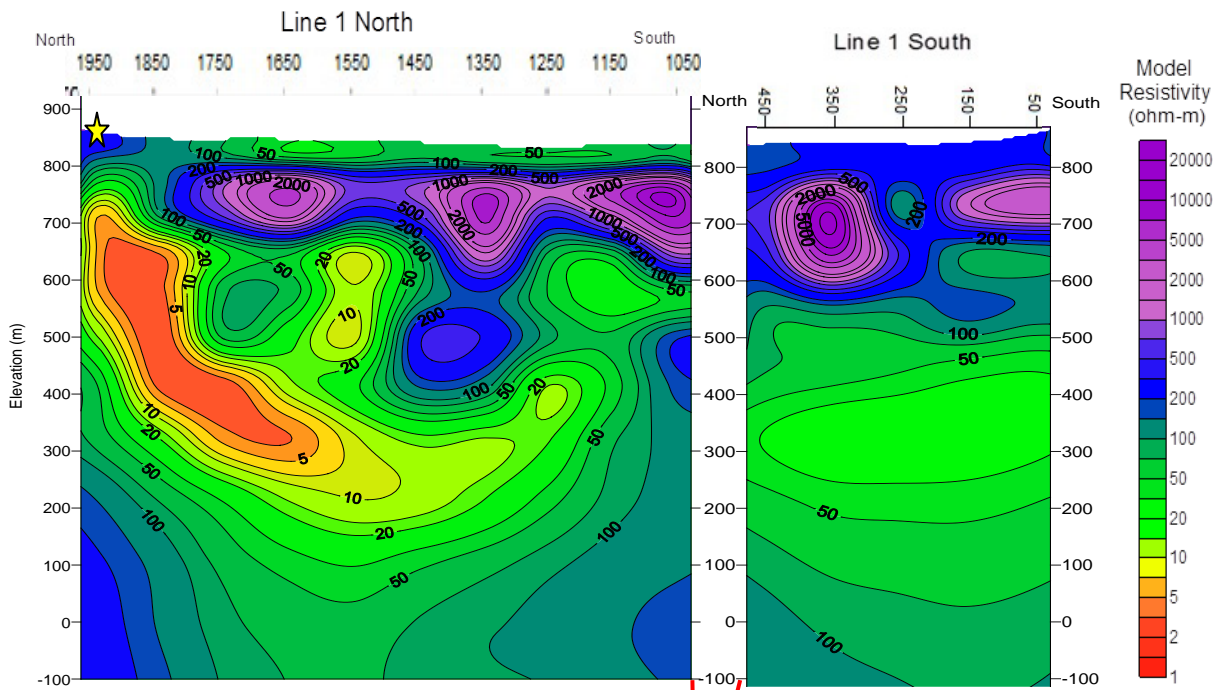
Figure 5.5 : (Top)Horizontal comparison between resistivity cross section and geologic cross section on the same scale for Line 1 South and North .The Red lines show the F₃'/F₄. (Right) Location of Line 1 North (F₃-F₃') and South (F₄-F₄') on geologic cross section.
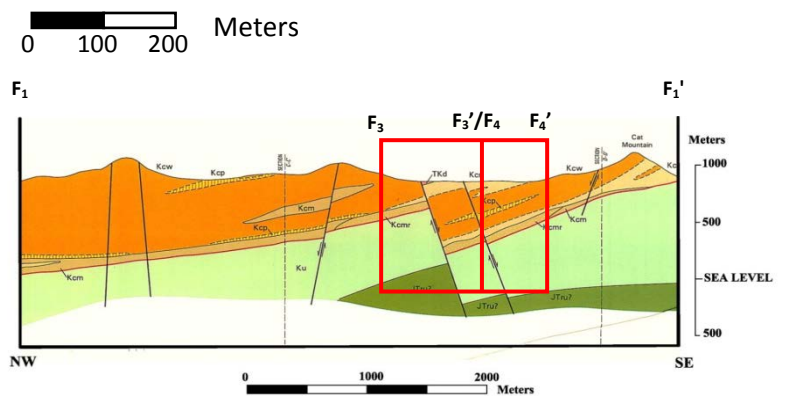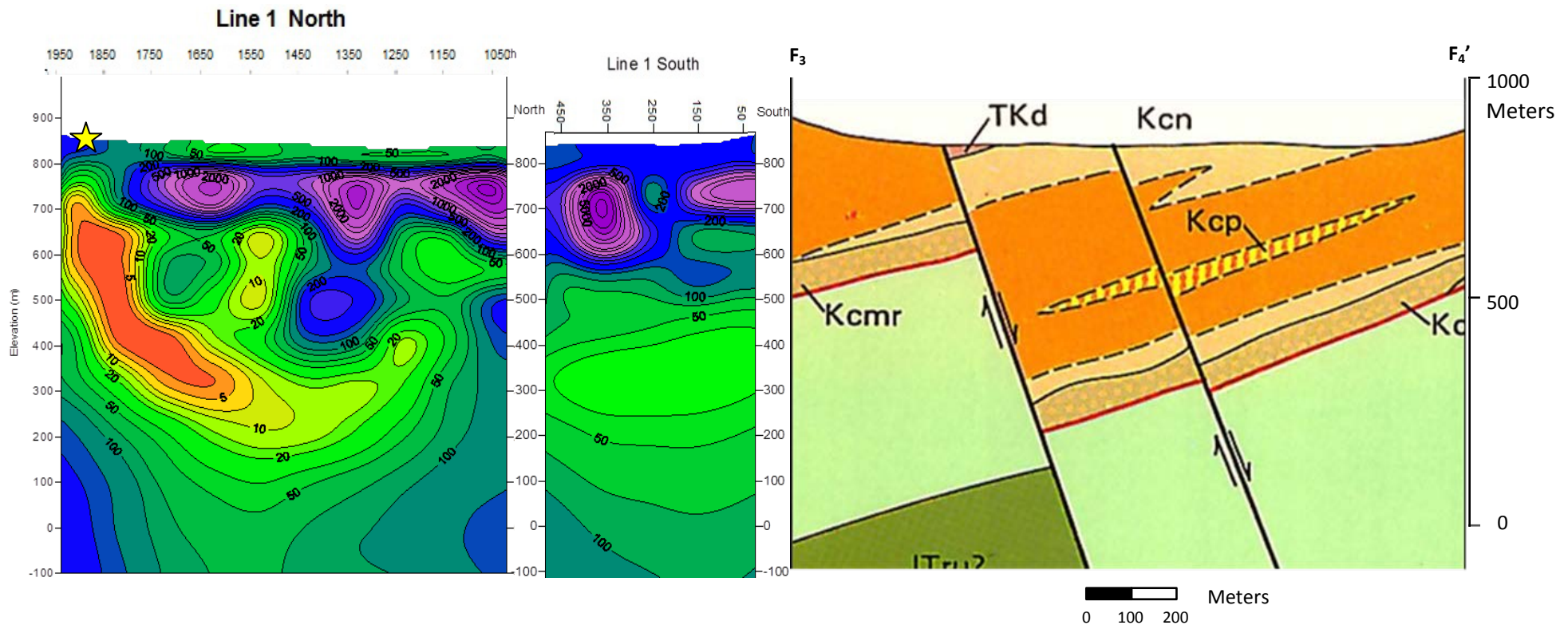
Figure 5.6: Vertical comparison between resistivity cross section and geologic cross section (F_3-F_4') for combined Line 1 South and North.
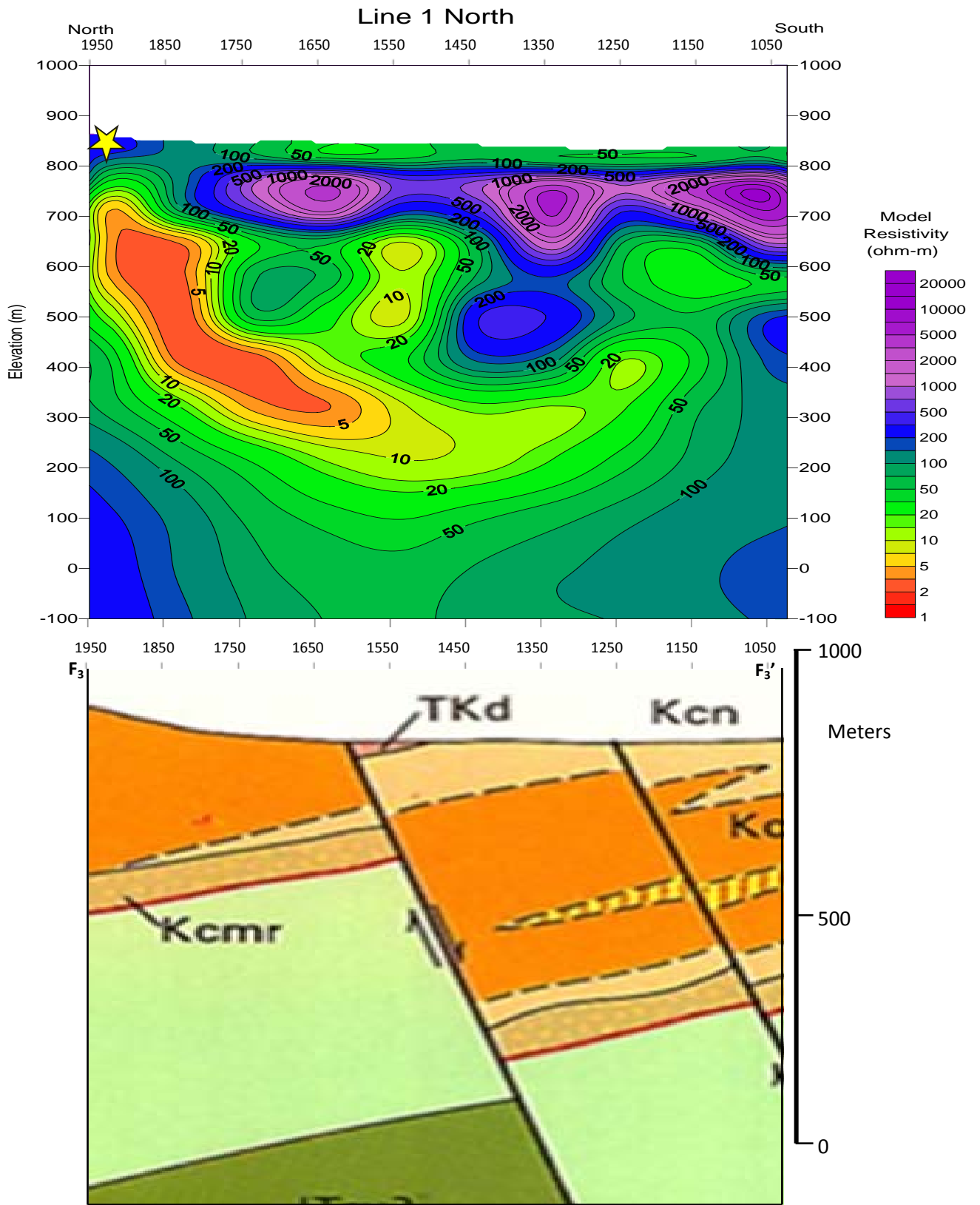
Figure 5.7 : Lateral comparison between resisitivity cross section and the geologic cross section for Line 1 North on the same scale.
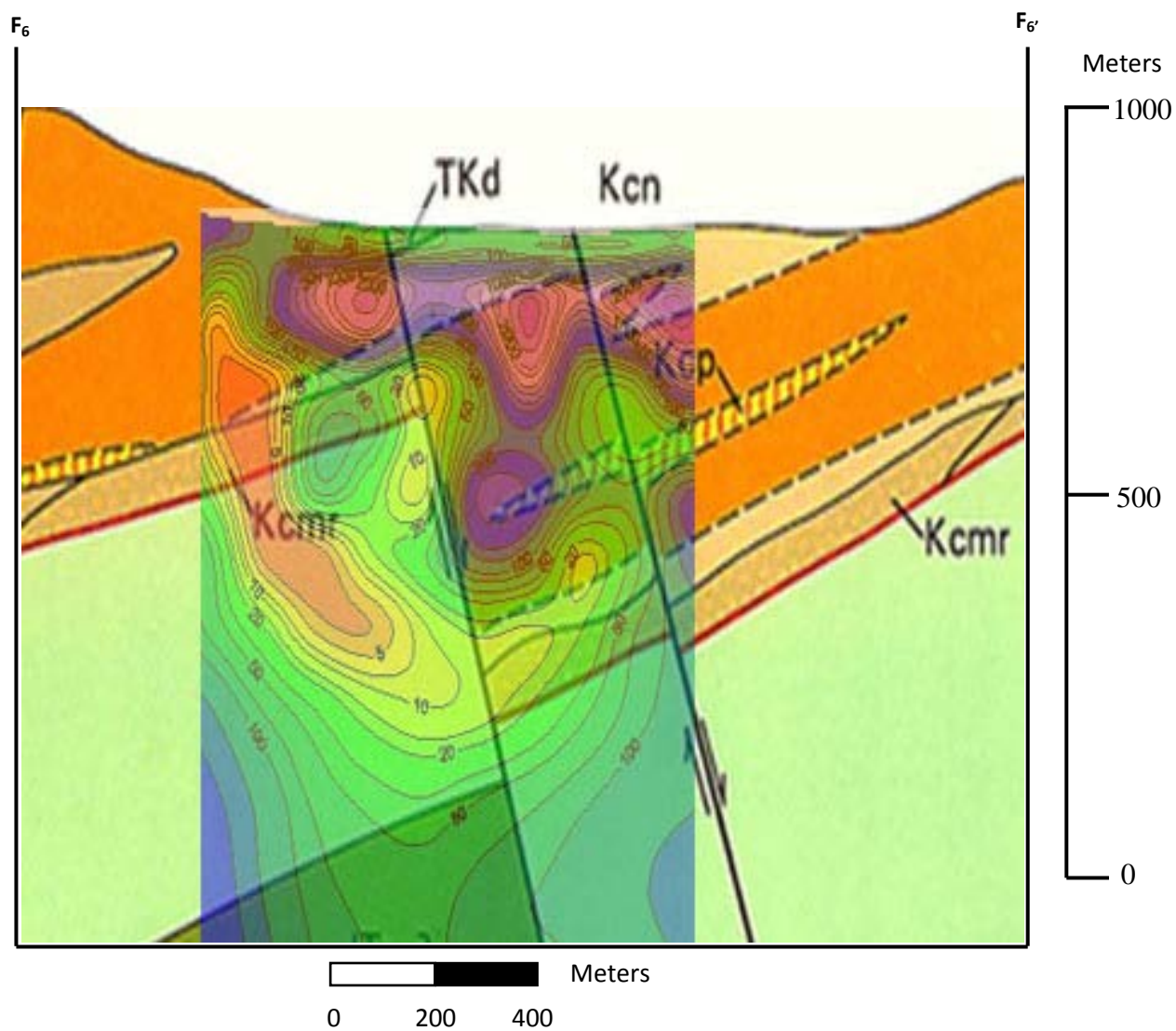
Figure 5.8: Resistivity cross section of Line 1 North overlain on the geologic cross section F_6-F_6'.

5.4. Line 2

The elevation of the conductive layer in Line 2 ranges from 250 m to 350 m above sea level (Figure 5.9).The boundary depth is deeper compared to the cross section of Line 1 North and South. This cross section suggests a shallower dip in the north-south direction in comparison to the cross section of Line 1. The deeper boundary of the conductive layer in Line 2 indicates a tilting from Line 1 to Line 2. It could also mean that the volume of permeable sedimentary rocks decreases eastward. Figure 5.10 generally shows that the pattern of the resistivity cross section for the first three stations maps the geologic units in geologic cross section. The low resistivity of interfingering pattern at elevation 500m to 600m is suspected to correlate with Kcp unit, which is also observed in the southern end of Line 1 North.

Figure 5.11 shows a possible fault line inferred from the geologic map and the lateral variability of resistivity. Because this is the same fault that crosses near station 1600 in Line 1 North, the dip is assumed to be the same. The same pattern of resistivity variation at the north end of Line 1 North is apparent in Line 2. The depth extent of the very high conductivity anomaly is also the same as in Line 1 North. This suggests that the sources of the anomaly observed in both cross sections are the same, namely the steel pipeline, with some effect from a nearby fence also. The warm color present is lower than about 3 Ohm-m seen as in Line 1. This might be due to the closer proximity of Line 2 to the barbed wire fence.
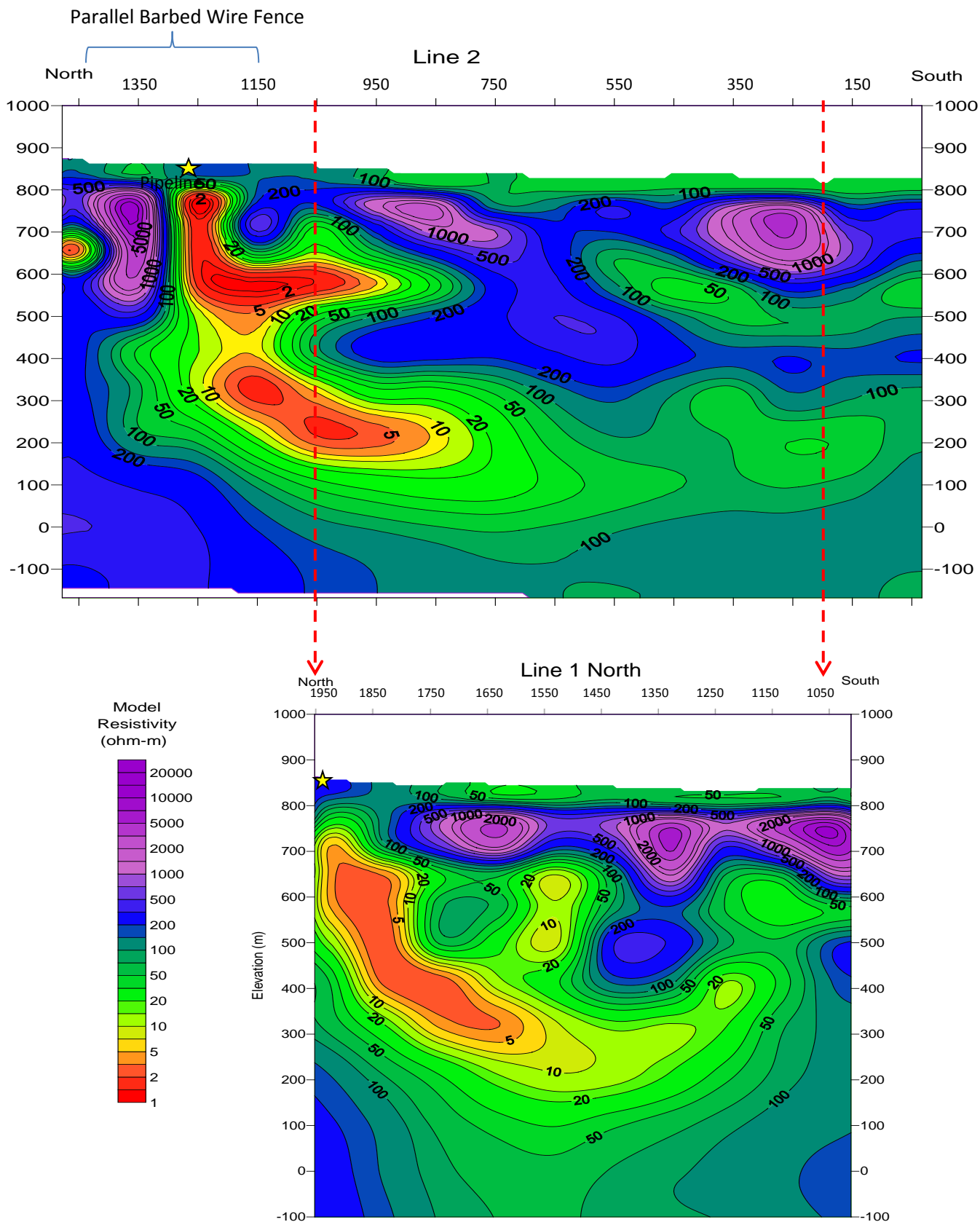
Figure 5.9: Dashed arrows from Line 2 correspond to the same cross section area of Line 1 North.
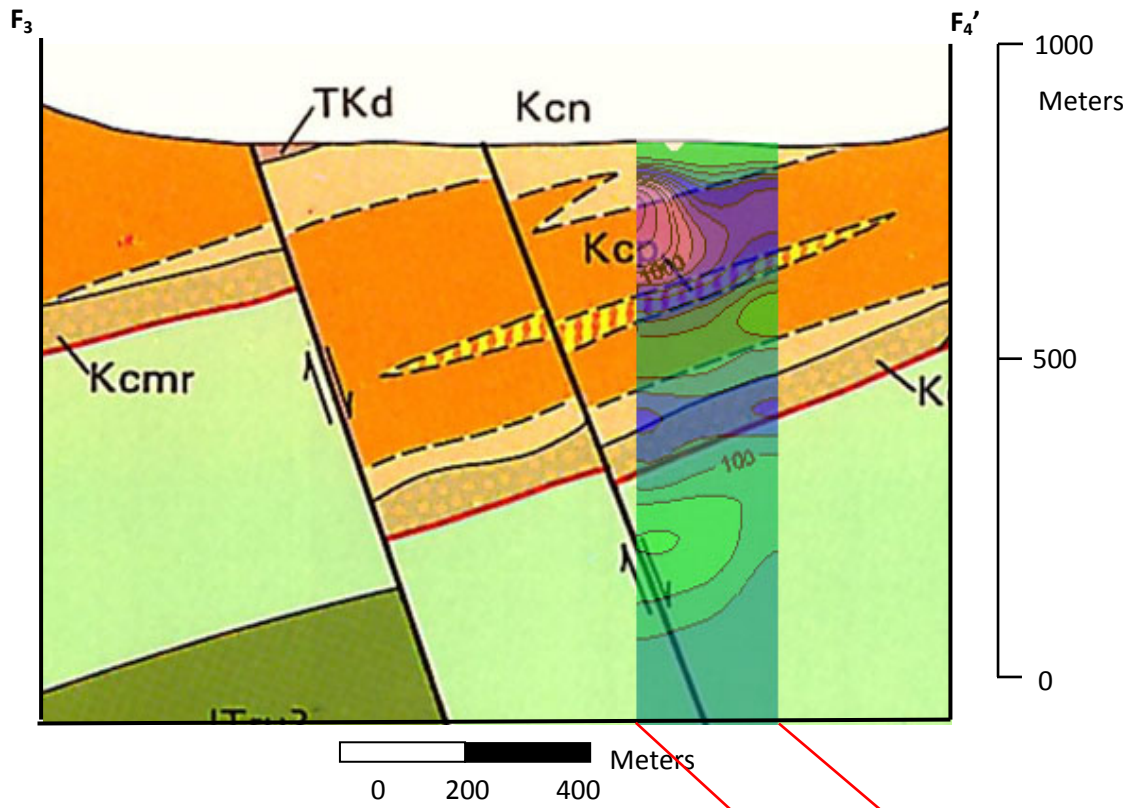
Figure 5.10: Overlain resistivity cross section for the first 3 stations of Line 2 on geologic cross section F_3-F_4'.
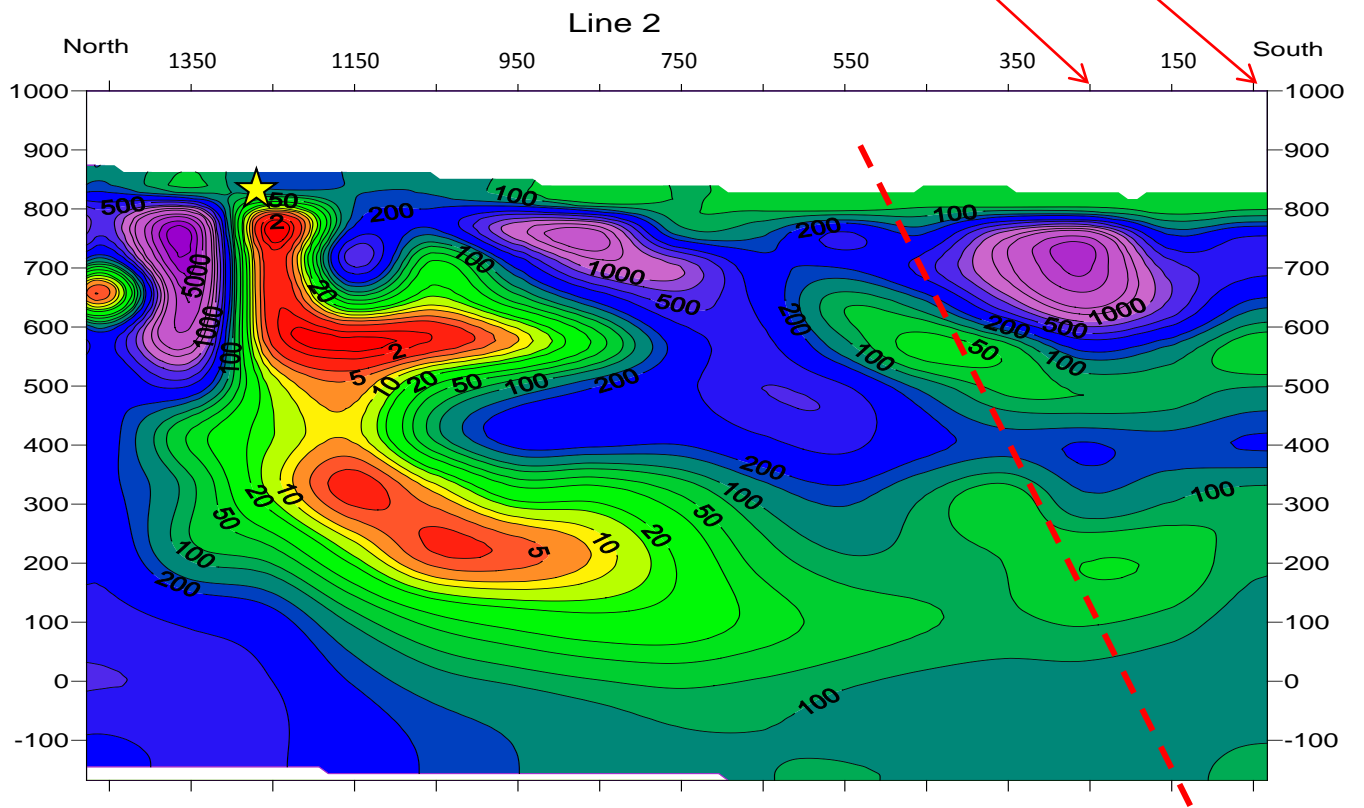
Figure 5.11: Dashed line shows an inferred fault line based on geologic map and the contour lines.

In summary, the resistivity cross sections produced using CSAMT technique generally agree with the geologic cross section interpreted by Lipman. The expected smooth continuation of the resistivity profile from Line 1 South to Line 1 North is slightly offset, possibly due to the different transmitter used in 2010 to record the Line 1 South profile. The comparison between the geologic cross section F_1-F_1' with Line 1 South and North is also limited since they do not perfectly intersect. The CSAMT survey confirms that there are permeable sedimentary rocks trapped underneath the impermeable volcanic rocks. The depth to the conductive layer varies within Line 1 and Line 2 and between these lines. The cultural interference at the northern part of both lines prevents the estimation of the conductive depth layer in that area.

6. Summary and Conclusions

6.1. Data Profile Summaries.

In this report, CSAMT data are compared to the magnetic data, gravity data and TEM data obtained from last year's class report, Geophysical Investigation of the Tucson Mountains, Geophysics Field Camp 2011. Surfer version 8.0 was used to produce the depth to the conductive-layer figures and the elevation of the conductive-layer figures.

Magnetic Stations
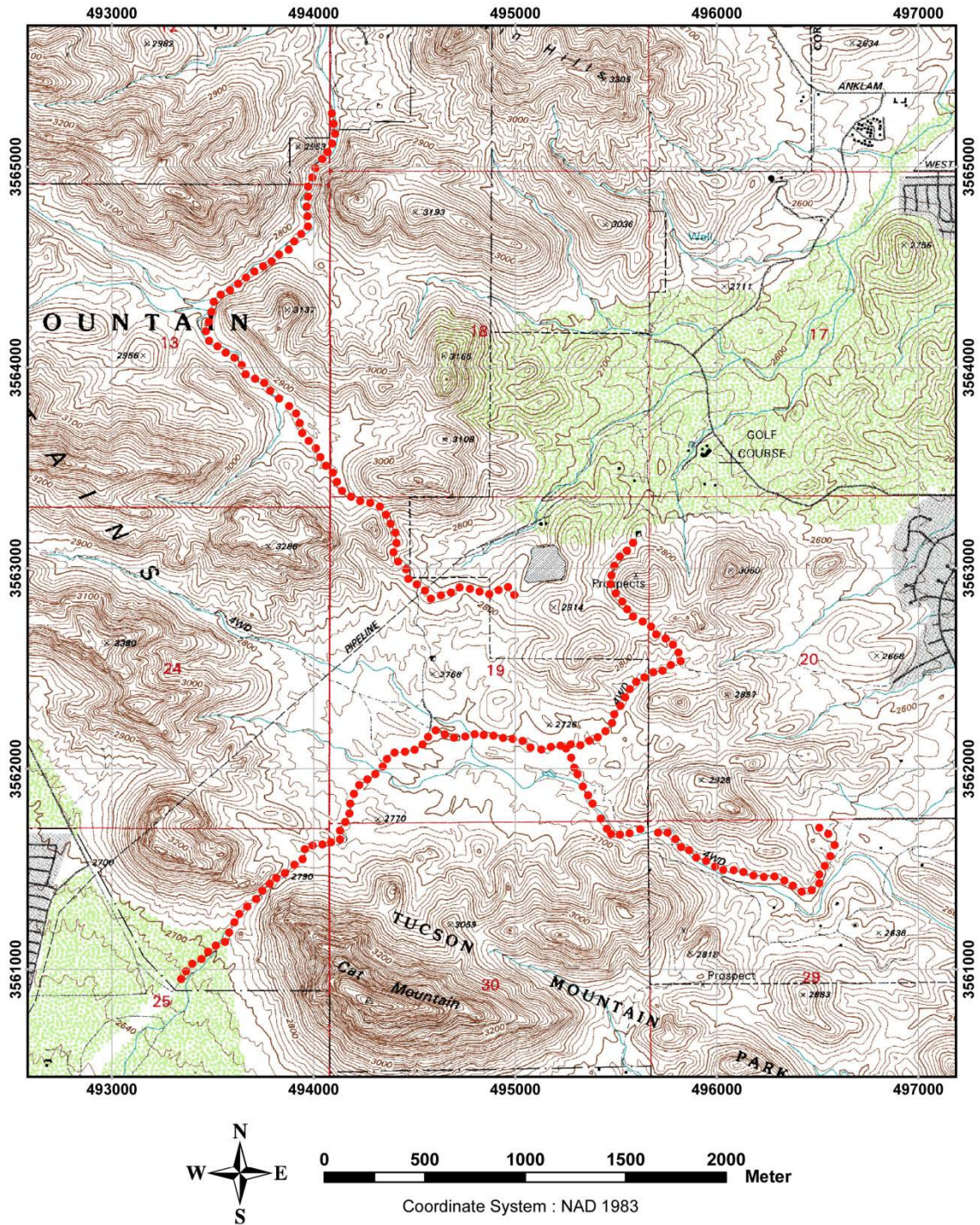
Figure 6.1: Topographic contour map of study area with all magnetic data points marked as red dots.

Survey Map
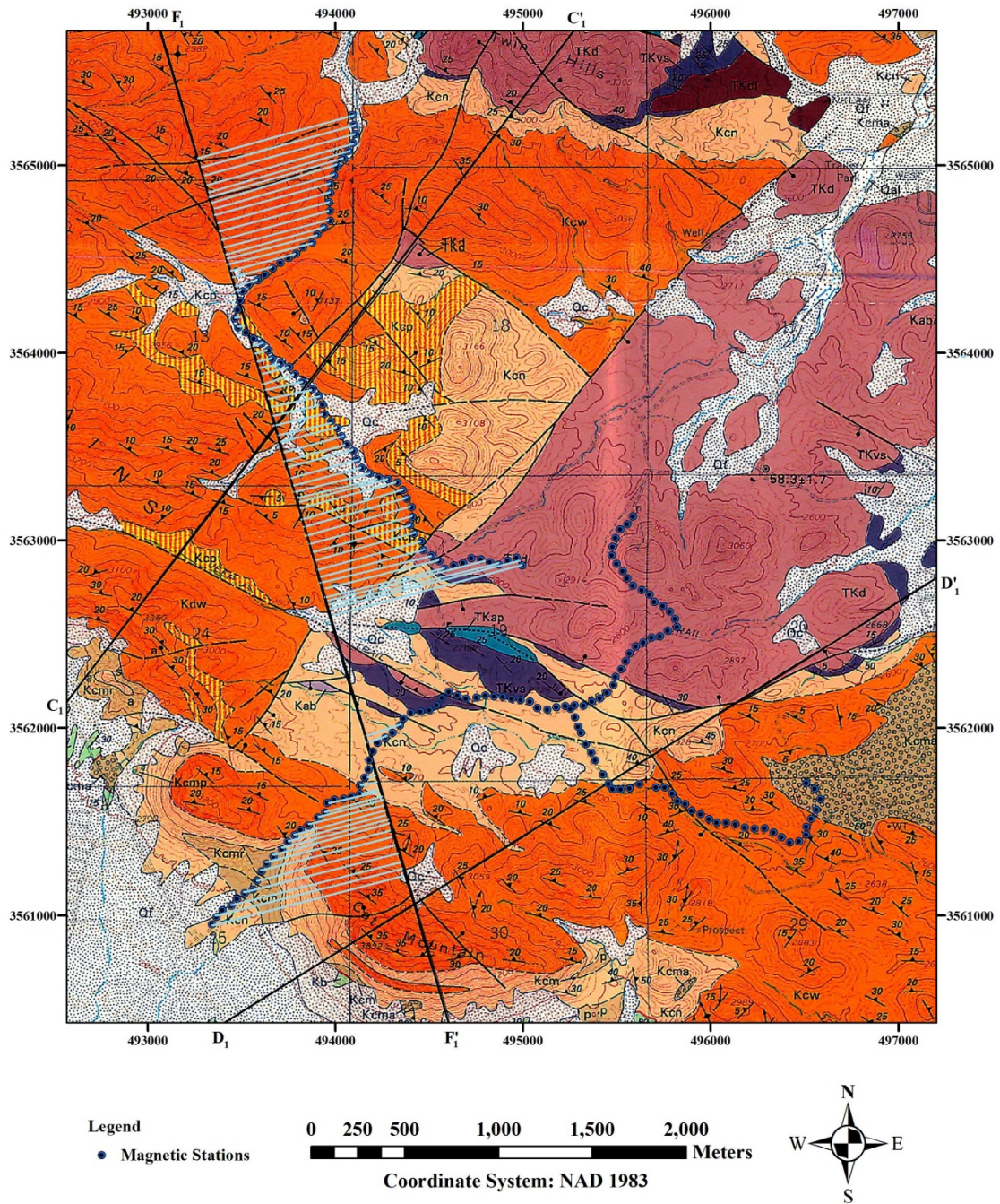
Figure 6.2: A map showing which magnetic points were projected onto the F_1-F_1' cross section line.
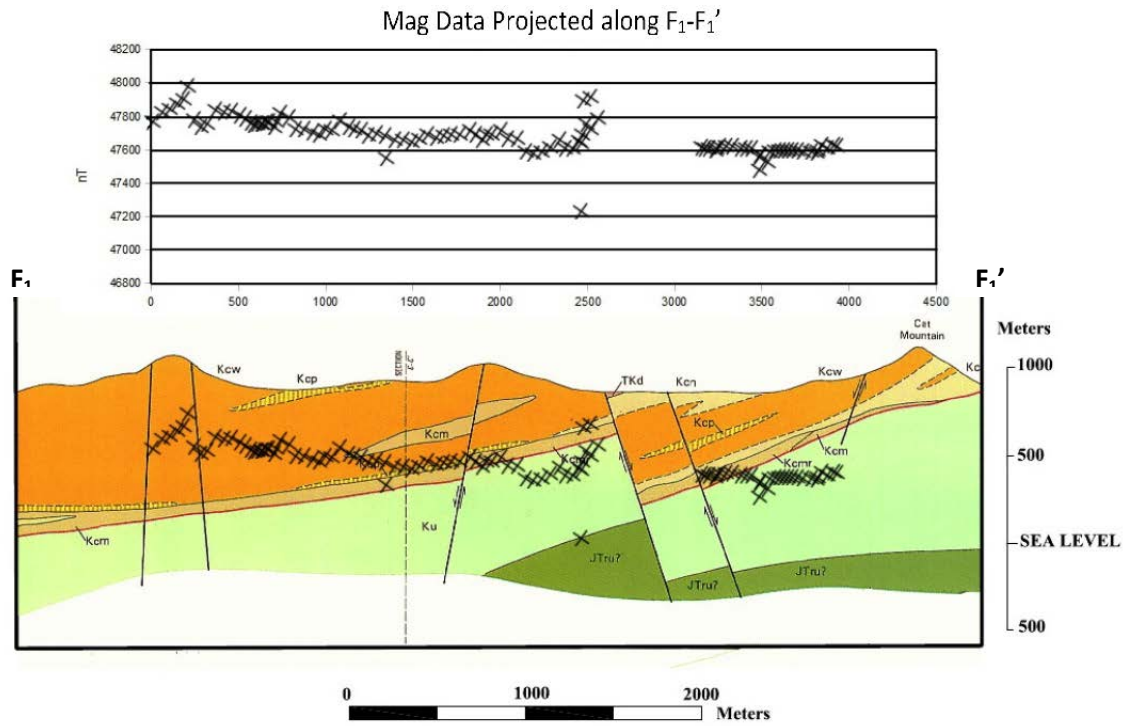
Figure 6.3: A graph of the corrected magnetic measurements at locations projected onto the F₁-F₁' line.

Survey Map
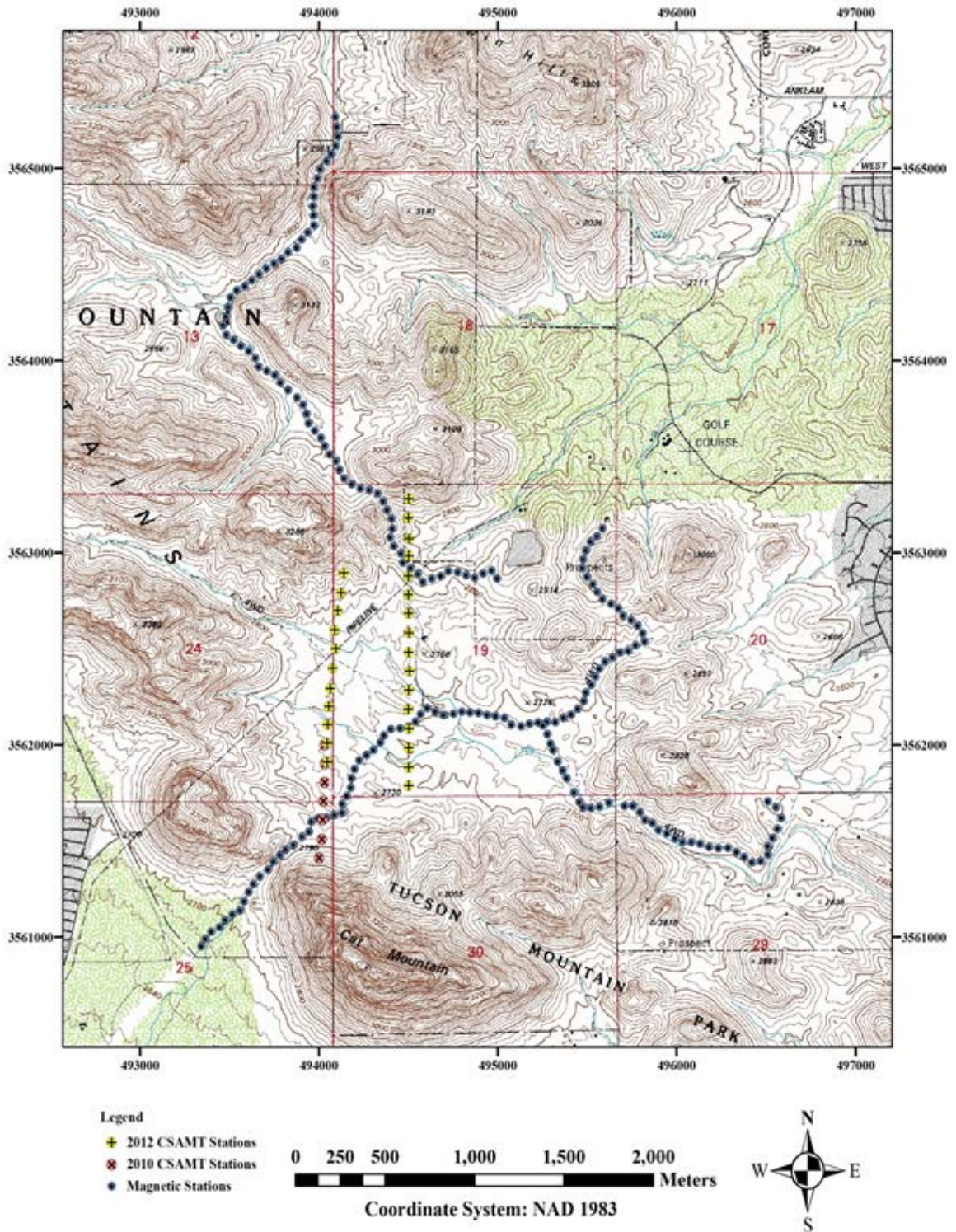
Figure 6.4: CSAMT and Magnetic Stations on topographic map.

Survey Map
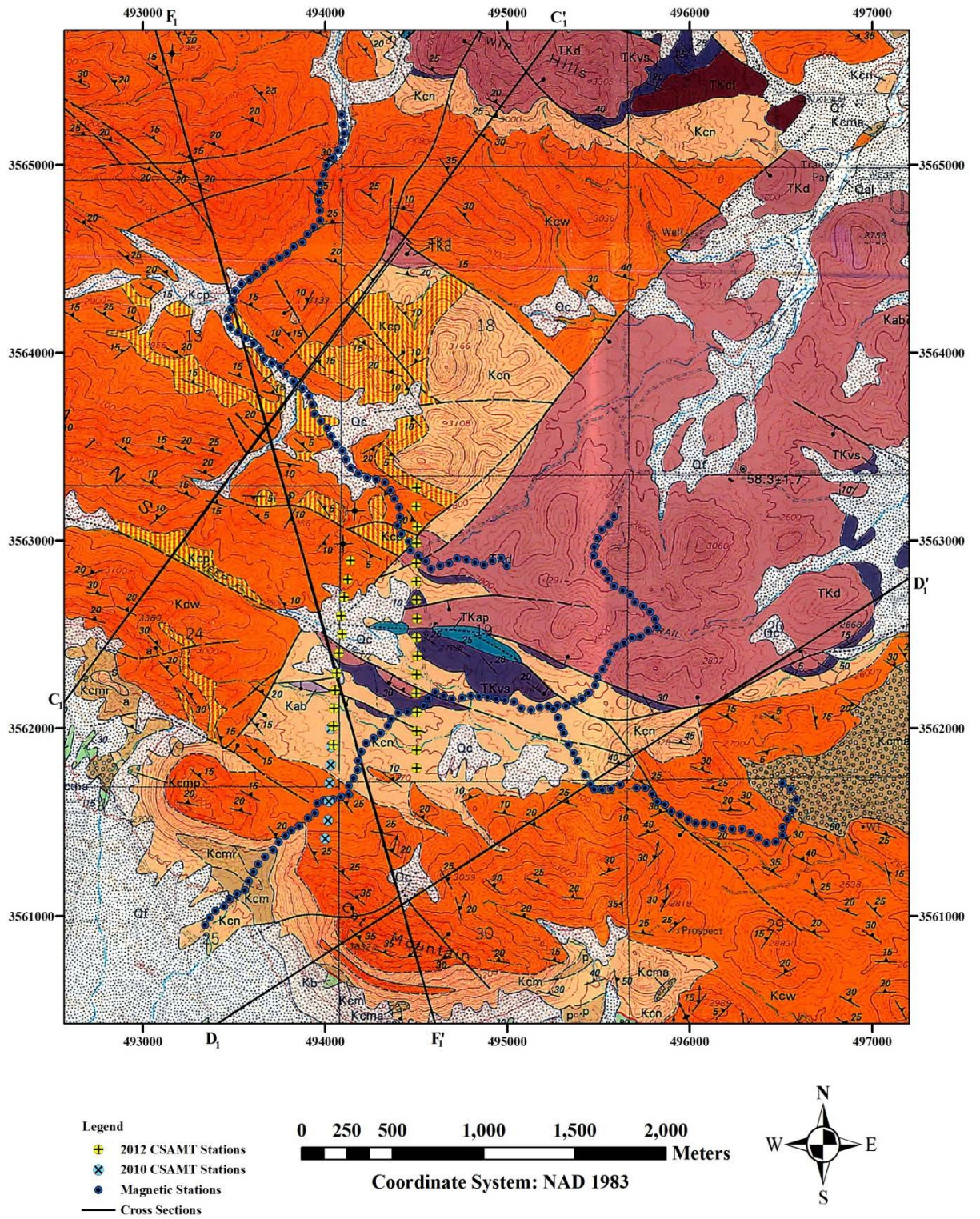
Figure 6.5: CSAMT and Magnetic Stations on geologic map.
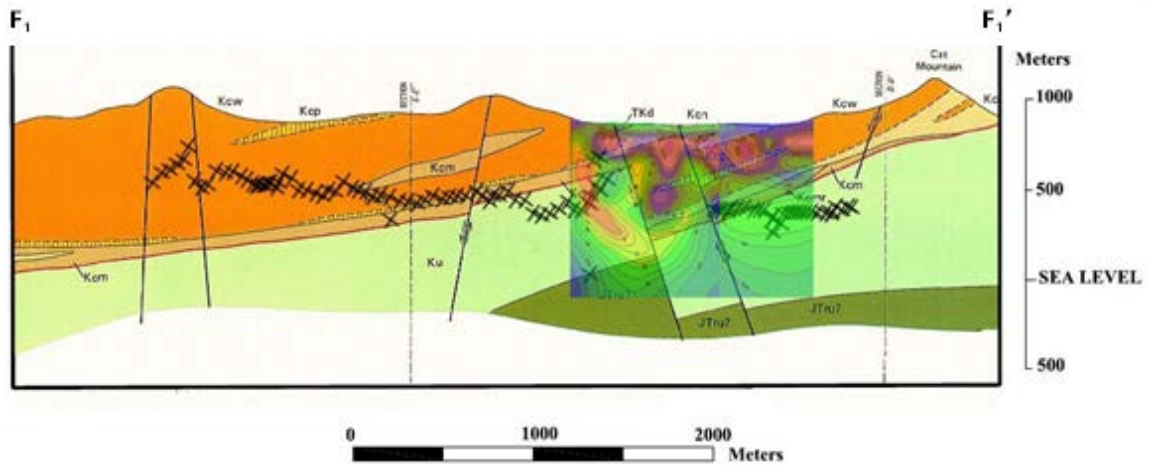
Figure 6.6: F_1-F_1' Magnetics and CSAMT Summary. Magnetics (black crosses): The central fault correlates with the magnetic field data. The fault feature can be determined by the anomaly correlation between the magnetic field and the geological structures. The CSAMT data also correlate with the Magnetic data.

Figure 6.7: General overview of the Tucson Mountains with gravity stations and field base station.

Survey Map
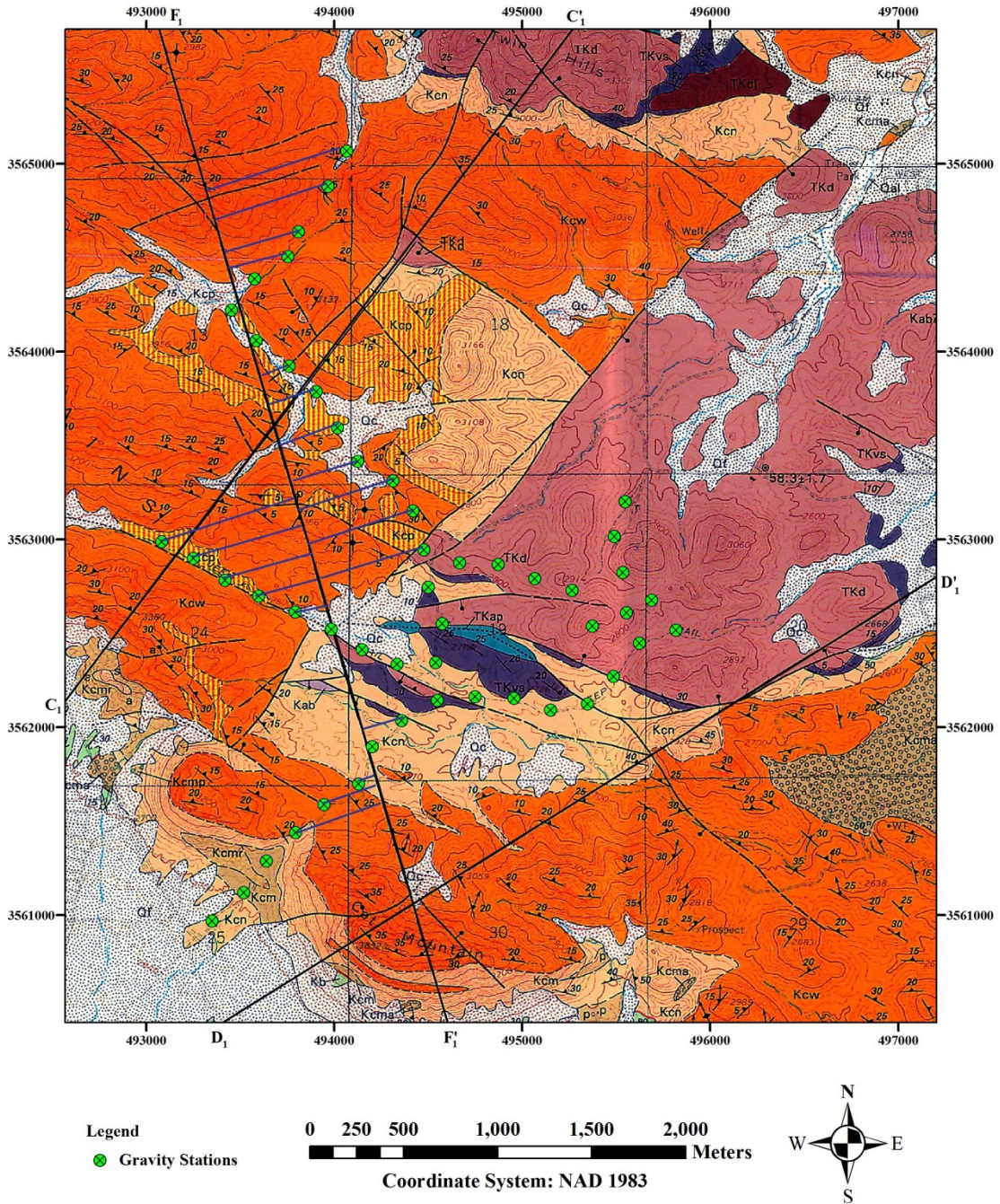
Figure 6.8: The survey area with all measured gravity stations are shown by blue points. Location of geological cross sections (thick black lines) and points projected onto F_1-F_1' by the blue lines showing which point was projected and where it was projected. Modified from (Lipmann, 1993).
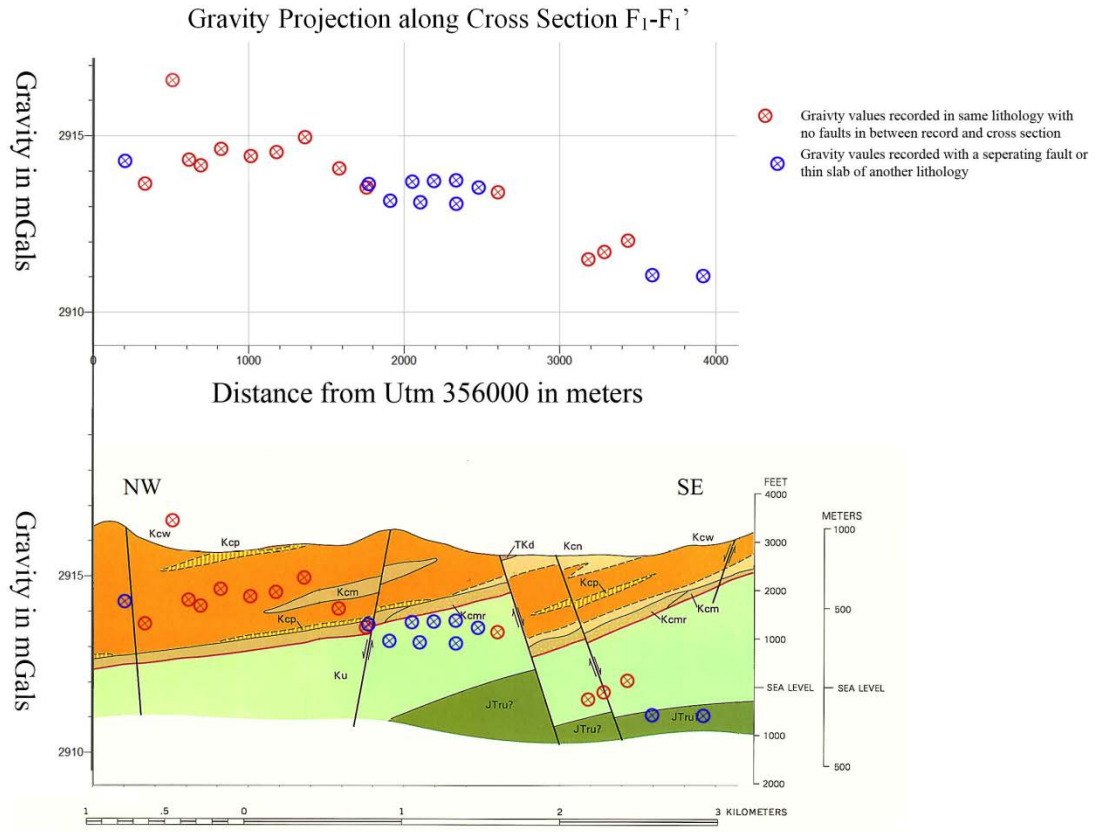
Figure 6.9: Gravity projection for F_1-F_1'.The graph on top shows gravity values in mGals on the y axis and distance in meters on the x-axis. The cross section below has had the points from the gravity survey superimposed so the correlations can be more easily seen. Modified from (Lipman, 1993).

Survey Map
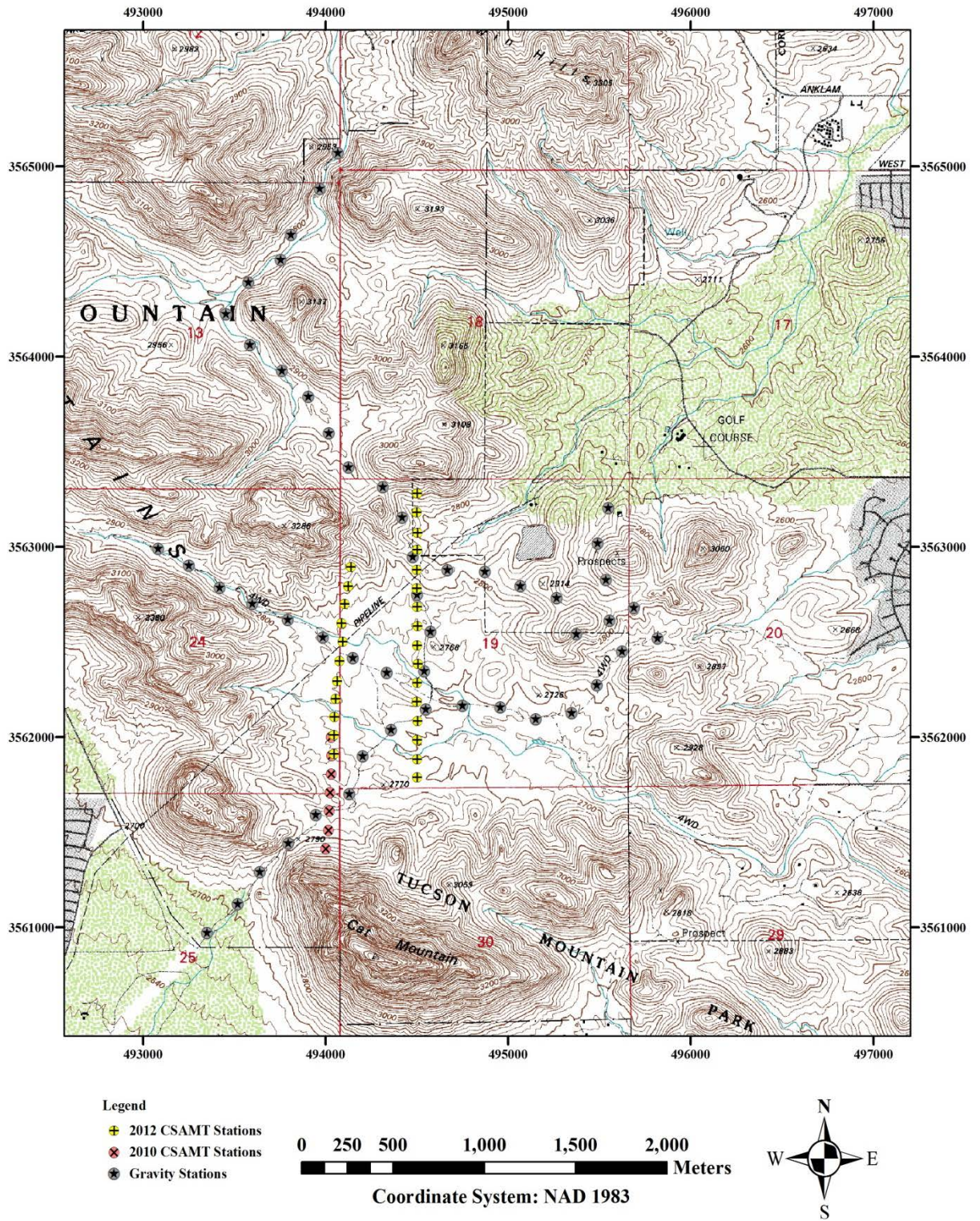
Figure 6.10: Gravity and CSAMT Stations on topographic map.
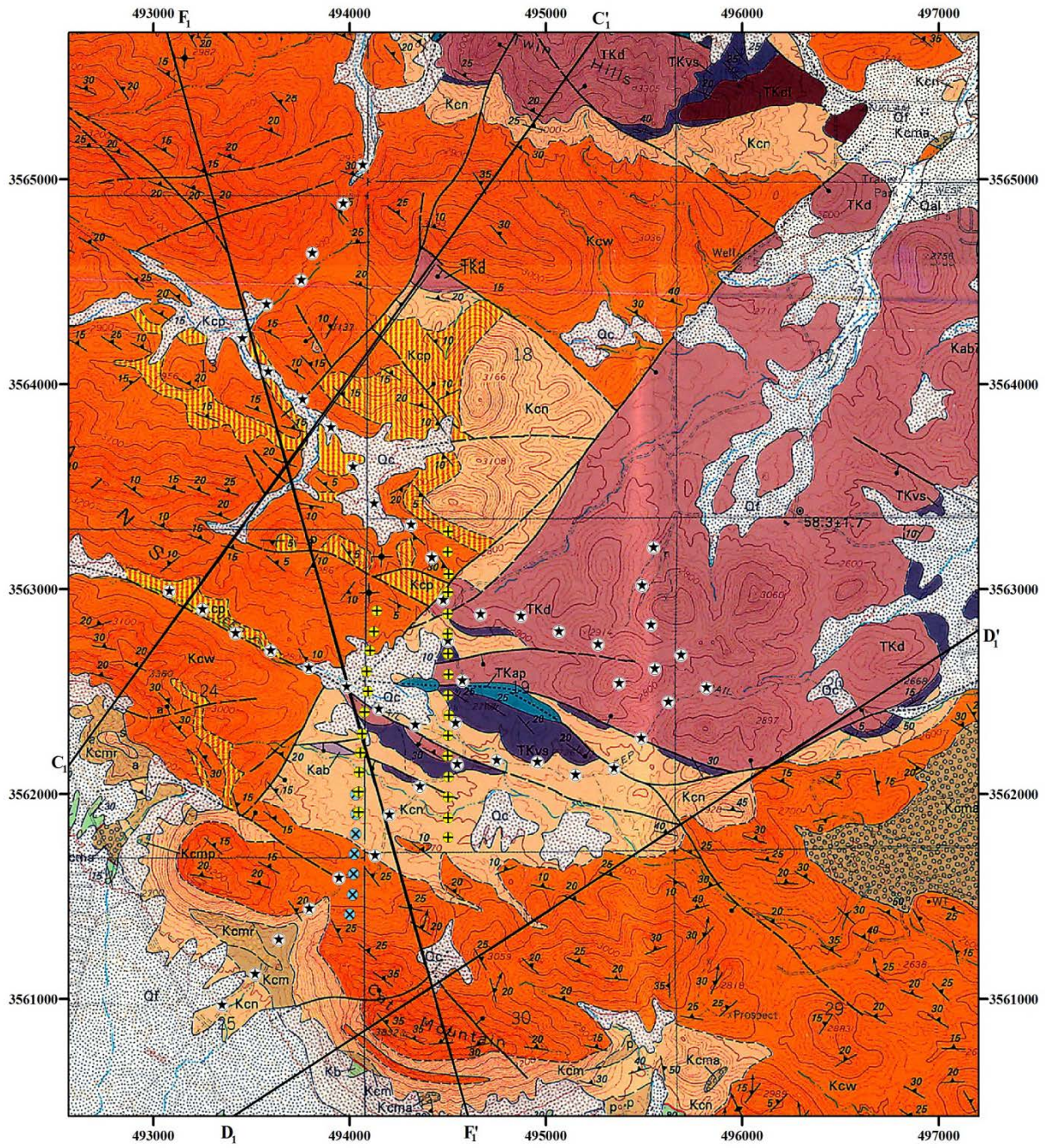
Survey Map
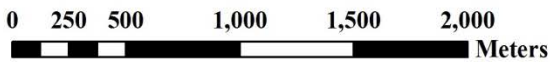
Figure 6.11: Gravity and CSAMT Stations on geologic map.

59
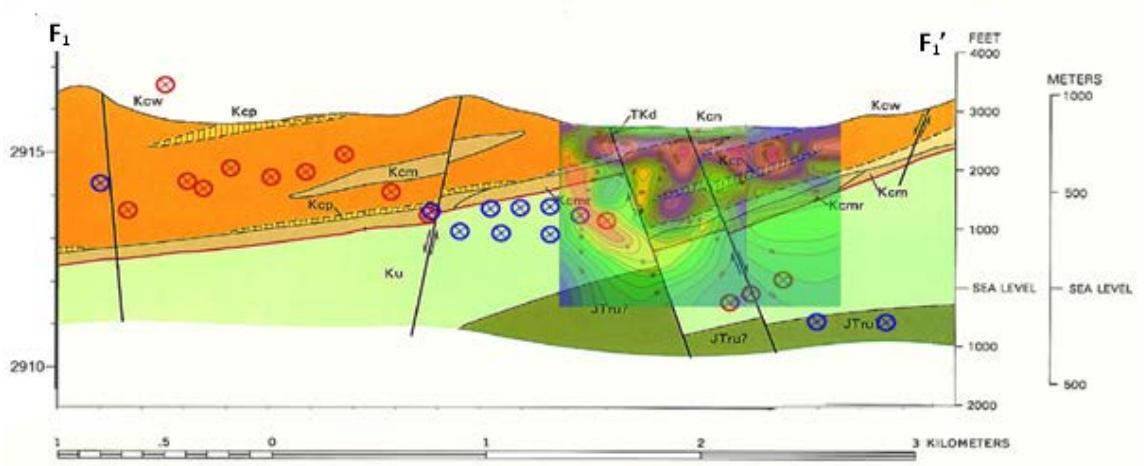
Figure 6.12: Gravity and CSAMT Summary. The gravity data are shown by the blue and red circles. The CSAMT section is also overlain. There is a correlation between both methods and the hypothesized faults.

TEM Stations
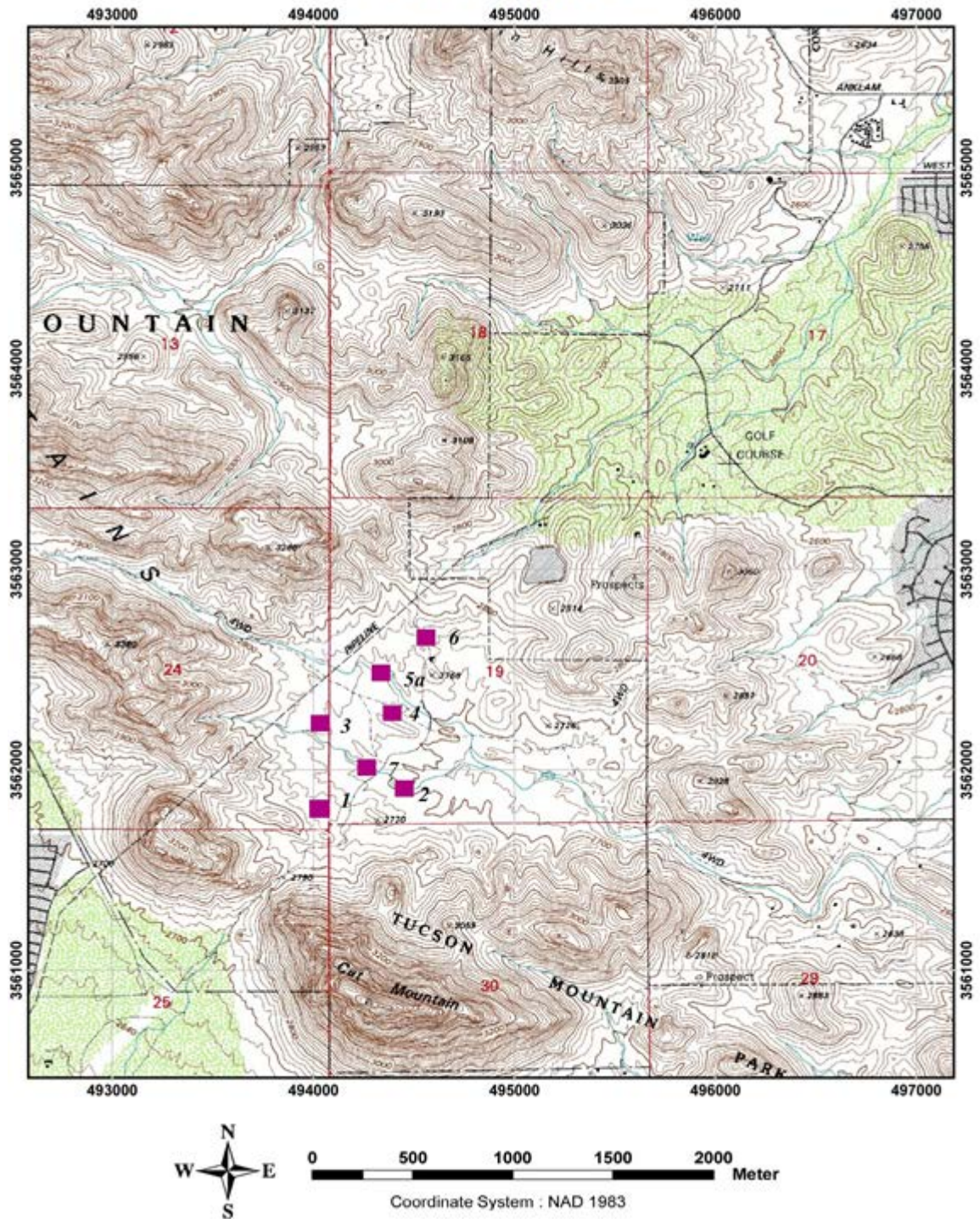
Figure 6.13: Location map of the TEM sites.
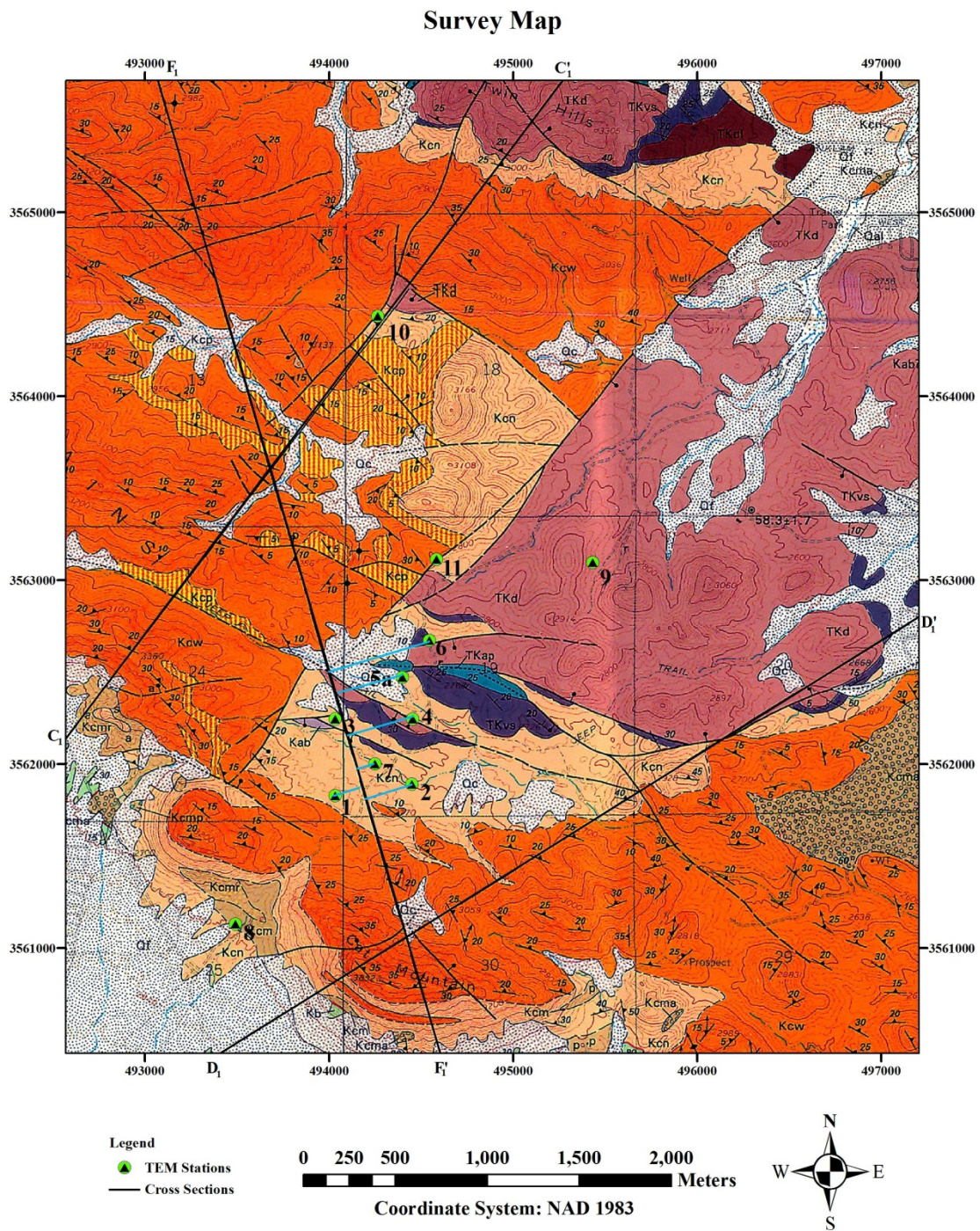
Figure 6.14: Map showing the locations and the projections of the TEM station loop centers on the different geological cross sections.
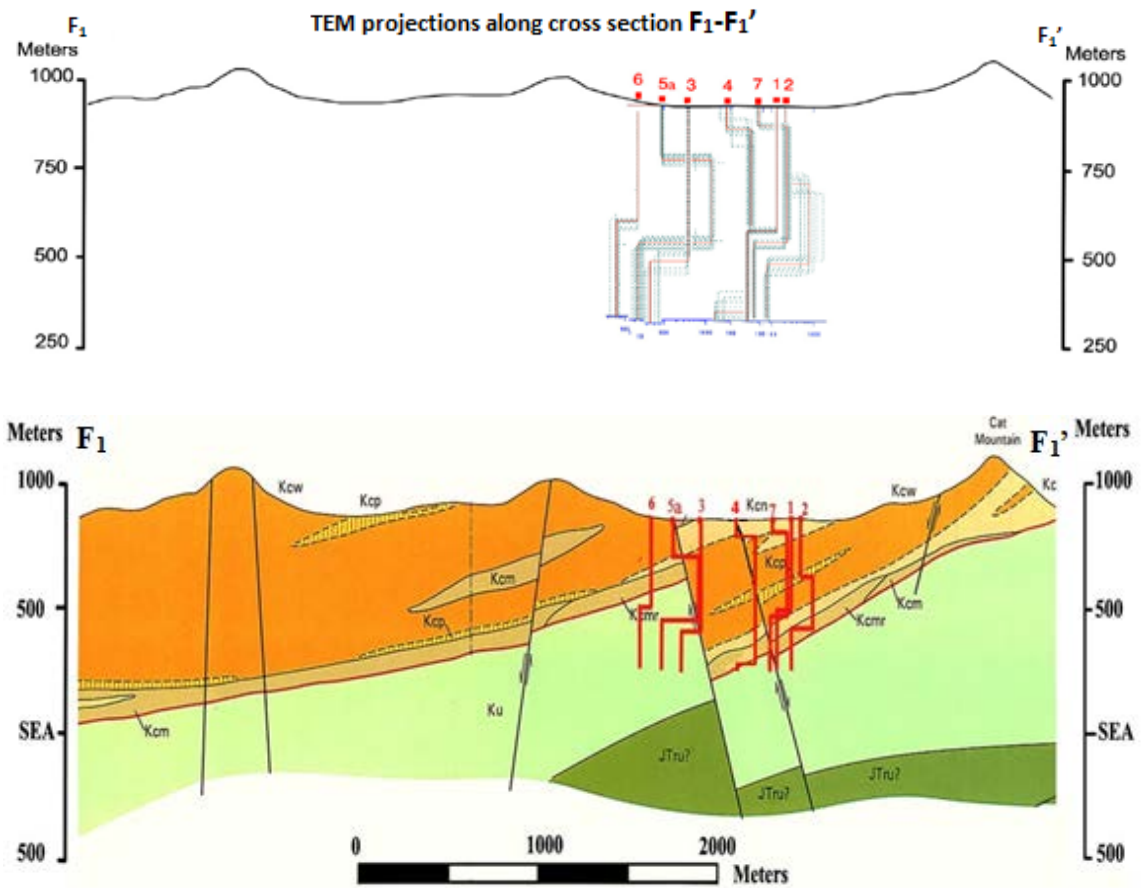
Figure 6.15: Comparison of TEM inversion model with F_1-F_1' interpreted geological cross section.

Survey Map
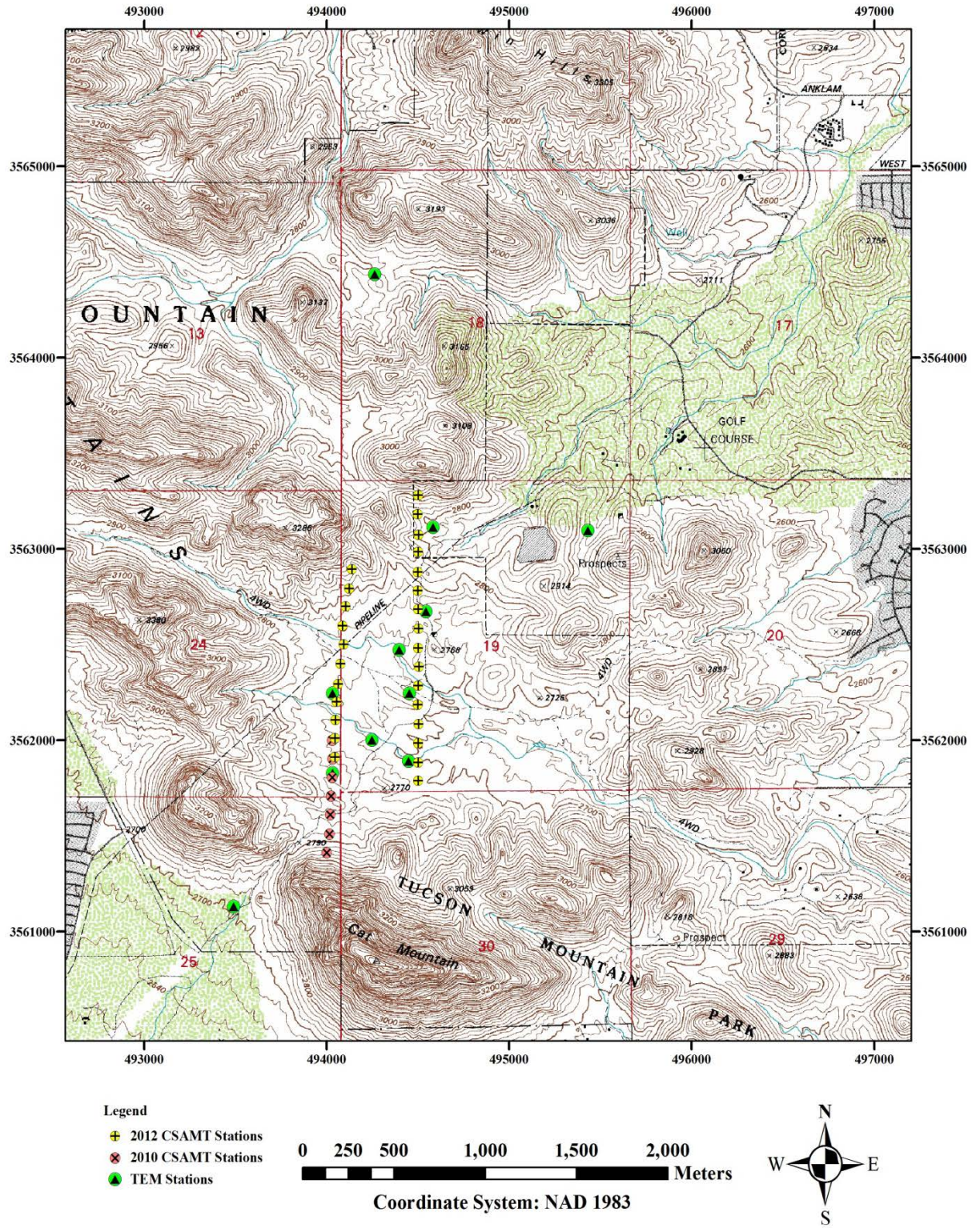
Figure 6.16: TEM and CSAMT Stations of topographic map.

Survey Map
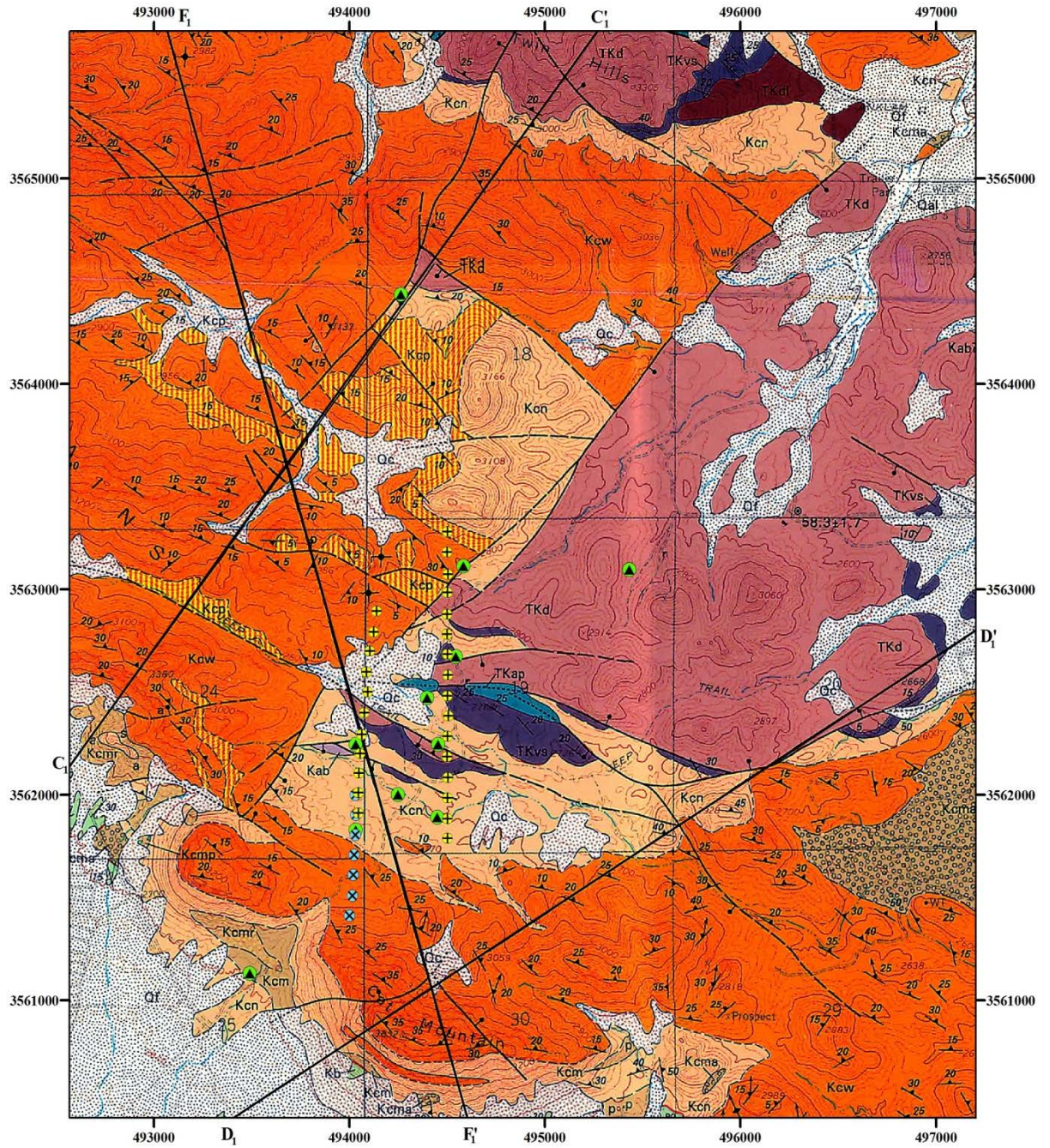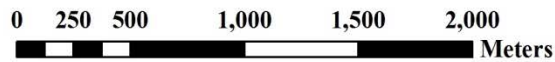
Figure 6.17: TEM and CSAMT on geologic map.
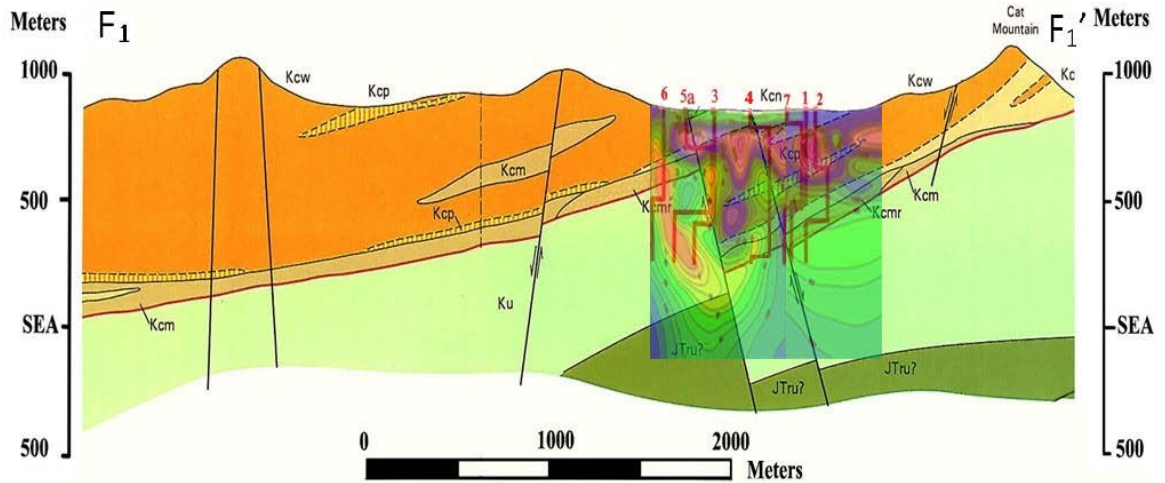
Figure 6.18: F_1-F_1' TEM and CSAMT Summary. TEM soundings (red lines): The TEM soundings on this profile line distinguish between the high-resistivity volcanics (Kcw) that overlay the low-resistivity sedimentary rocks (Ku). Overall, the TEM data correlate well with the geological cross section. CSAMT (contour overlay): The CSAMT data between 1000m and 500m are affected by the pipeline. The CSAMT data between 500m and -100m correlate well with the interpreted geological cross section, including the depth to the sedimentary layers
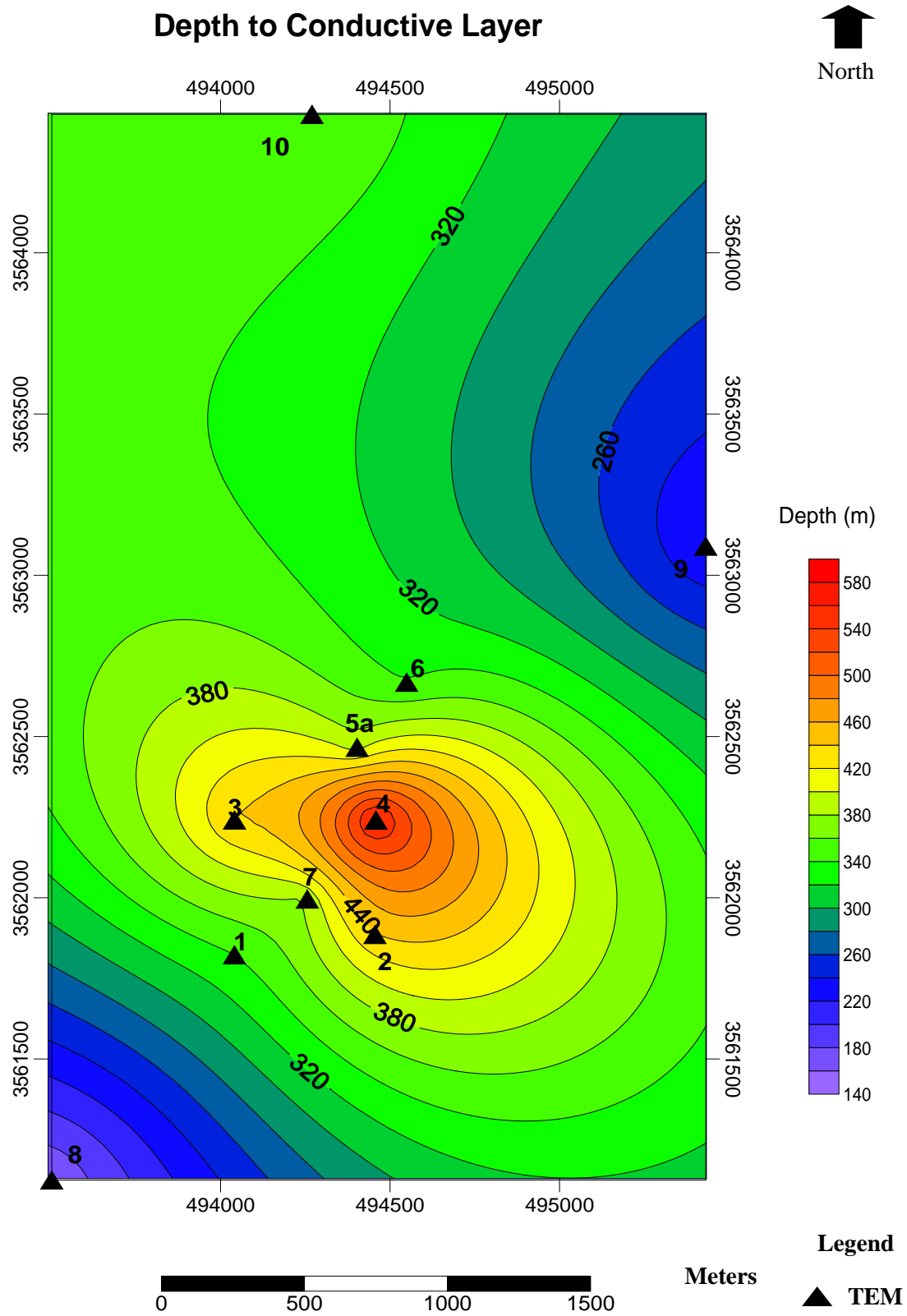
Figure 6.19: Depth to Conductive Layer from the surface based on TEM data.
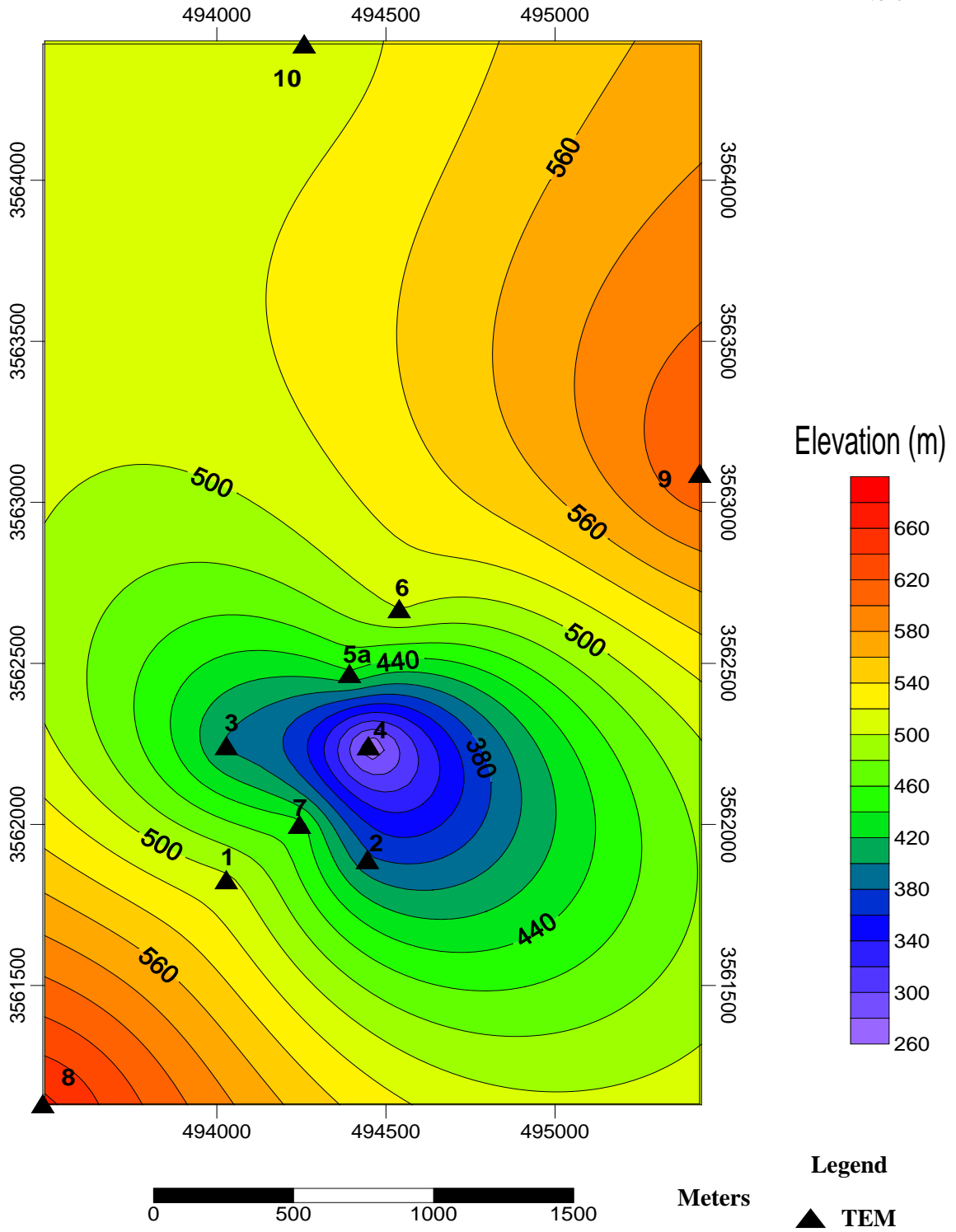
Figure 6.20: Elevation of Conductive Layer above sea level based on TEM data.
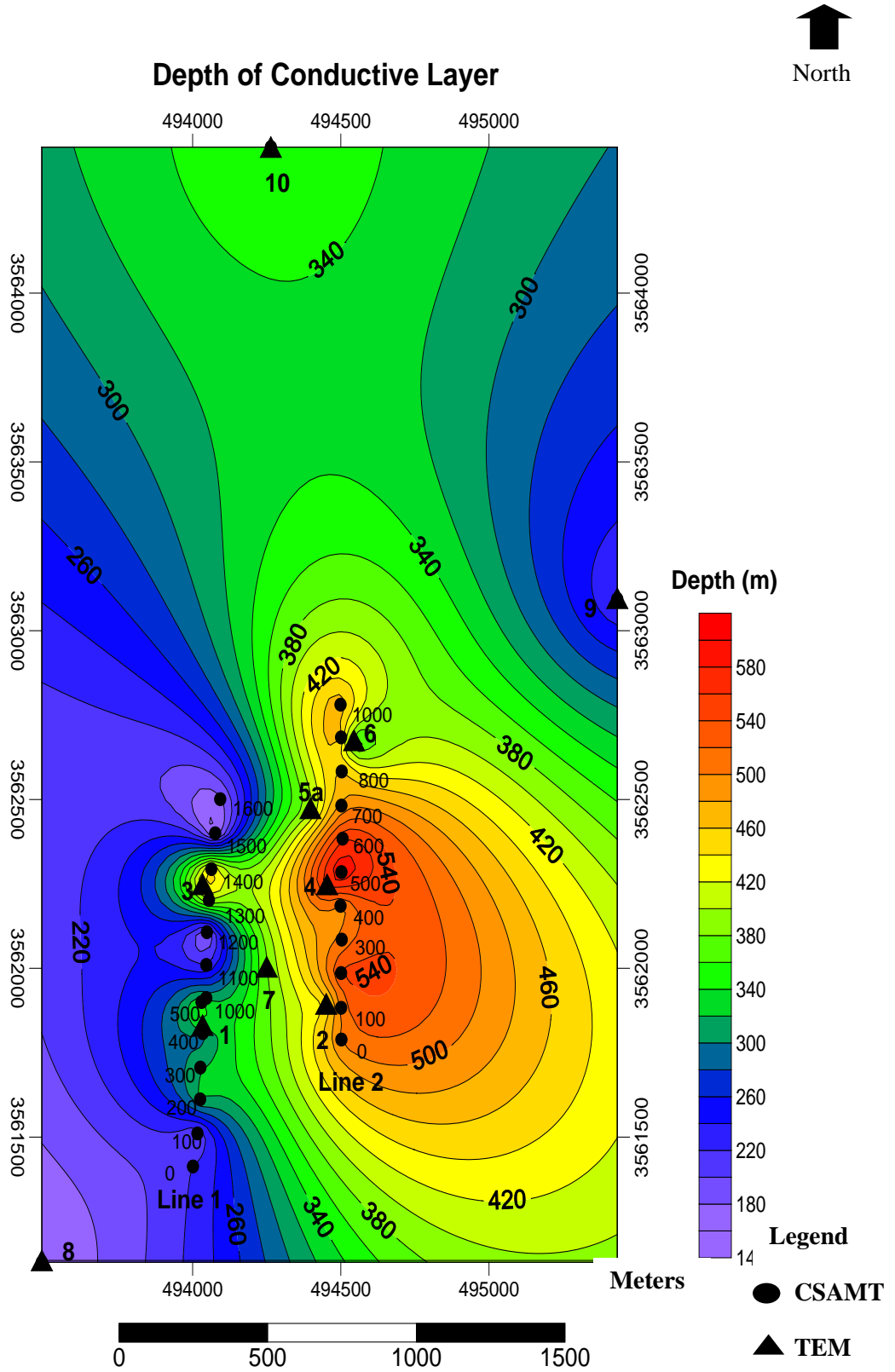
Figure 6.21: Depth of Conductive Layer from the surface based on CSAMT and TEM data.
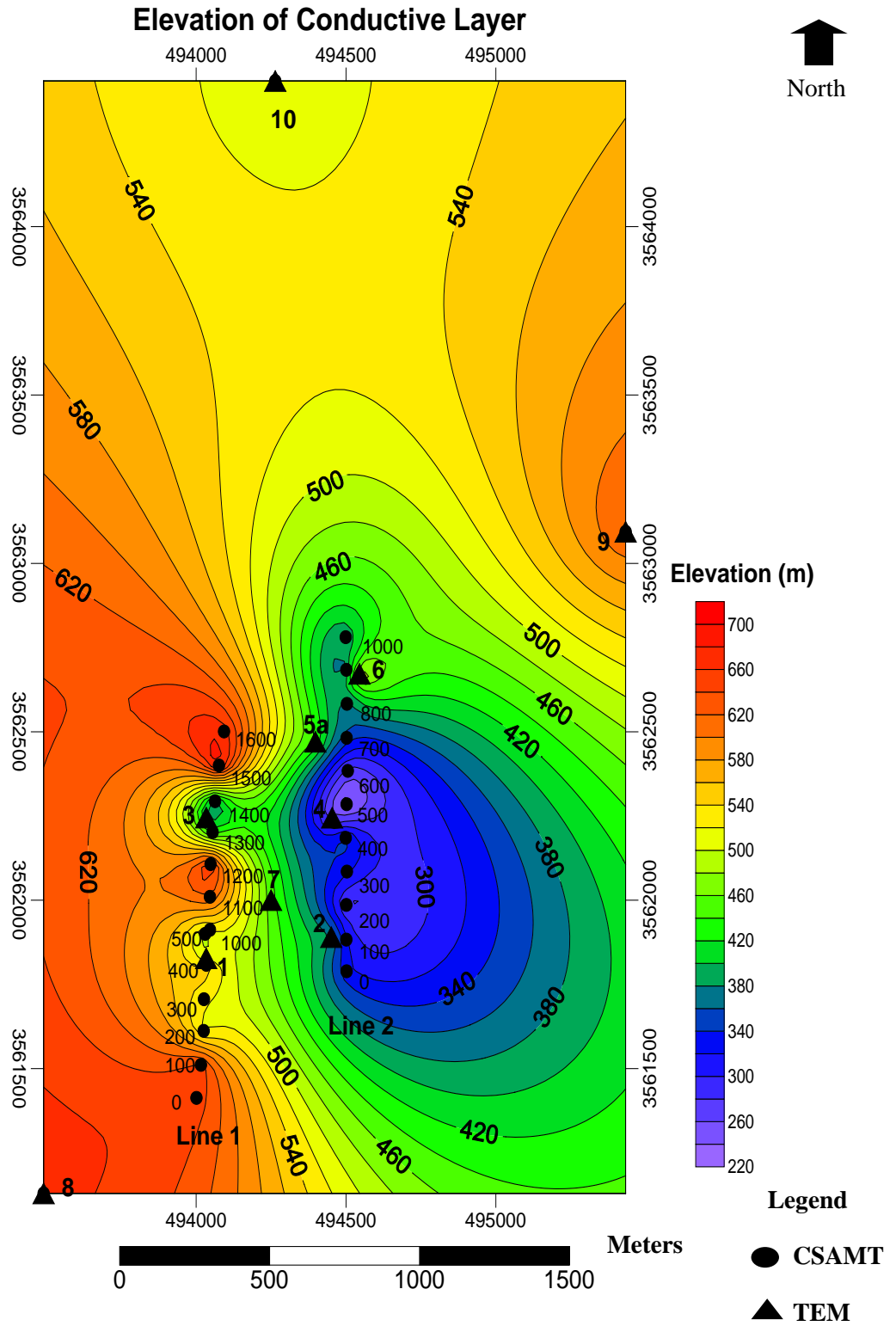
Figure 6.22: Elevation of Conductive Layer above sea level based on CSAMT and TEM data.
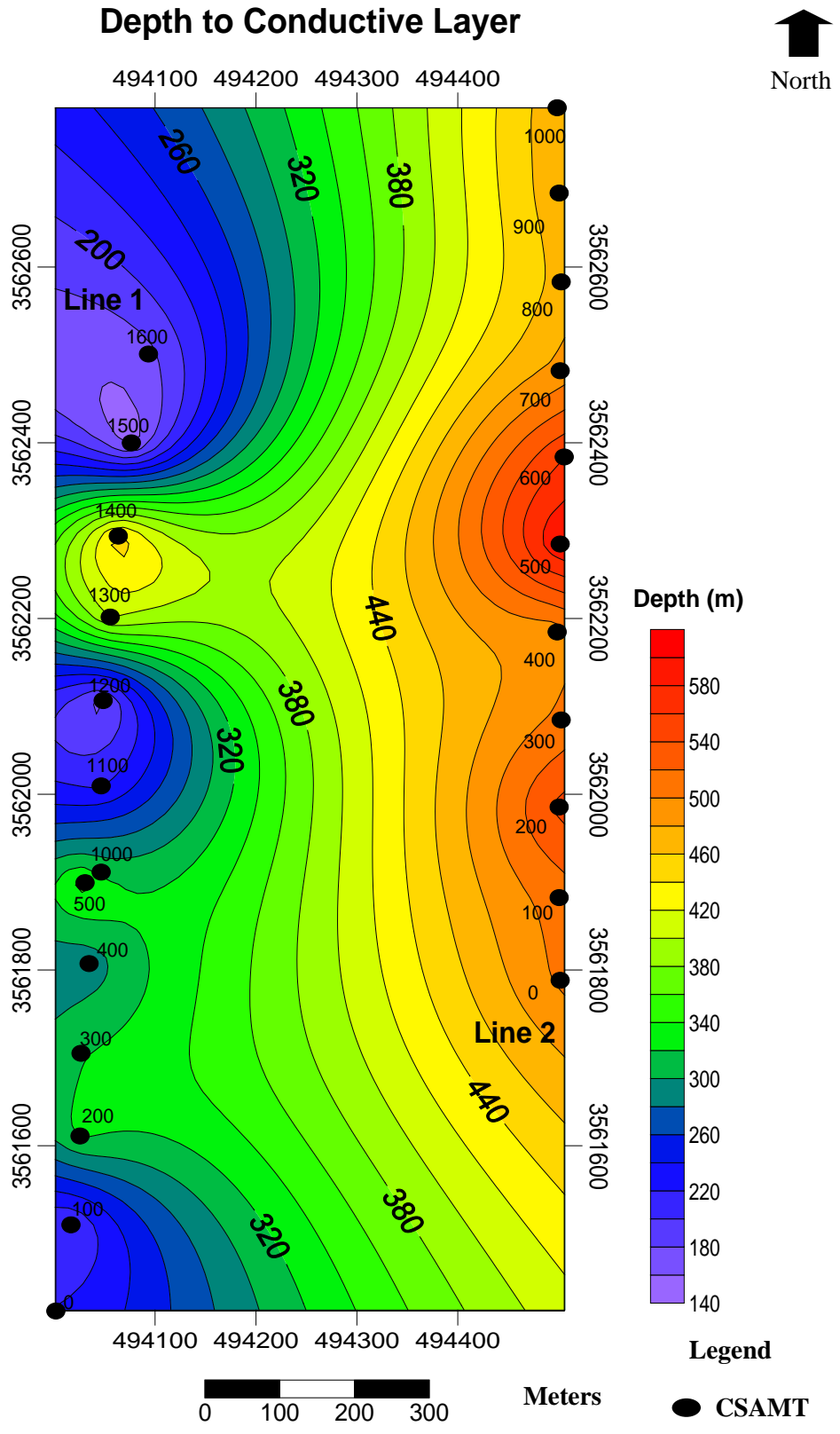
Figure 6.23: Depth to Conductive Layer from the surface based on CSAMT data.
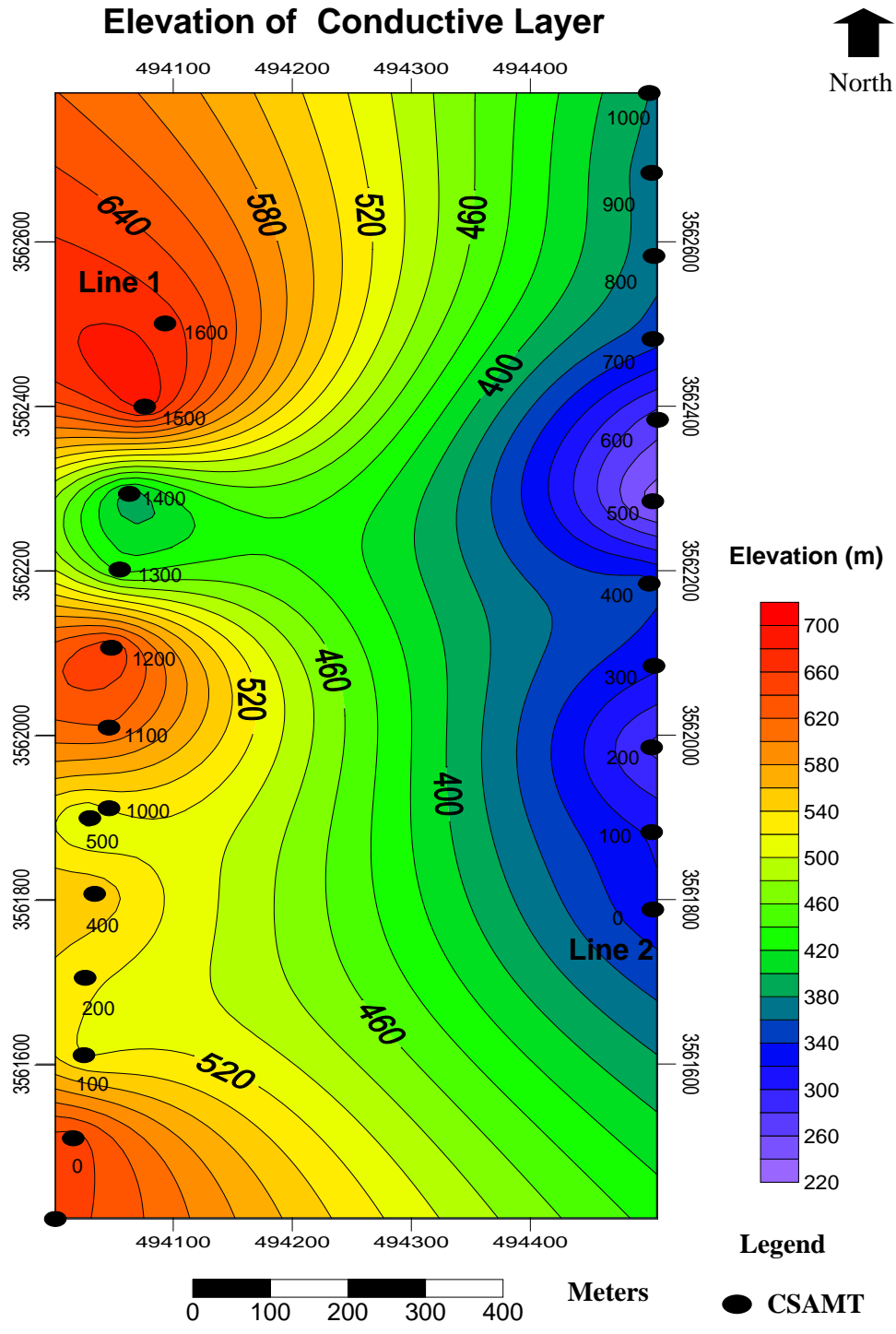
Figure 6.24: Elevation of Conductive Layer above sea level based on CSAMT data.

Station No.	Easting (m)	Northing (m)	Elevation (m)	Elevation of conductive layer (m)	Depth to conductive layer (m)
1	494033	3561827	844	504	340
2	494451	3561890	823	383	440
3	494034	3562245	836	396	440
4	494454	3562245	830	260	570
5a	494398	3562470	830	440	390
6	494545	3562672	842	502	340
7	494250	3562000	828	448	380
8	493491	3561129	826	666	160
9	495433	3563094	840	620	220
10	494264	3564432	866	506	360

Table 6.1 Data of conductive layer from TEM.

Station No.	Easting (m)	Northing (m)	Elevation (m)	Elevation of conductive layer (m)	Depth to conductive layer (m)
1000	494046	3561912	837	525	312
1100	494046	3562010	837	620	217
1200	494048	3562107	833	660	173
1300	494055	3562202	833	430	403
1400	494063	3562294	835	385	450
1500	494076	3562400	845	695	150
1600	494093	3562501	844	670	174

Table 6.2 Data of conductive layer from Line 1 North of CSAMT.

Station No.	Easting (m)	Northing (m)	Elevation (m)	Elevation of conductive layer (m)	Depth to conductive layer (m)
0	494001	3561413	871	650	221
100	494016	3561511	848	650	198
200	494025	3561612	840	515	325
300	494026	3561706	843	525	318
400	494034	3561808	842	555	287
500	494030	3561900	840	490	350

Table 6.3 Data of conductive layer from Line 1 South of CSAMT.

Station No.	Easting (m)	Northing (m)	Elevation (m)	Elevation of conductive layer (m)	Depth to conductive layer (m)
0	494502	3561789	829	325	504
100	494501	3561883	827	318	509
200	494501	3561986	821	275	546
300	494503	3562085	830	325	505
400	494499	3562185	839	350	489
500	494502	3562285	830	230	600
600	494506	3562384	830	270	560
700	494502	3562482	837	350	487
800	494503	3562583	837	370	467
900	494501	3562684	844	370	474
1000	494499	3562781	854	380	474

Table 6.4 Data of conductive layer from Line 2 of CSAMT.

6.2 Conclusions

The CSAMT survey is generally in agreement with the geological interpretation of Lipman, 1993. The TEM and CSAMT surveys agree with the hypothesized geologic cross section in terms of the thickness of the welded (Kcw) and partly welded (Kcm) to non-welded (Kcn) volcanics, which overlay deeper sedimentary rocks (Ku). Interpreted faults and their proposed displacement were also detected with these methods and the results show a positive correlation with Lipman's interpretation. The TEM and CSAMT electrical resistivity data clearly show the presence of a deep conductive layer, below the resistive volcanic sequence, which is best illustrated on cross section F_1-F_1' (Figure 6.18).

Subsurface geological information can be determined by the CSAMT data. The central fault in cross section F_1-F_1' correlated with the zone where the resistivity contour lines tend to gather together. On the other hand, the large homogeneous zone where the resistivity doesn't change frequently shows the same type of rock without geological structure.

From the CSAMT data, some geological information can be determined based on the changing resistivity. Since different lithology may correlate with different resistivity, the depth and thickness of certain kinds of rock can be determined by the resistivity values given by CSAMT data. Compared to the TEM survey, the CSAMT data provides more detailed information about the thickness of the rock formations and more accurate information about distribution of different types of rocks along each profile line.

However, the CSAMT data was significantly affected by the pipeline. From Figure 5.9, the northern sections of both lines 1 and 2 are dominated by the pipeline response.

Attempts to accurately model the pipeline effect and remove the pipeline effect from the

cross sections were not successful.

References

Avanesians, Patrick, G. A. Daroch, J. Fleming, S. A. Hundt, S. C. Leake, L. Ojha, B. K. Sternberg, D. F. Wampler, 2011, Geophysical investigation of the Tucson Mountains: Geophysical field camp 2011 LASI -11-1, University of Arizona, Laboratory for Advanced Subsurface Imaging, Tucson, AZ.

Golden Software, Surfer v8, http://www.goldensoftware.com/products/surfer/surfer.shtml , accessed March 9, 2012.

Lipman, Peter W., 1993, Geologic map of the Tucson Mountain Caldera, Southern Arizona, USGS miscellaneous investigation series, Map I-2205.

Loke, M. H., 1999, Electrical imaging surveys for environmental and engineering studies: A practical guide to 2-D and 3-D surveys, 4-5, accessed April 27, 2012; http://www.georentals.co.uk/Lokenote.pdf

McCoy, Scott Jr., 1964, A description of the limestone blocks of the Tucson Mountain Chaos Pima County, Arizona: M.S. thesis, University of Arizona.

Ricks, Adam, 2012, Personal communication: Central Arizona Project, Phoenix, AZ.

Zonge International,2009, Introduction to CSAMT, http://www.zonge.com/PDF_Papers/Intro_CSAMT.pdf, accessed March 10, 2012.

Zonge International, Equipment, http://www.zonge.com/Equipment.html, accessed March 15, 2012.

Zonge International, Software: Data processing and modeling software,

http://zonge.com/DataPrograms.html, accessed March 2, 2012.

Appendix

A. Raw sounding data

1. Line 1 North

2. Line 2

3. Line 1 North - Pre-RF filter

B. SCS2D Best-Fit Model

1. Line 1 North

2. Line 2

Appendix A

Figures 4.1 through 4.25 are the raw sounding data plots for each frequency from Line 1 North and Line 2. The green points indicate the calculated apparent resistivity, using up to the 5th harmonic. The black points indicate the average apparent resistivity per frequency. The alternate colors reflect the CSAVGW program application of statistical analysis to identify outliers. All the sounding data for each frequency were interpreted by the user, and some points were omitted, adjusting the average and overall coherency of the dipole trend.
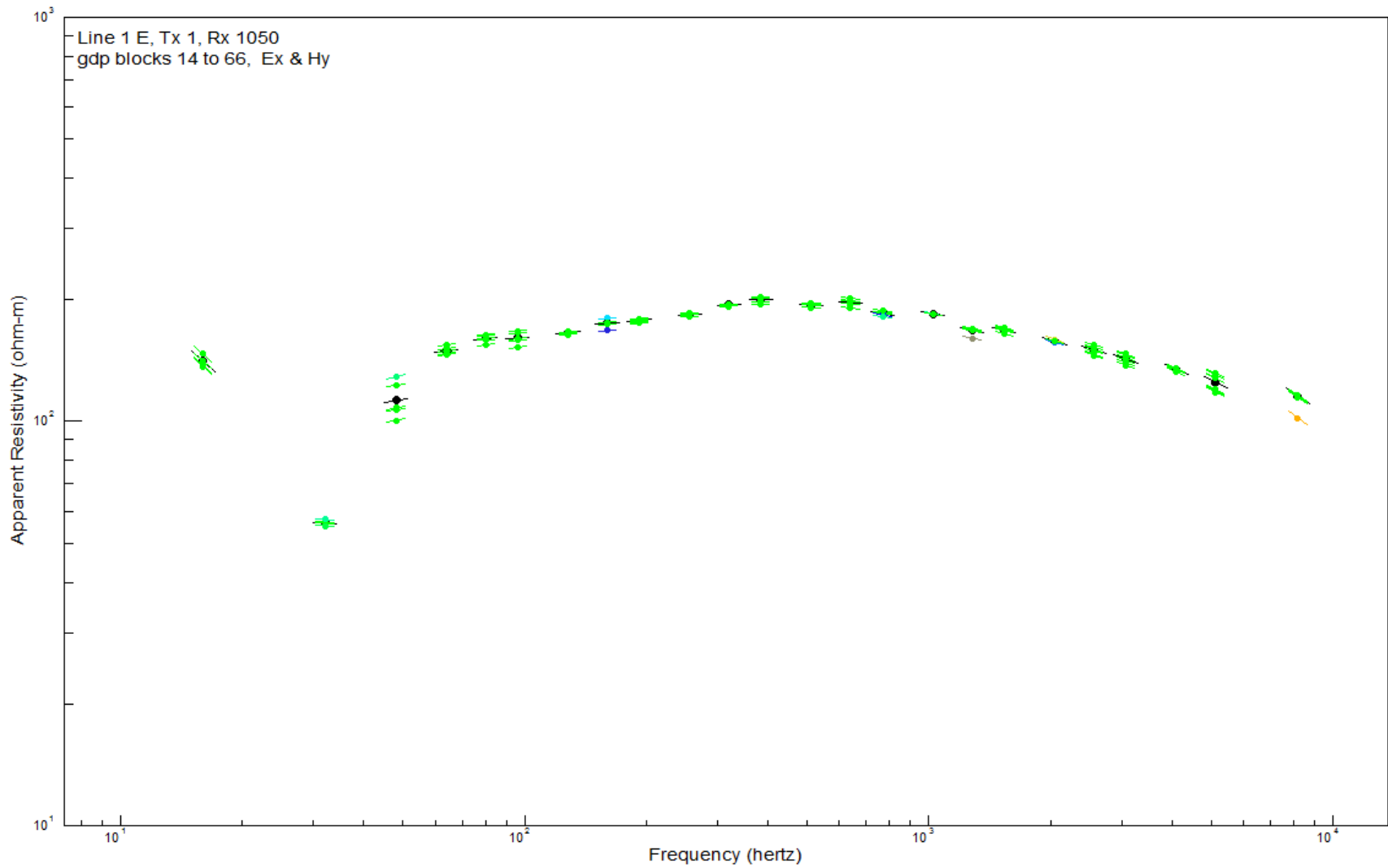
Appendix 4.1 : Line 1 raw sounding data, observing up to the 5th harmonic. Dipole 1050.
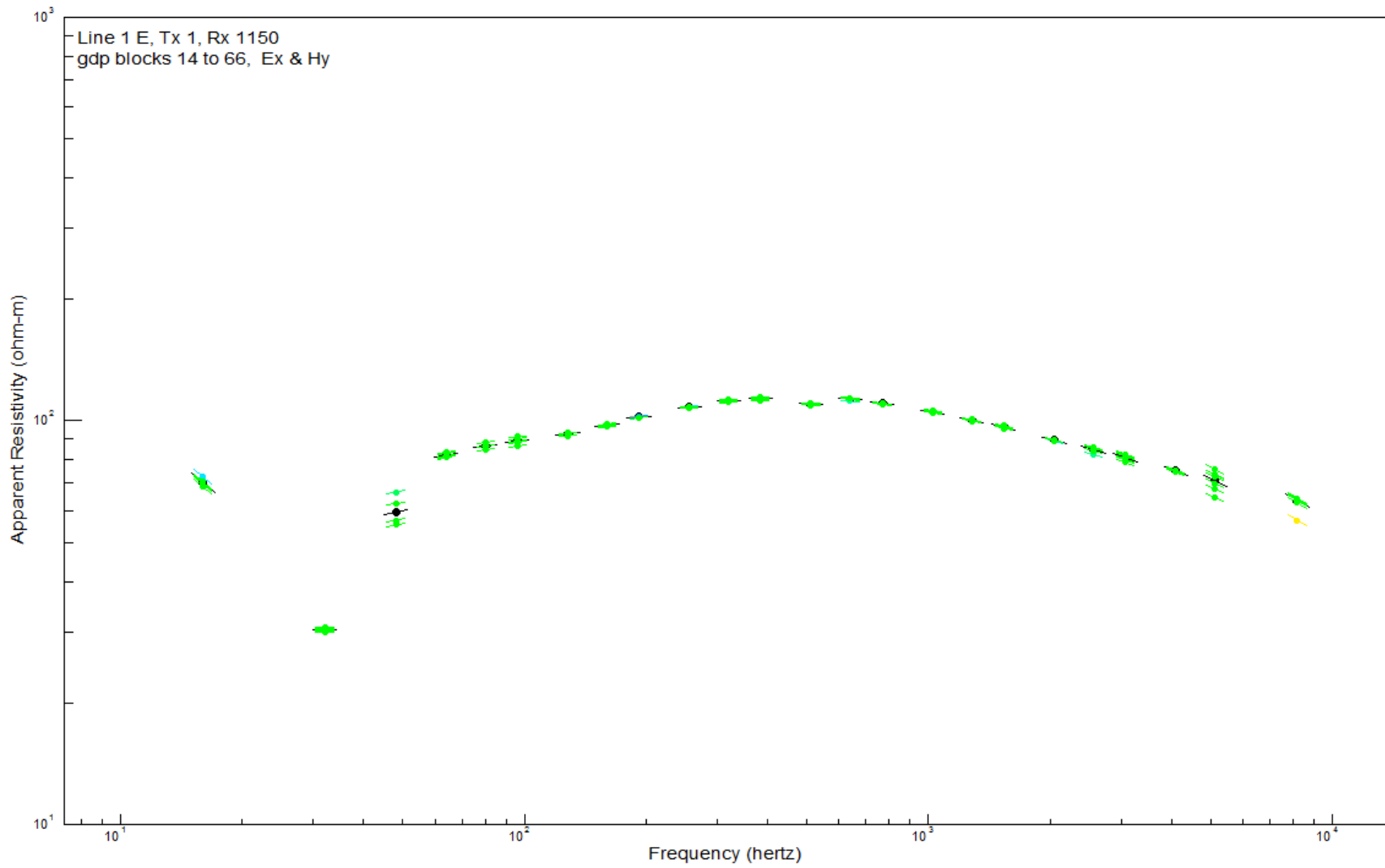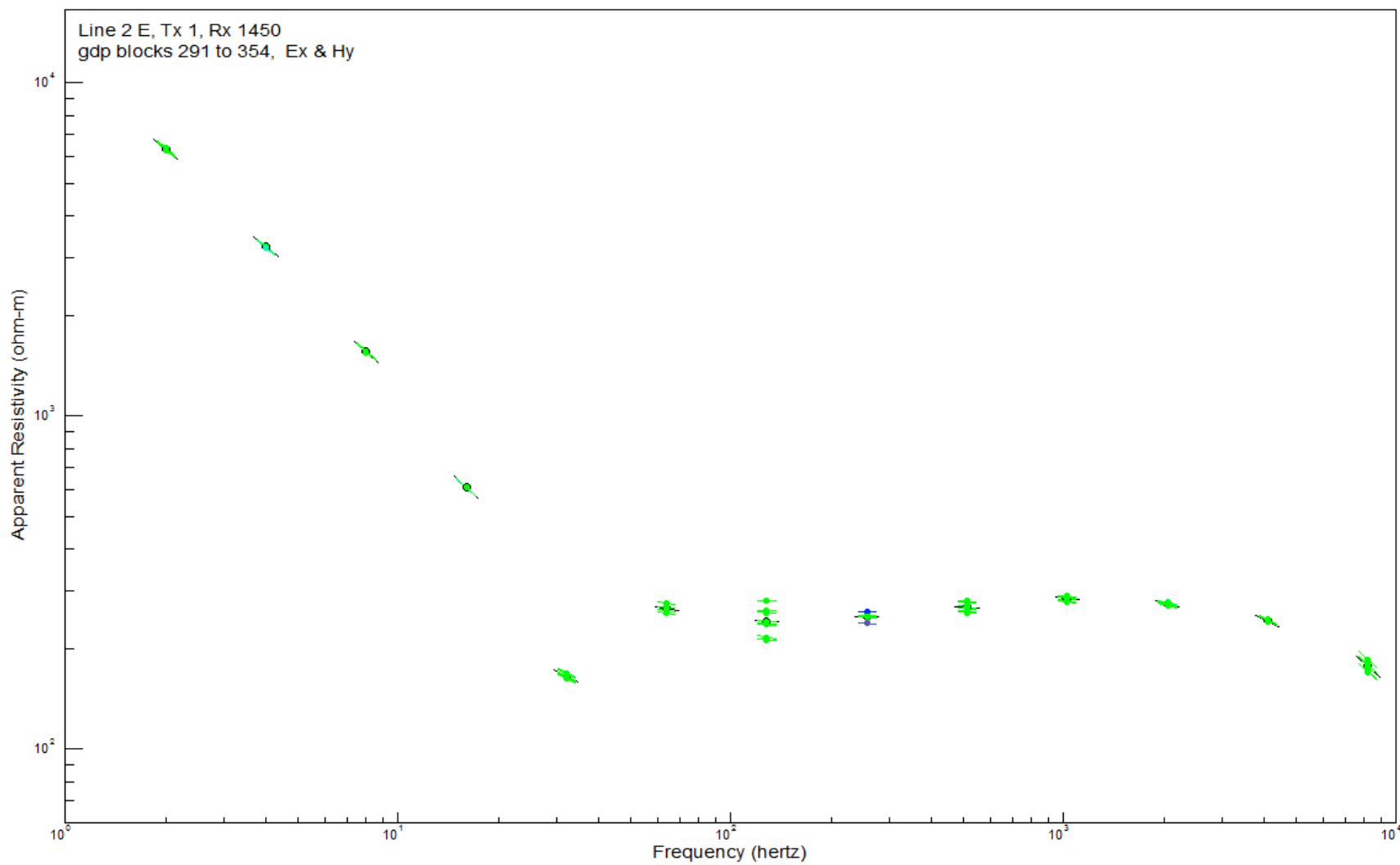
Appendix 4.2 : Line 1 raw sounding data, observing up to the 5th harmonic. Dipole 1150.
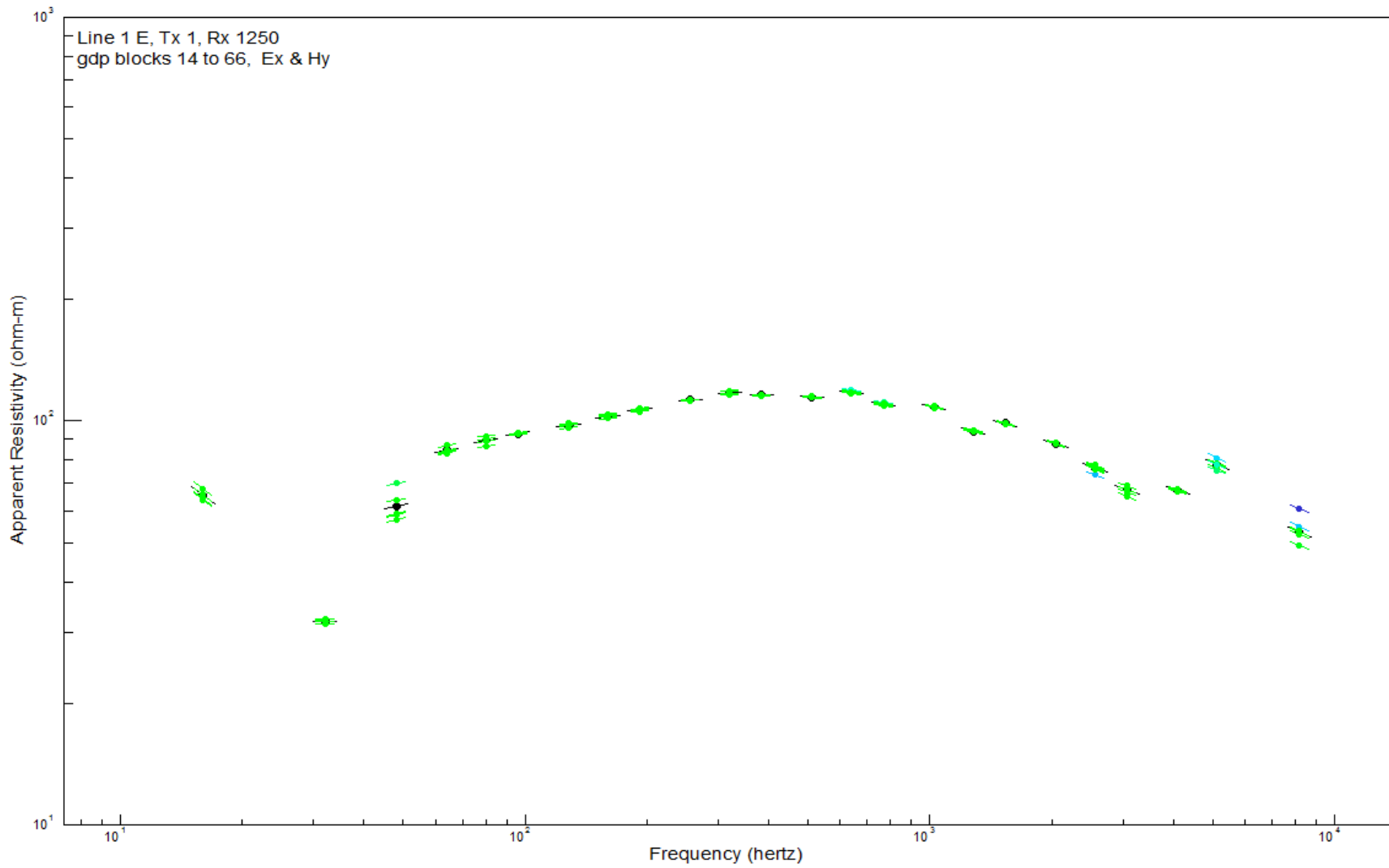
Appendix 4.3 : Line 1 raw sounding data, observing up to the 5th harmonic. Dipole 1250.
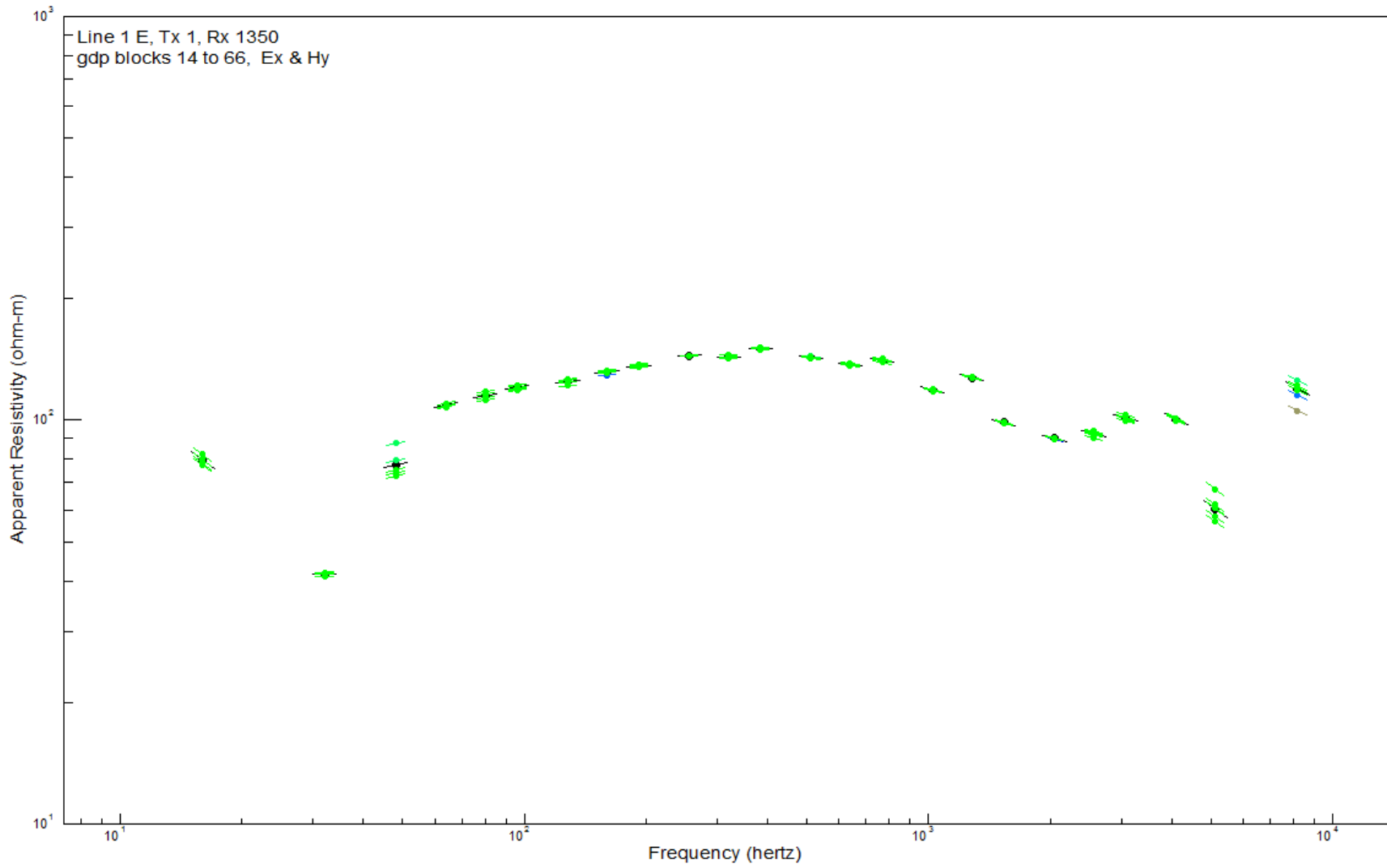
Appendix 4.4 : Line 1 raw sounding data, observing up to the 5th harmonic. Dipole 1350.
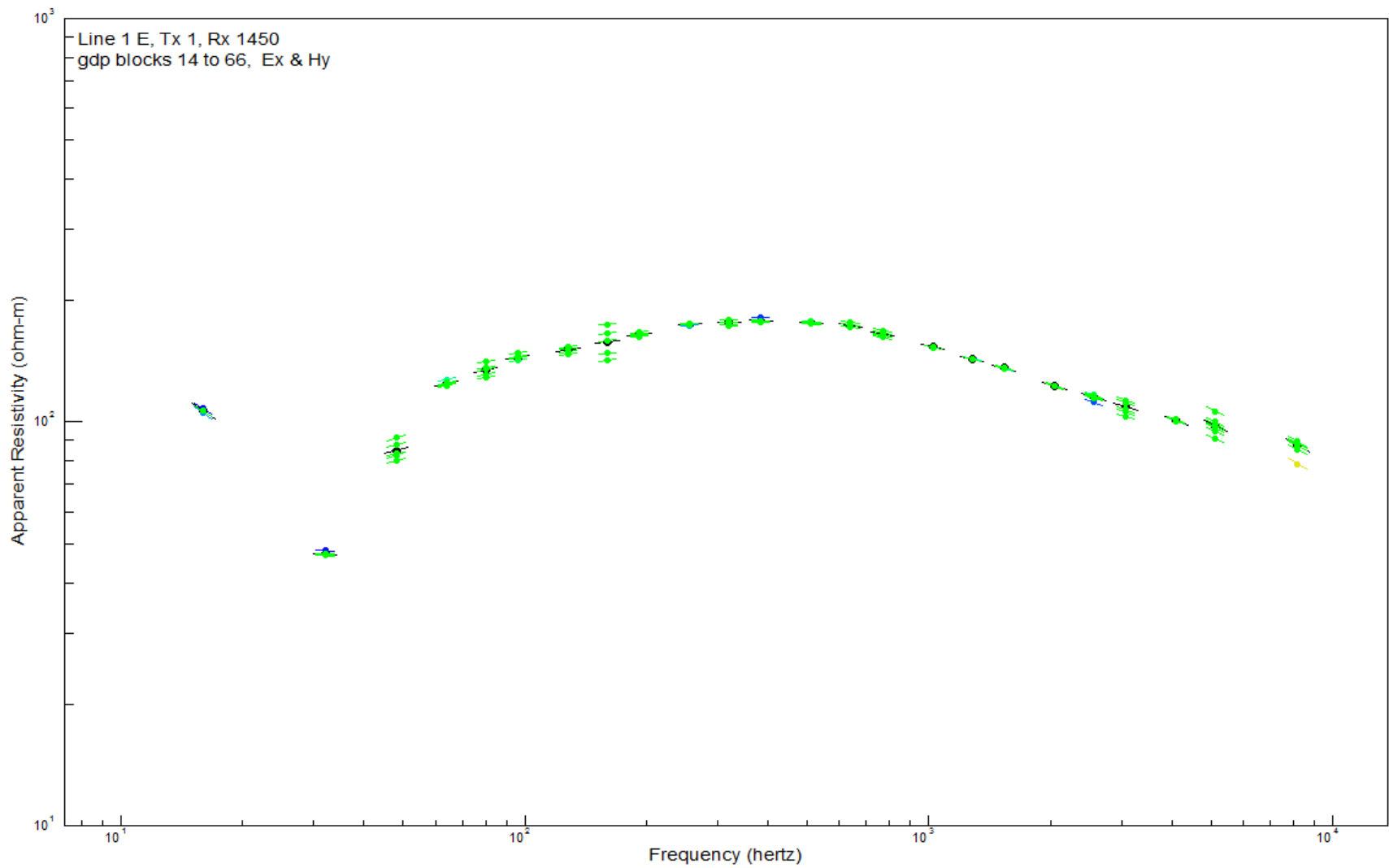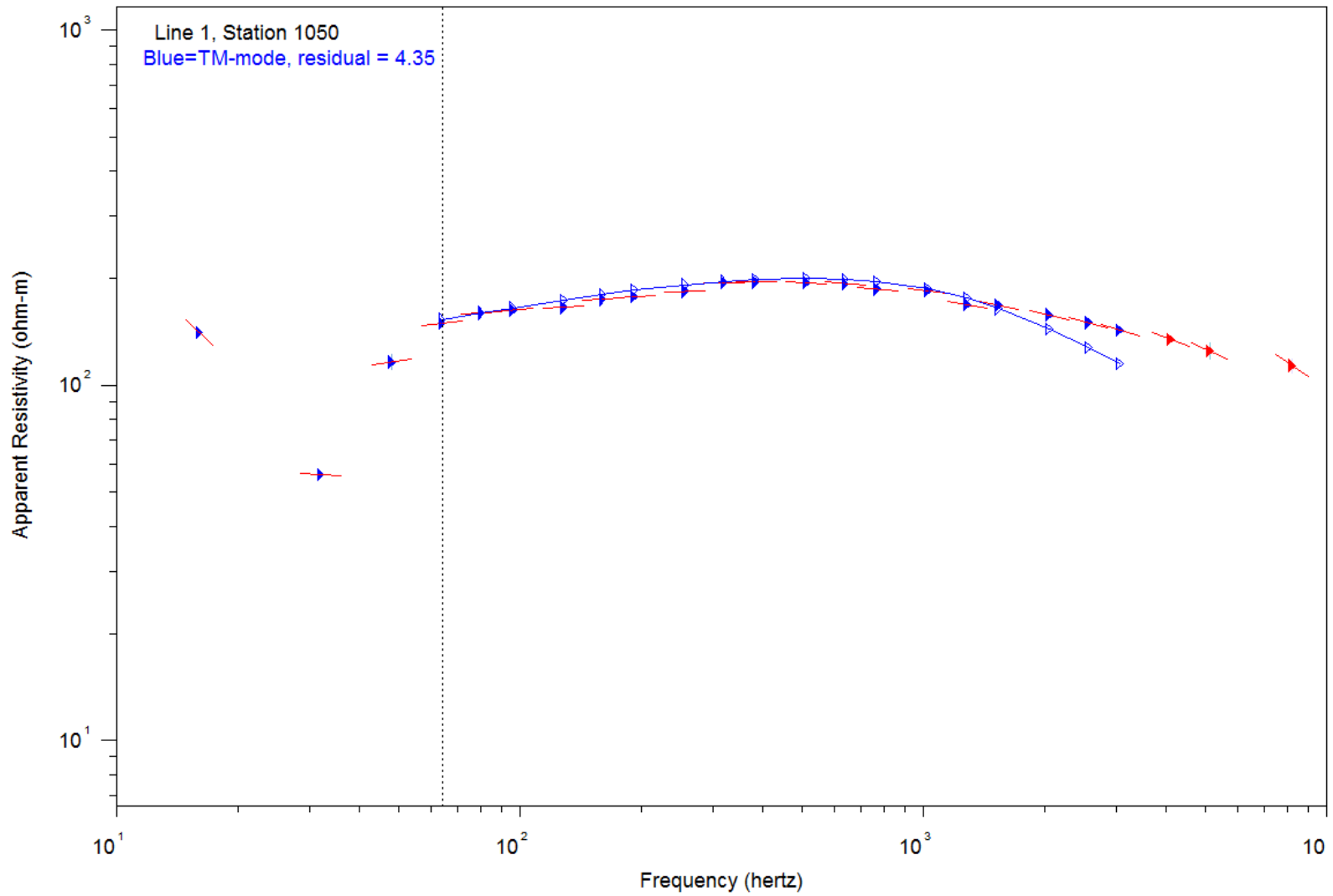
Appendix 4.5 : Line 1 raw sounding data, observing up to the 5th harmonic. Dipole 1450.

Line 1 E, Tx 1, Rx 1550
gdp blocks 78 to 132, Ex & Hy
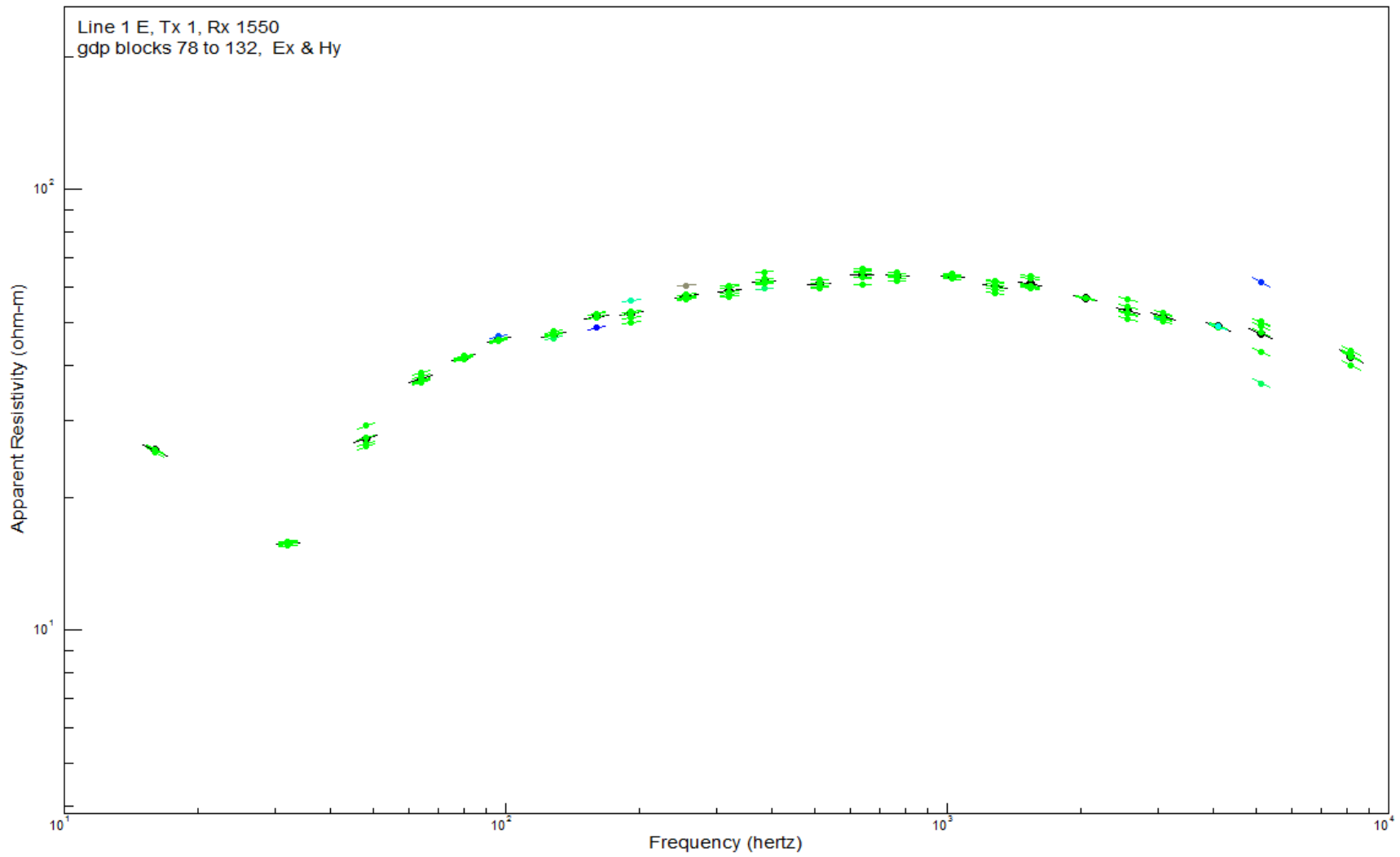
Appendix 4.6 : Line 1 raw sounding data, observing up to the 5th harmonic. Dipole 1550.
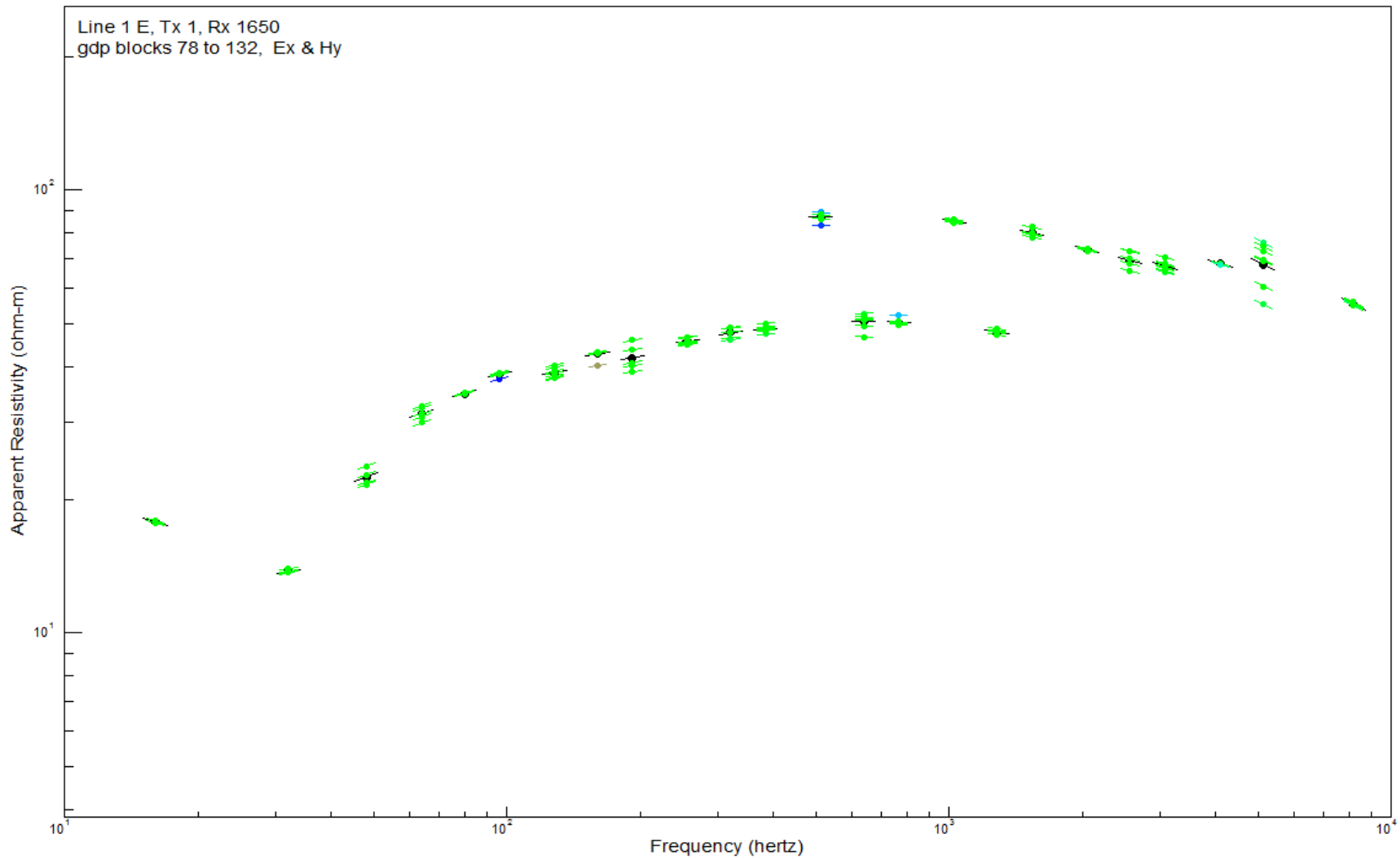
Appendix 4.7 : Line 1 raw sounding data, observing up to the 5th harmonic. Dipole 1650.
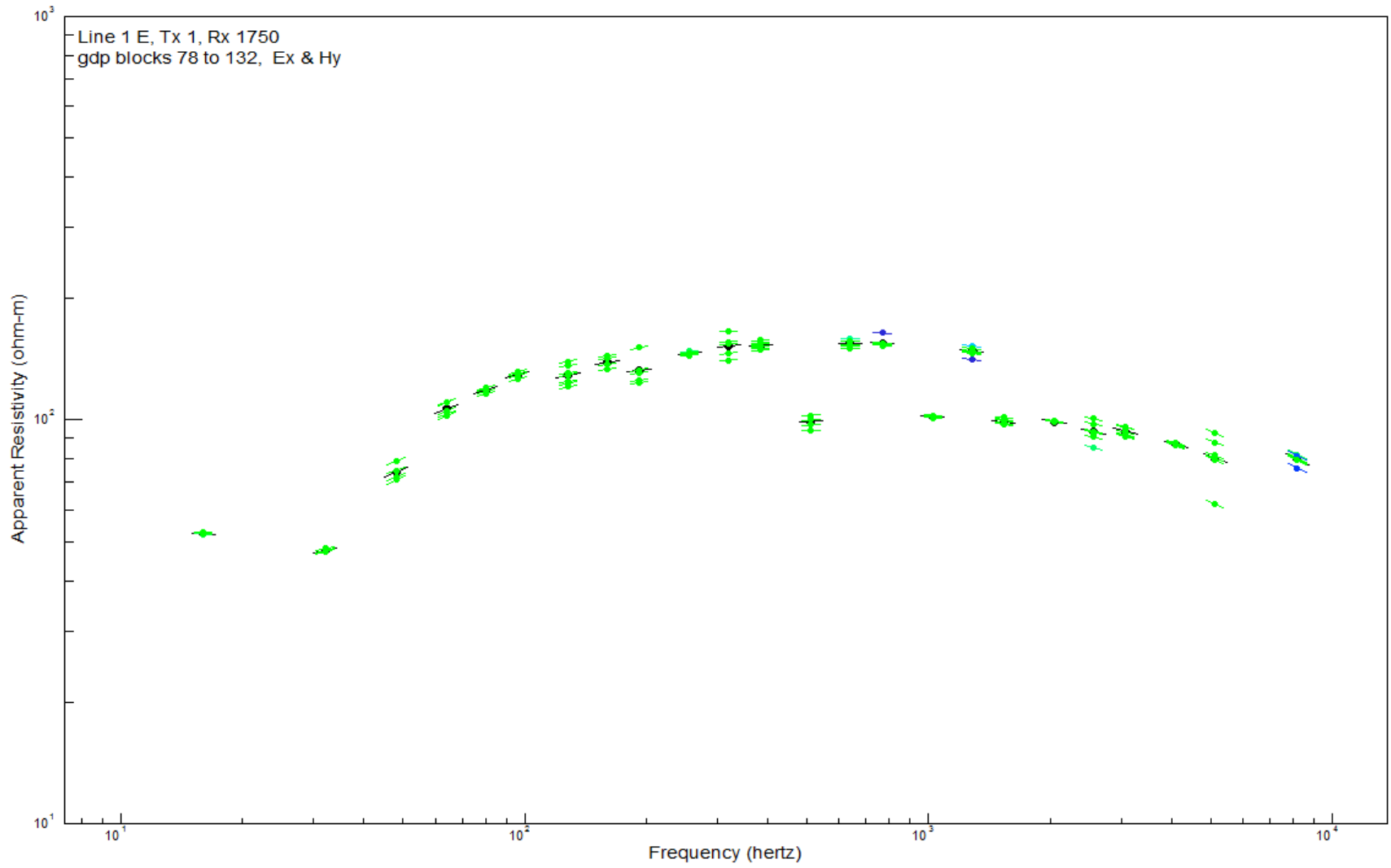
Appendix 4.8 : Line 1 raw sounding data, observing up to the 5th harmonic. Dipole 1750.
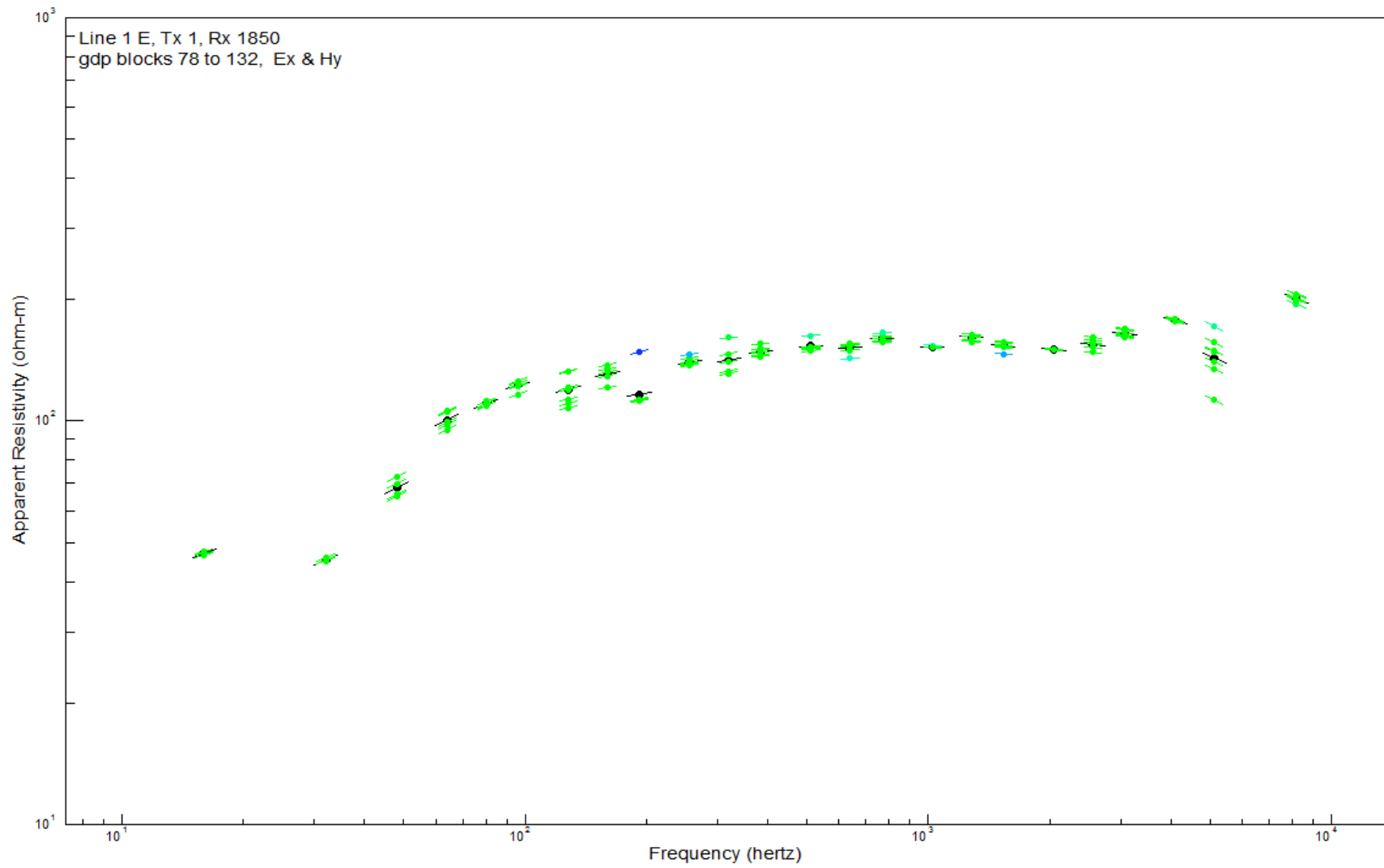
Appendix 4.9 : Line 1 raw sounding data, observing up to the 5th harmonic. Dipole 1850.
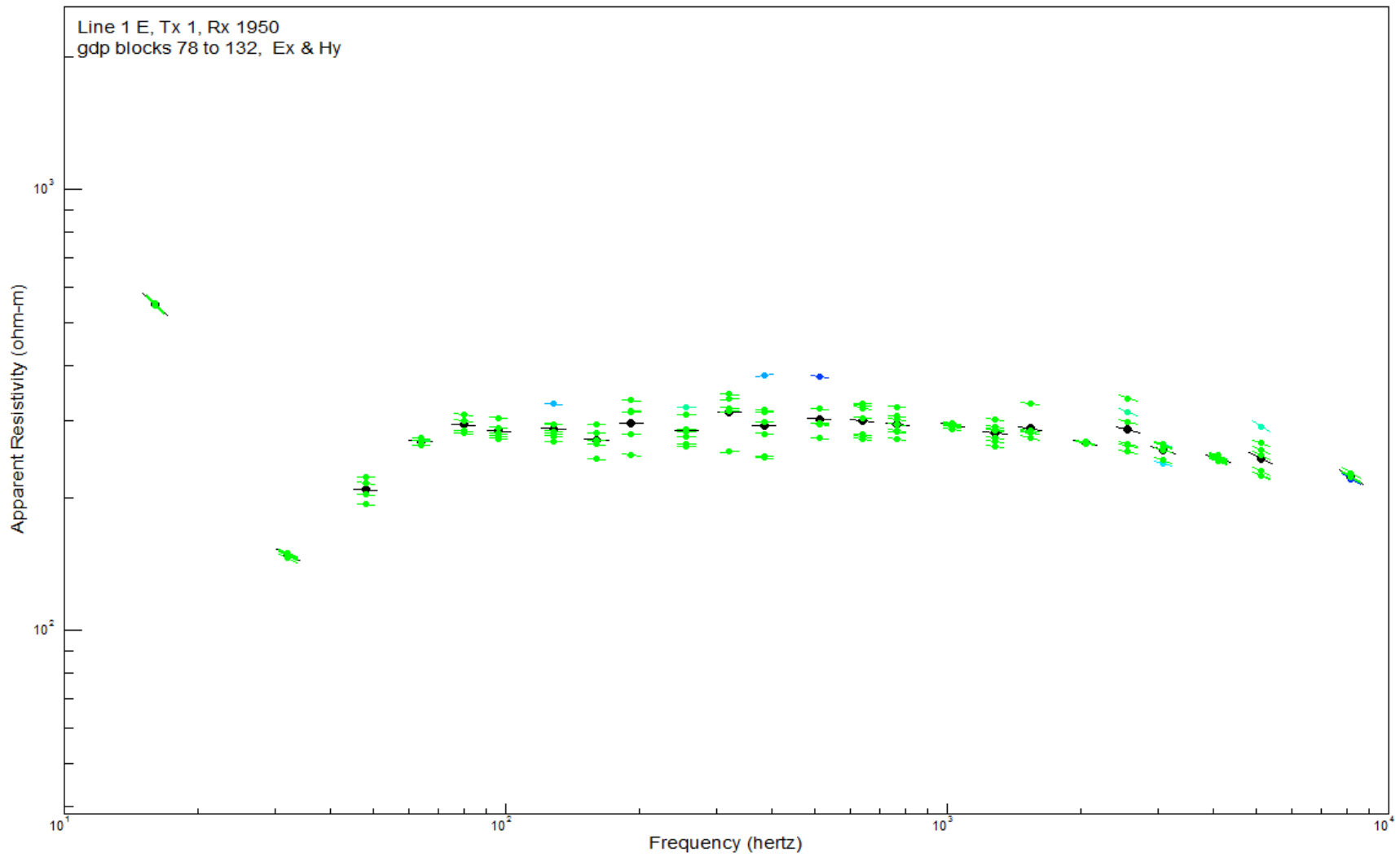
Appendix 4.10 : Line 1 raw sounding data, observing up to the 5th harmonic. Dipole 1950.
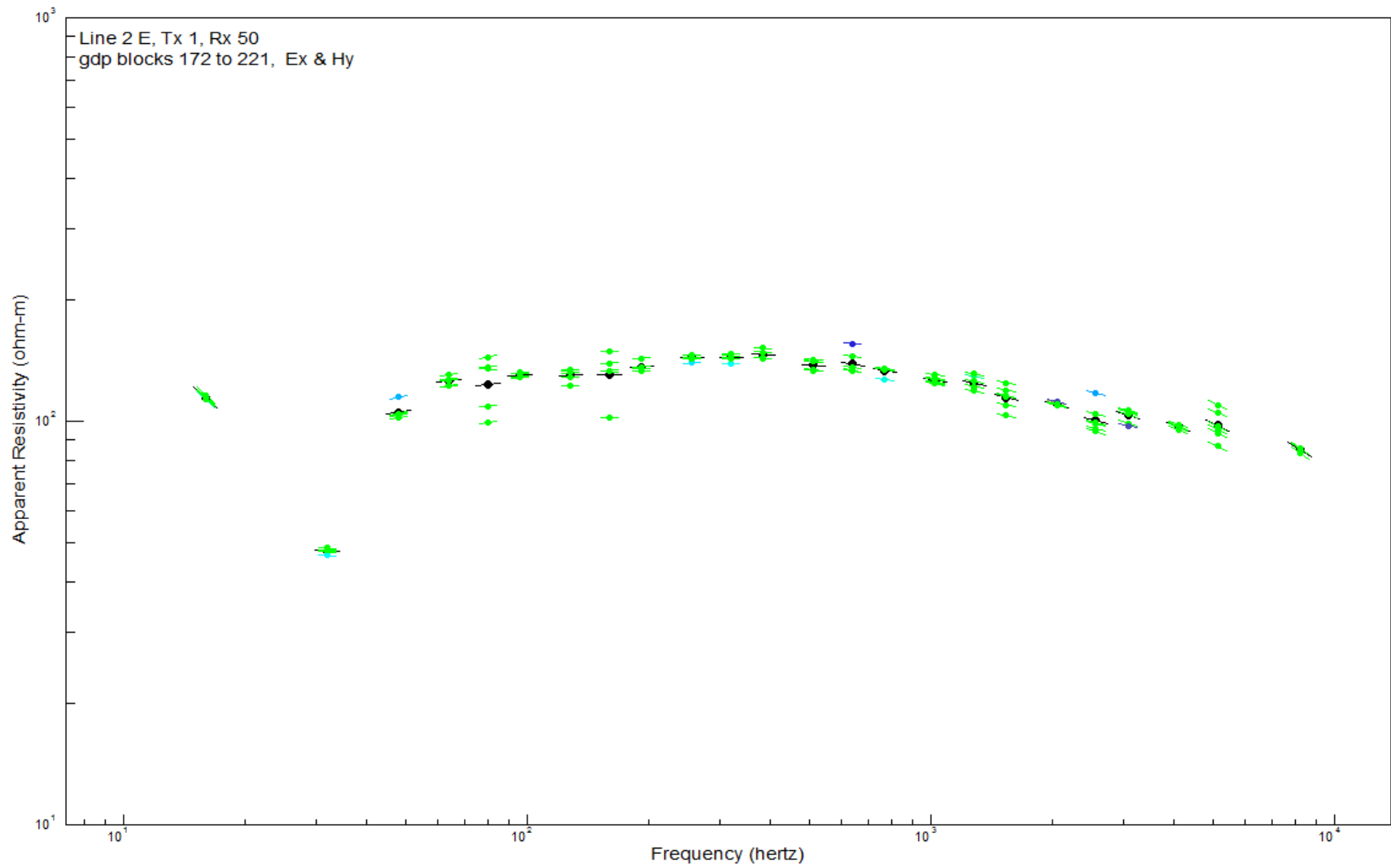
Appendix 4.11 : Line 2 raw sounding data, observing up to the 5th harmonic. Dipole 50.
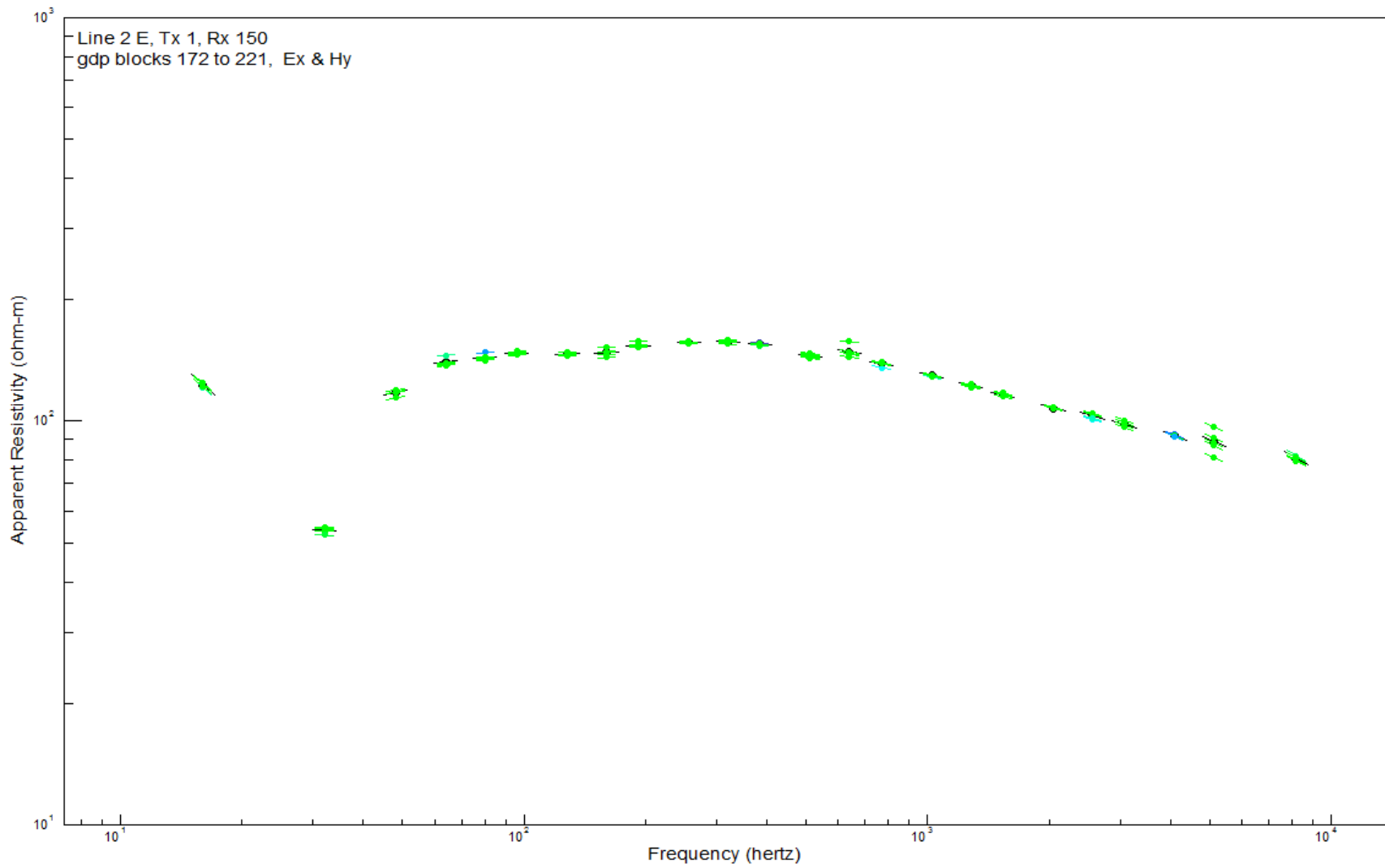
Appendix 4.12 : Line 2 raw sounding data, observing up to the 5th harmonic. Dipole 150.
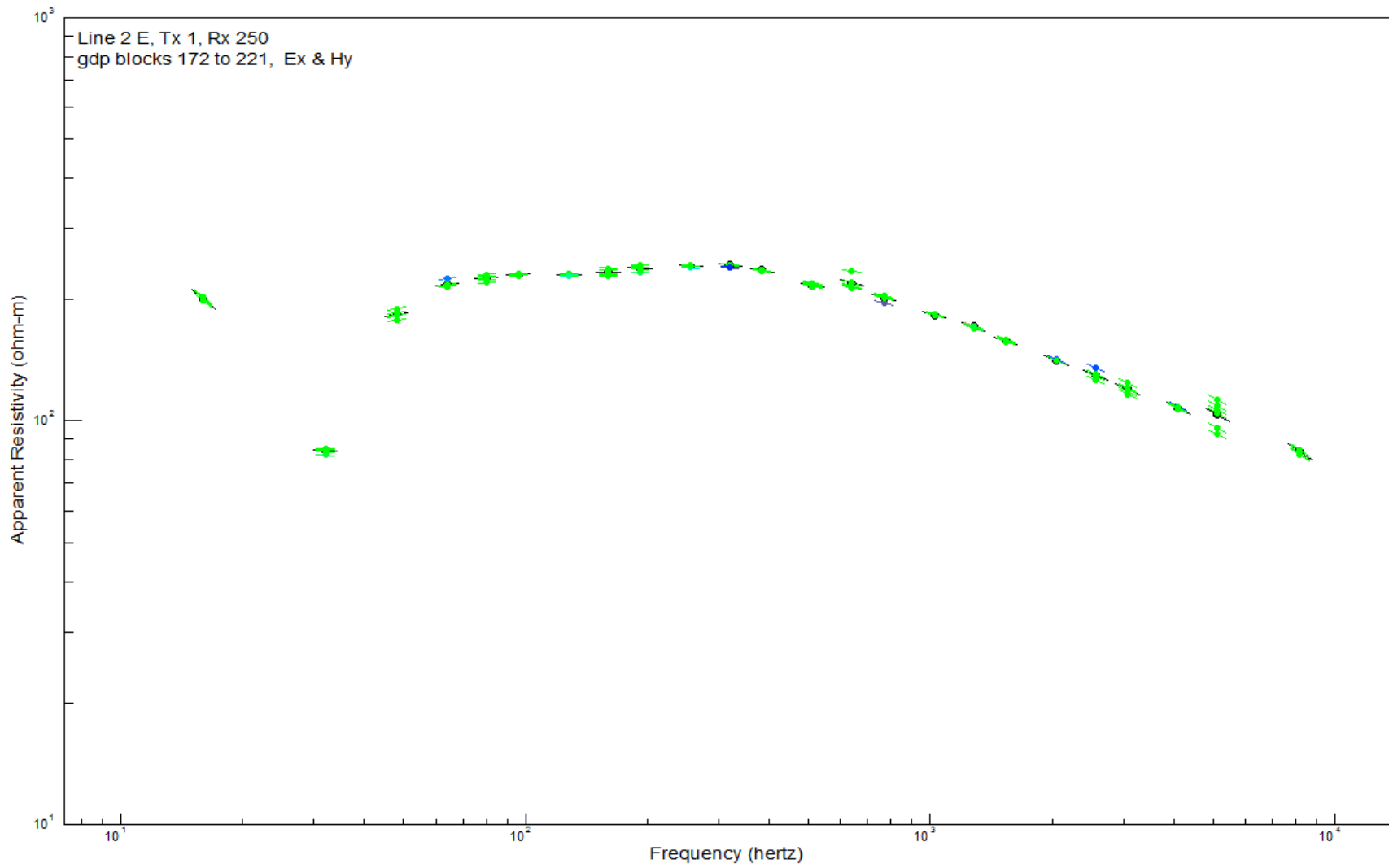
Appendix 4.13 : Line 2 raw sounding data, observing up to the 5th harmonic. Dipole 250.

The chart shows:
- Title: Line 2 E, Tx 1, Rx 250
- Subtitle: gdp blocks 172 to 221, Ex & Hy
- Y-axis: Apparent Resistivity (ohm-m)
- X-axis: Frequency (hertz)
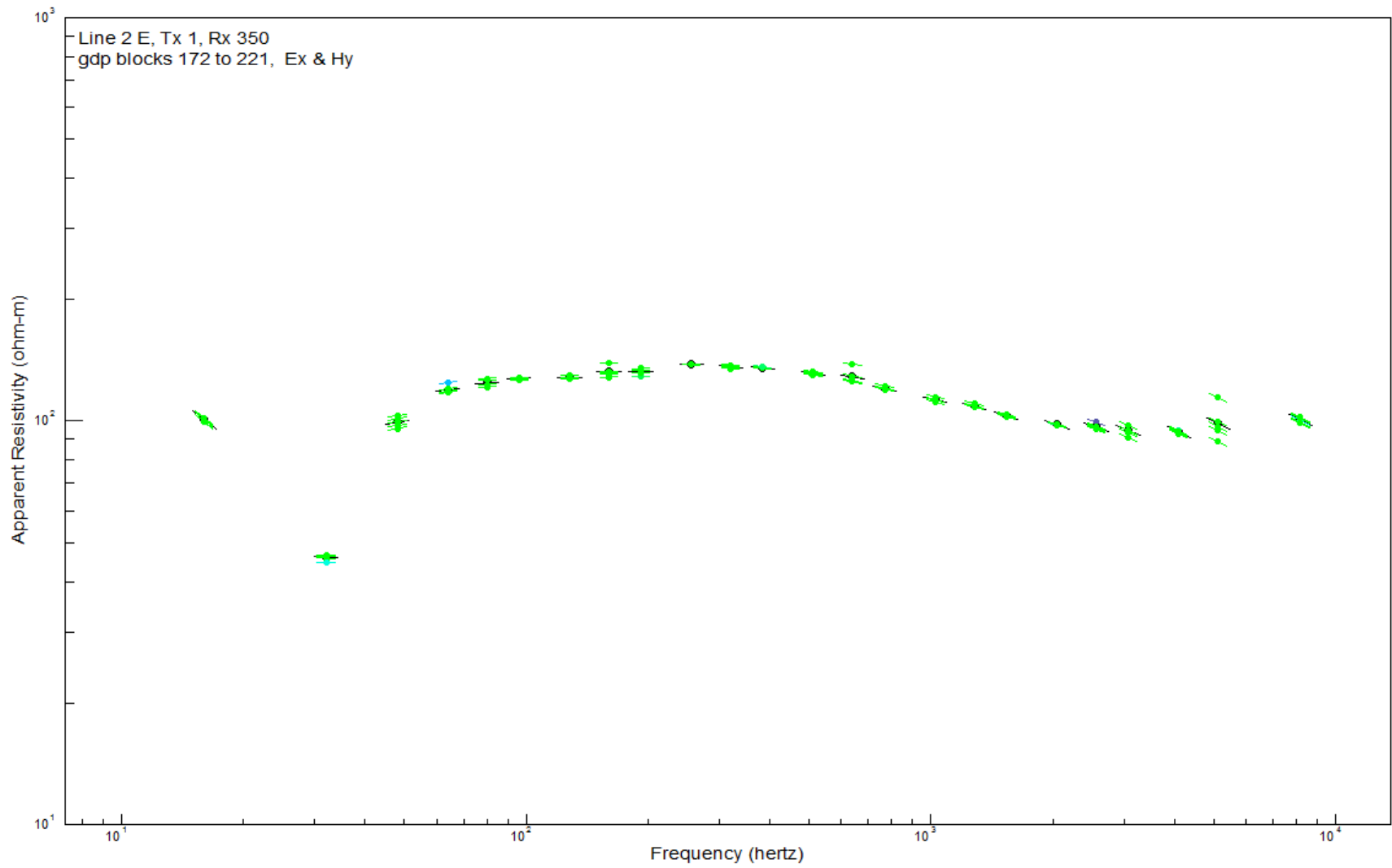
Appendix 4.14 : Line 2 raw sounding data, observing up to the 5th harmonic. Dipole 350.
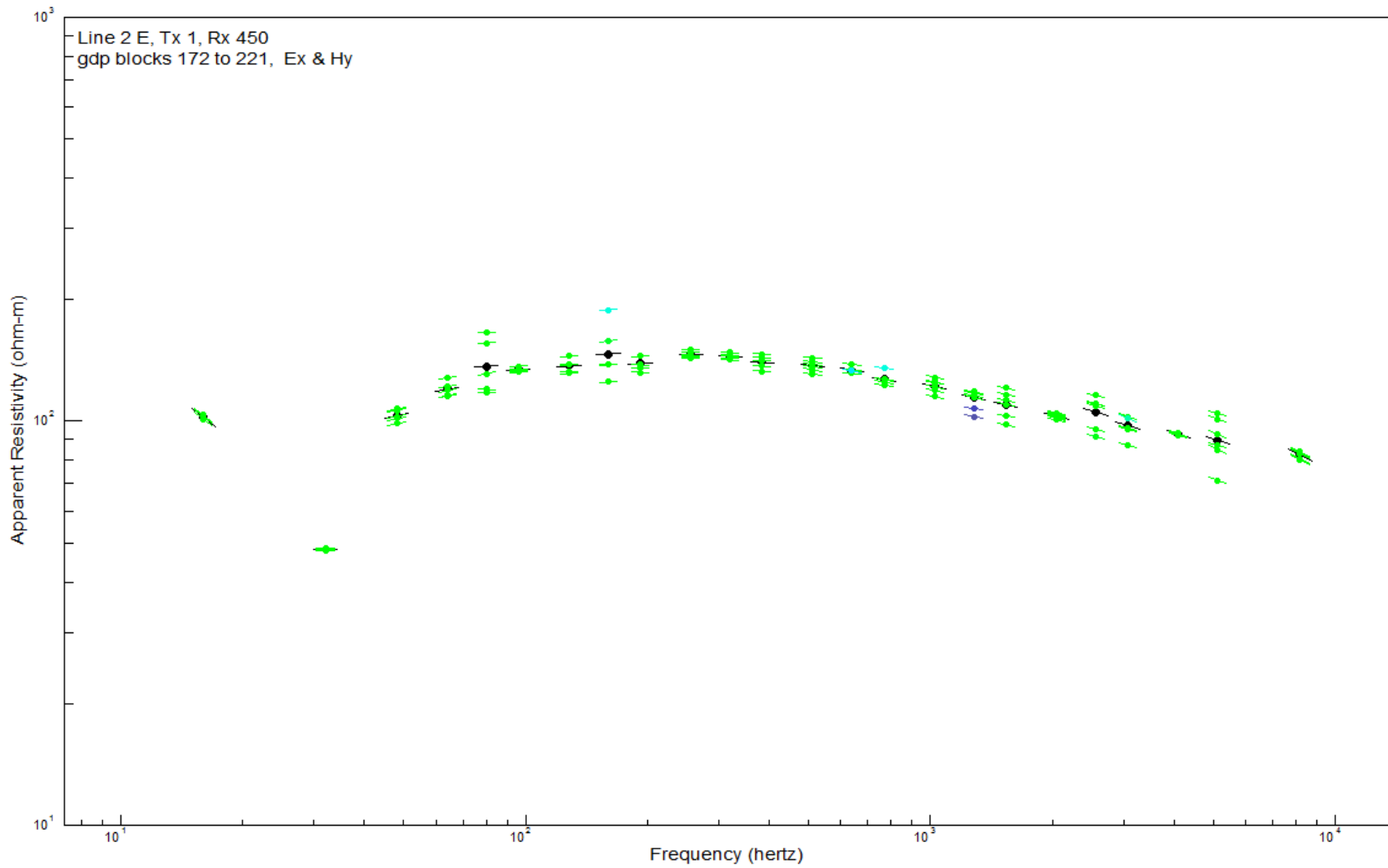
Appendix 4.15 : Line 2 raw sounding data, observing up to the 5th harmonic. Dipole 450.
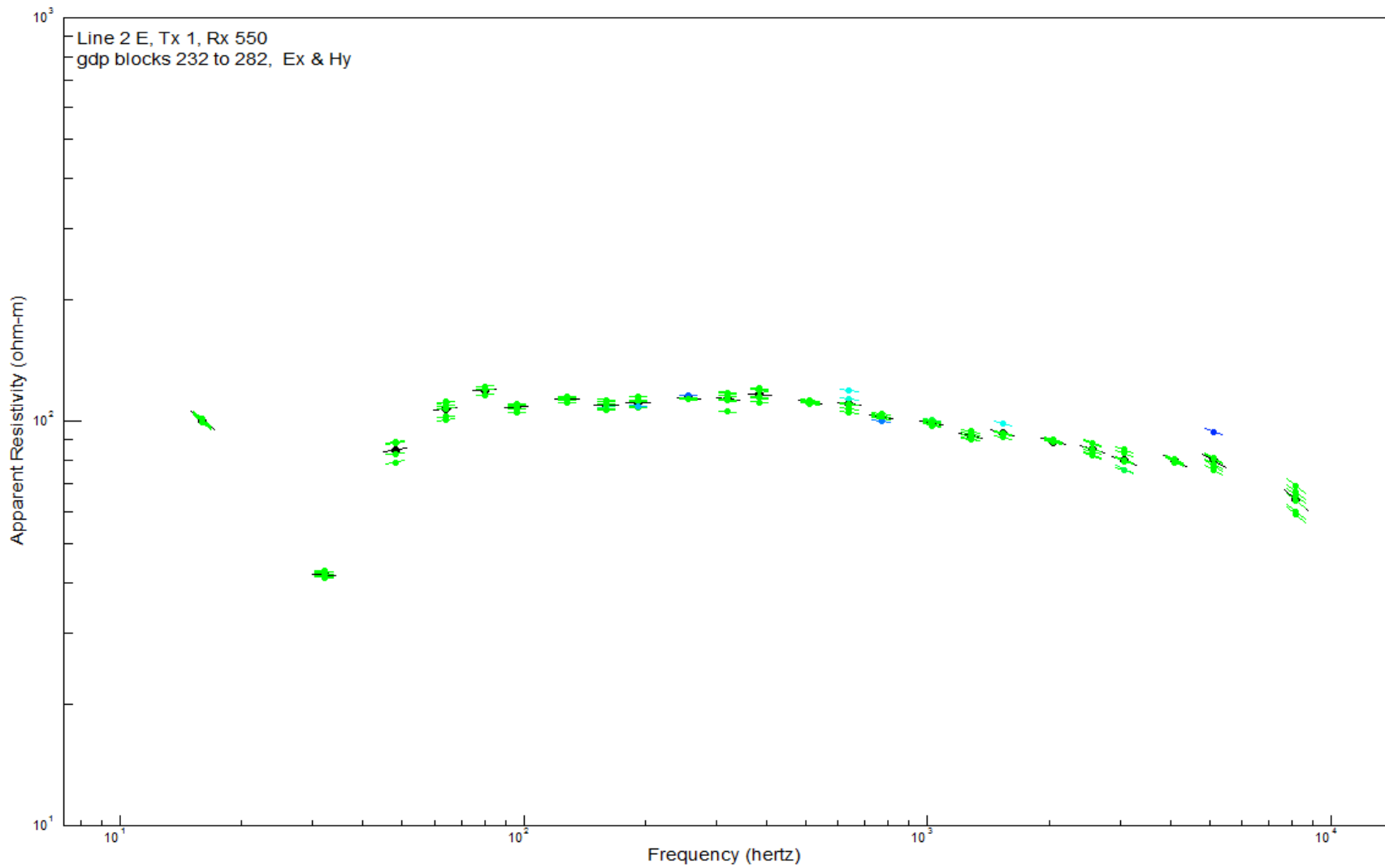
Appendix 4.16 : Line 2 raw sounding data, observing up to the 5th harmonic. Dipole 550.
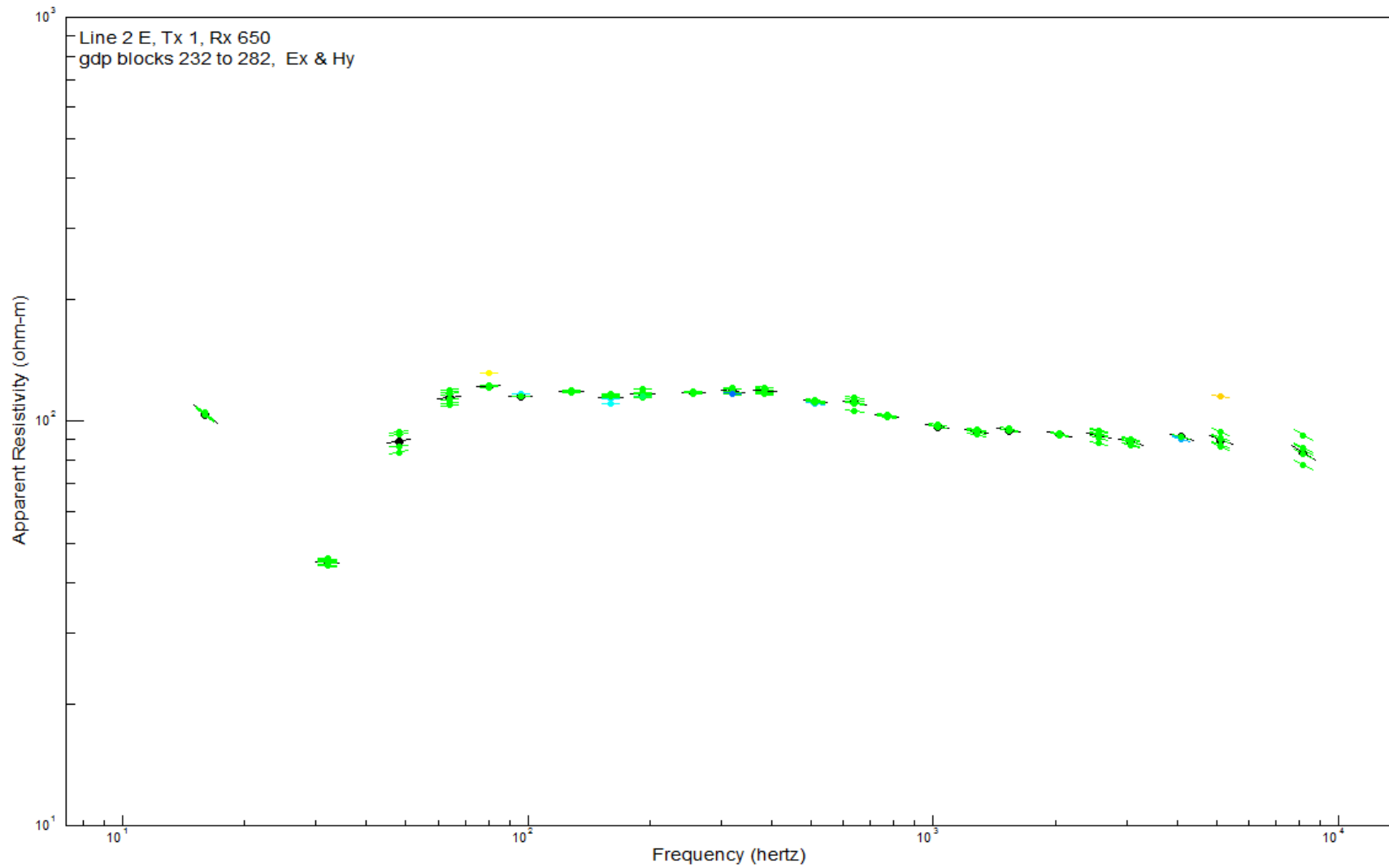
Appendix 4.17 : Line 2 raw sounding data, observing up to the 5th harmonic. Dipole 650.

Line 2 E, Tx 1, Rx 750
gdp blocks 232 to 282, Ex & Hy

Apparent Resistivity (ohm-m)

Frequency (hertz)
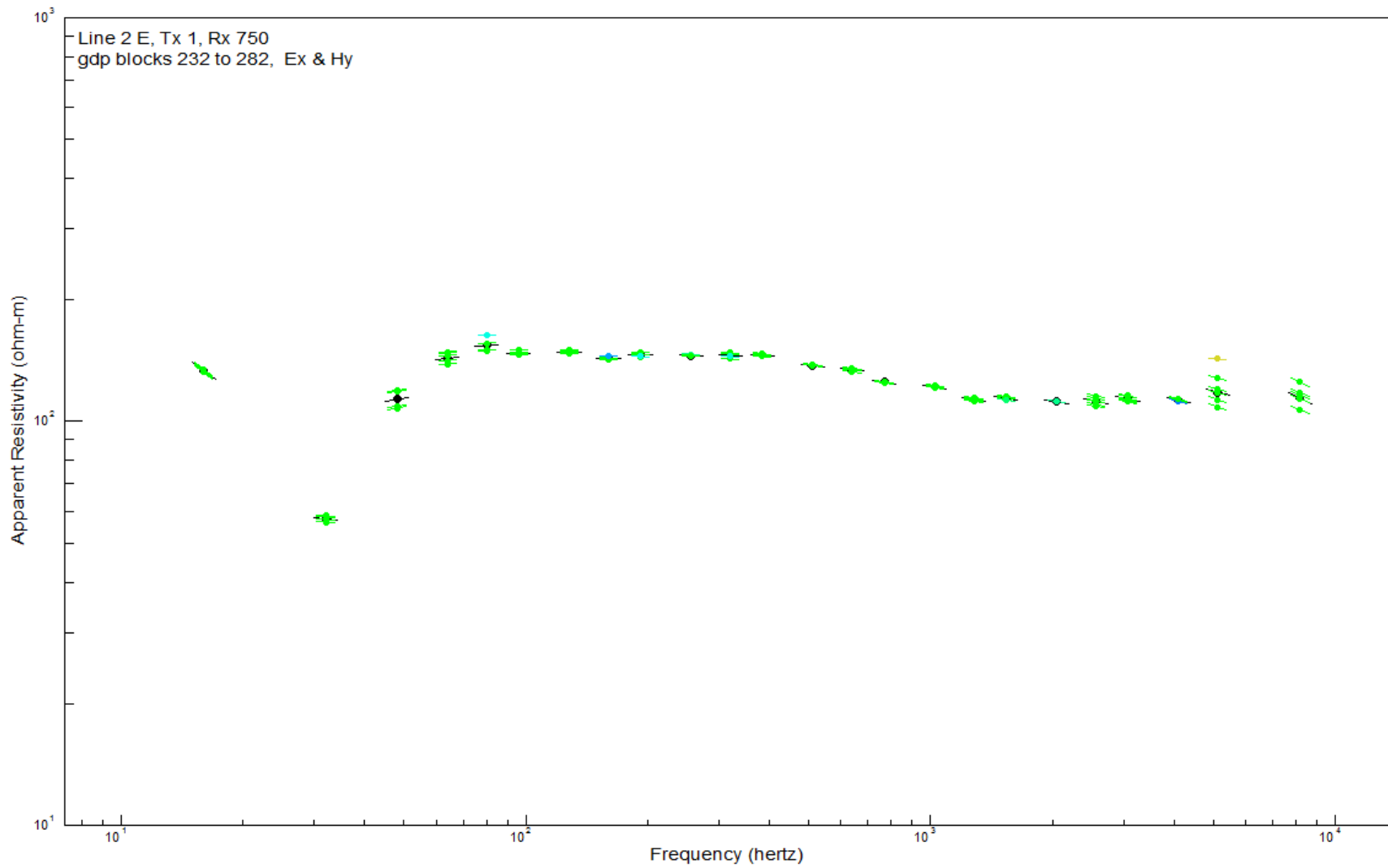
Appendix 4.18 : Line 2 raw sounding data, observing up to the 5th harmonic. Dipole 750.
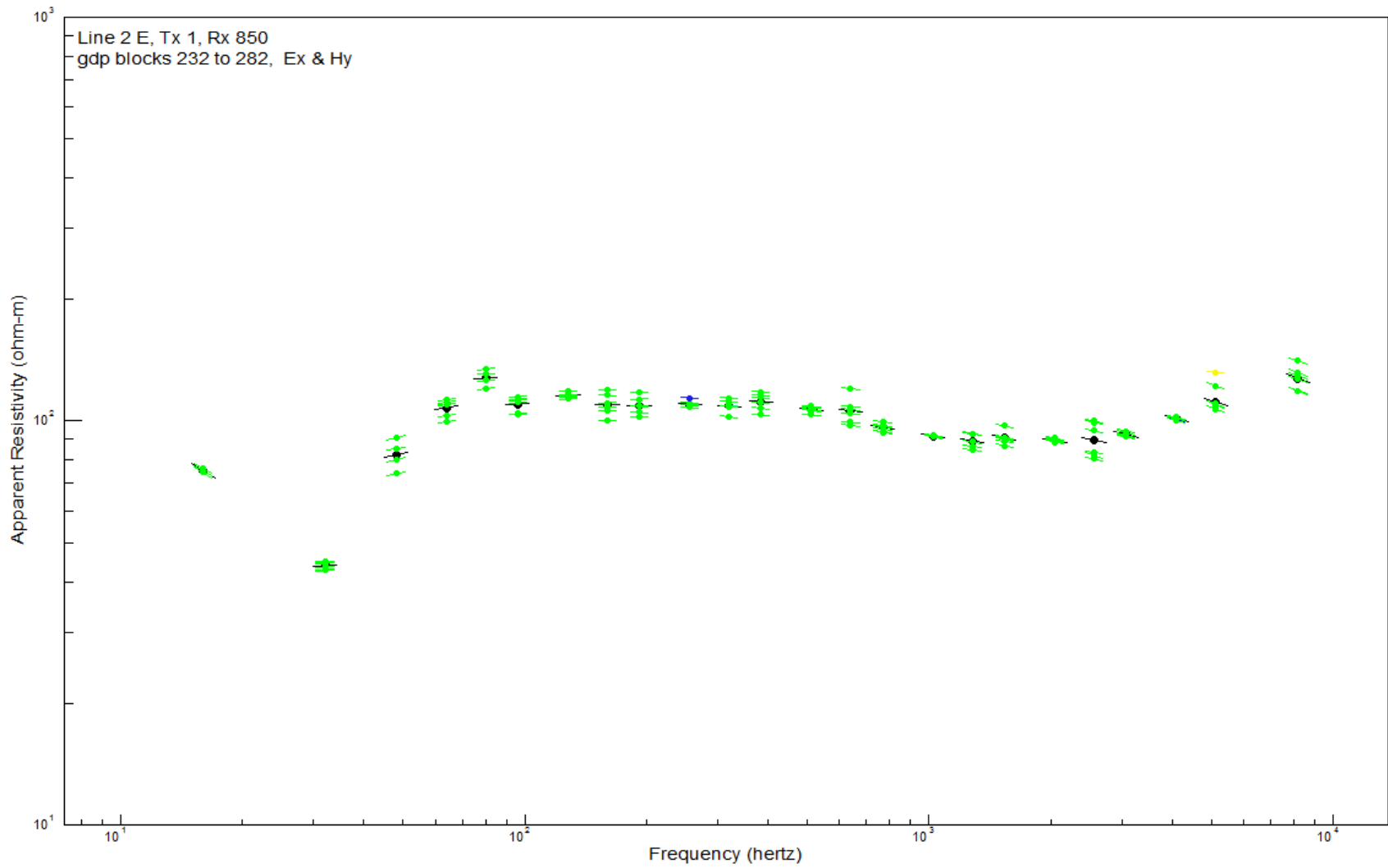
Appendix 4.19 : Line 2 raw sounding data, observing up to the 5th harmonic. Dipole 850.
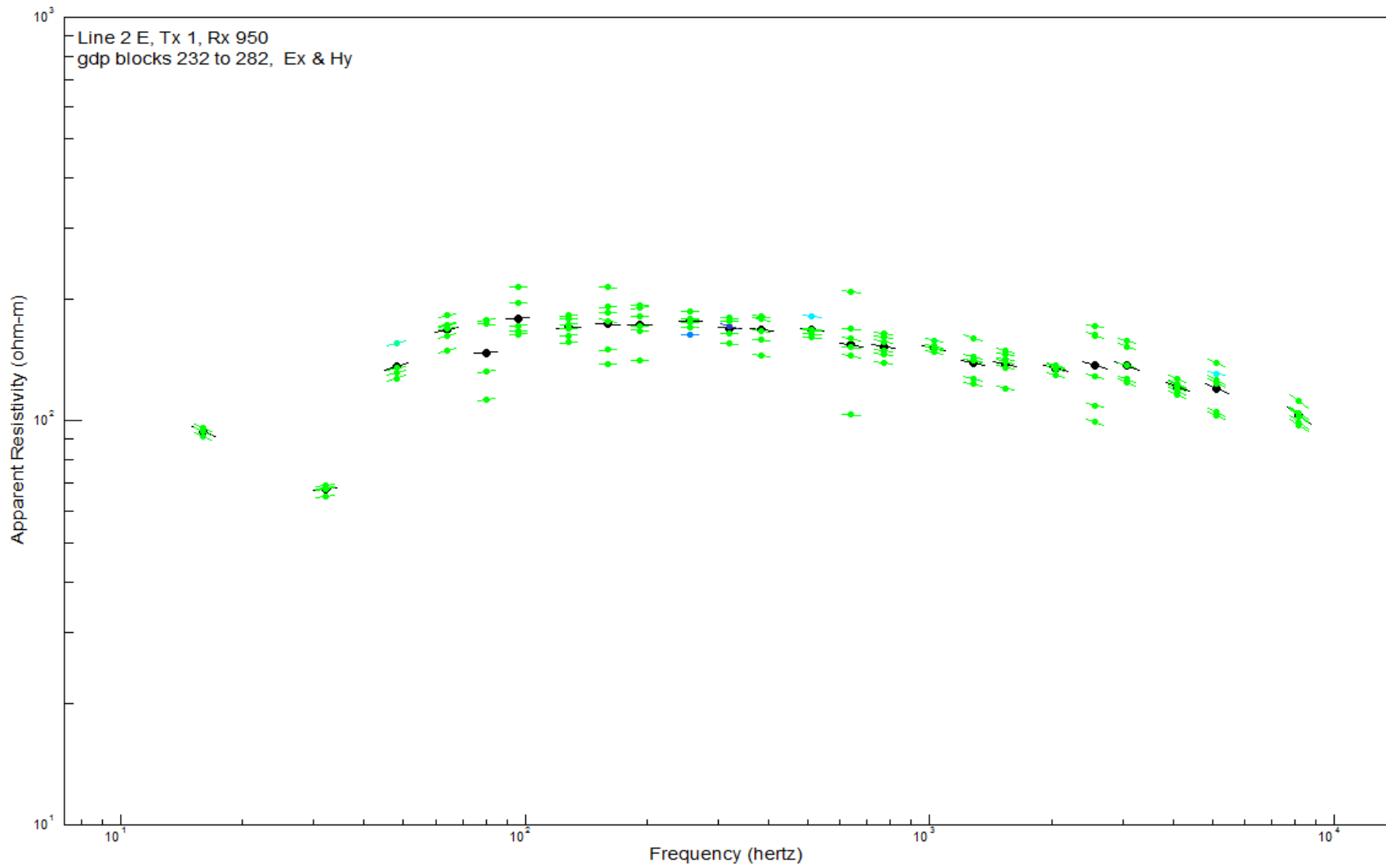
Appendix 4.20 : Line 2 raw sounding data, observing up to the 5th harmonic. Dipole 950.
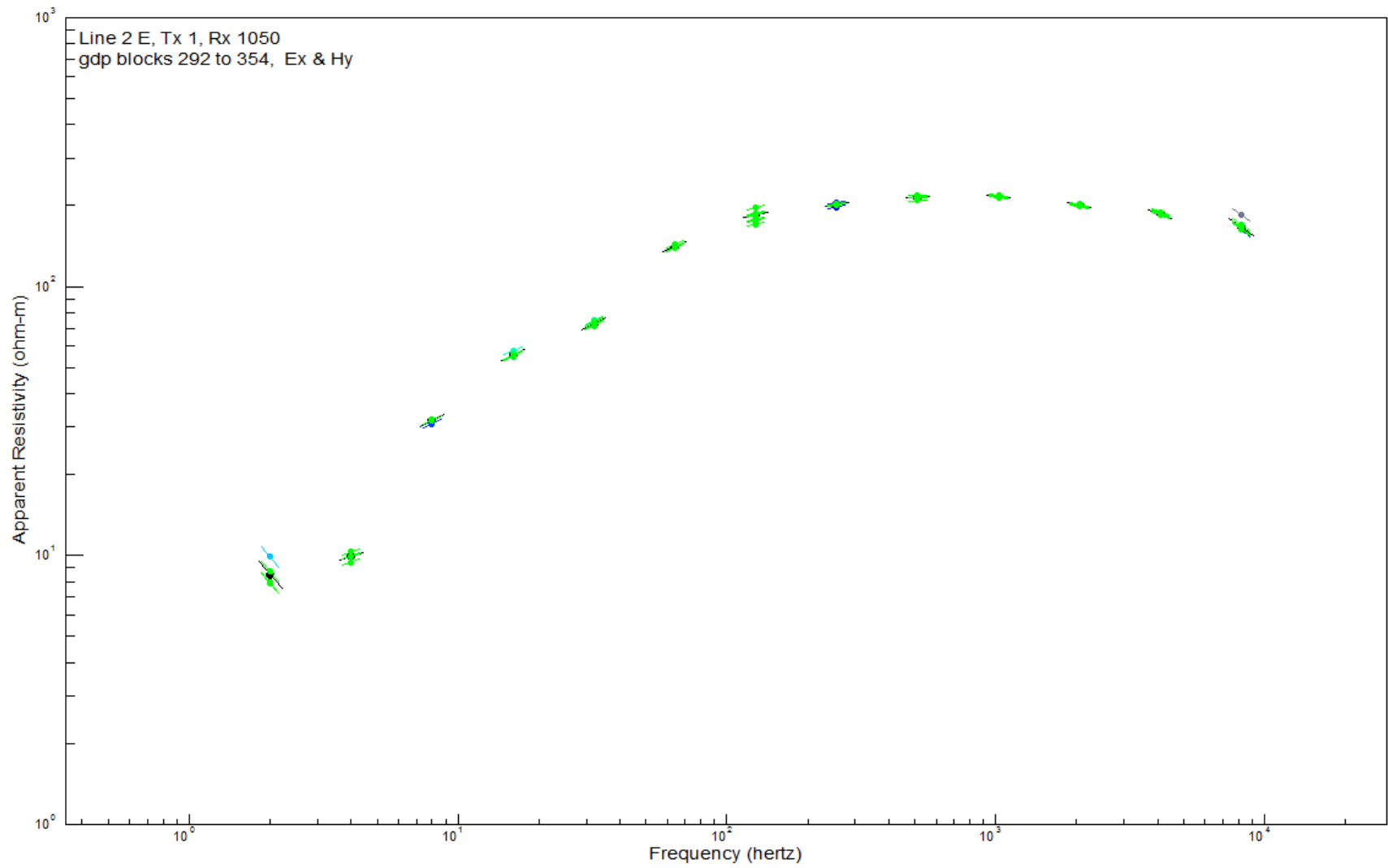
Appendix 4.21 : Line 2 raw sounding data, observing up to the 5th harmonic. Dipole 1050.
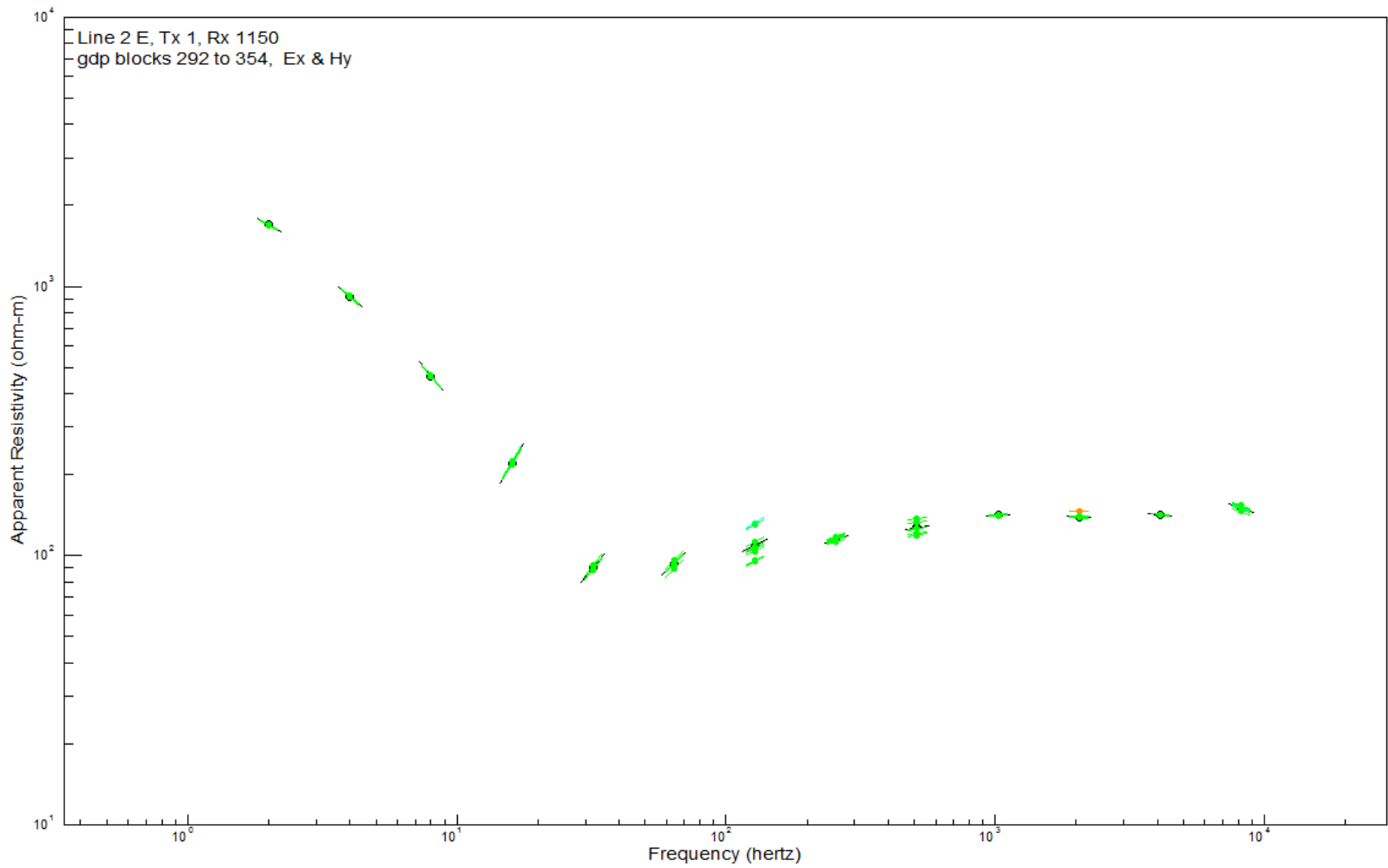
Appendix 4.22 : Line 2 raw sounding data, observing up to the 5th harmonic. Dipole 1150.

Line 2 E, Tx 1, Rx 1250
gdp blocks 292 to 354, Ex & Hy
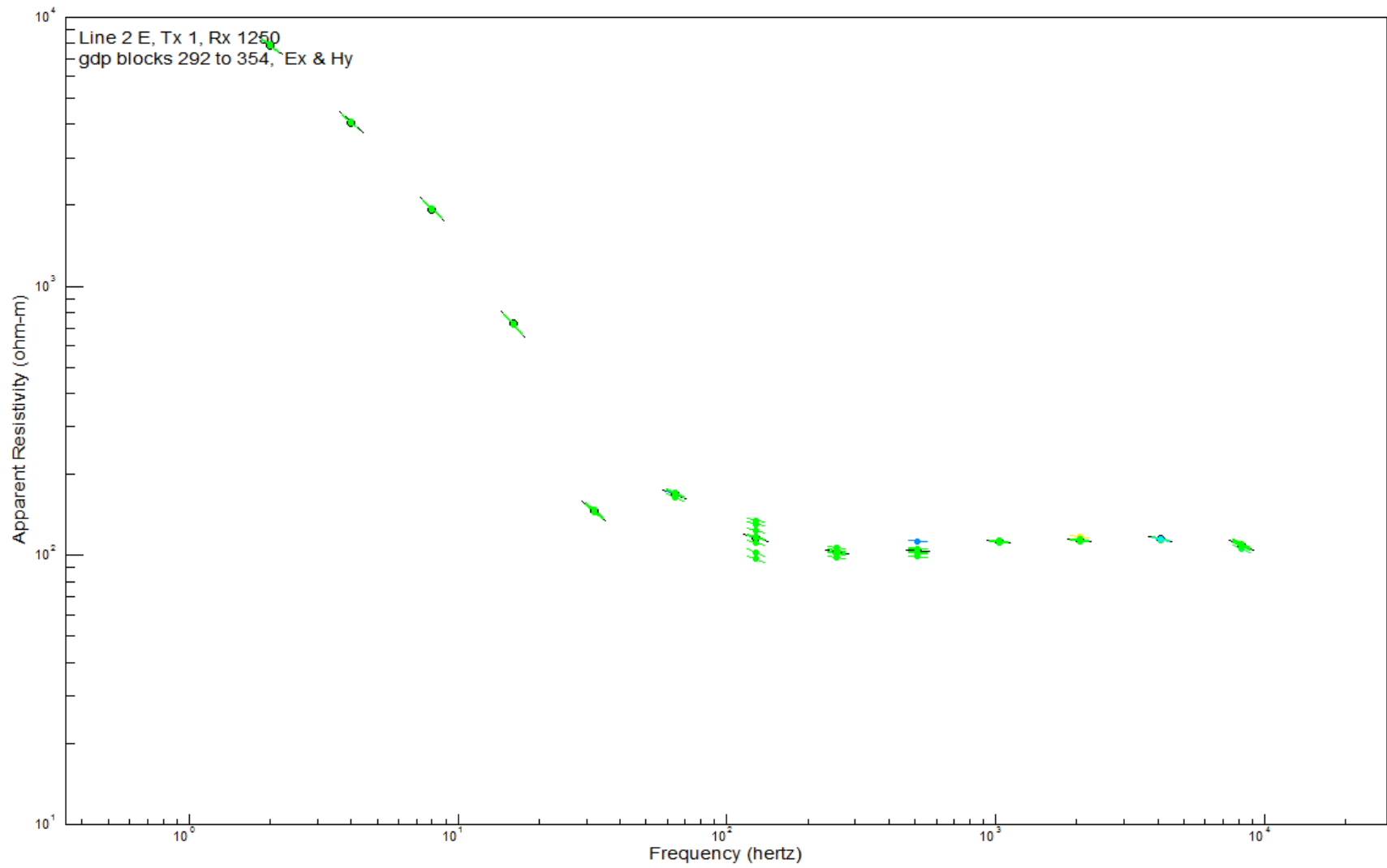
Appendix 4.23 : Line 2 raw sounding data, observing up to the 5th harmonic. Dipole 1250.
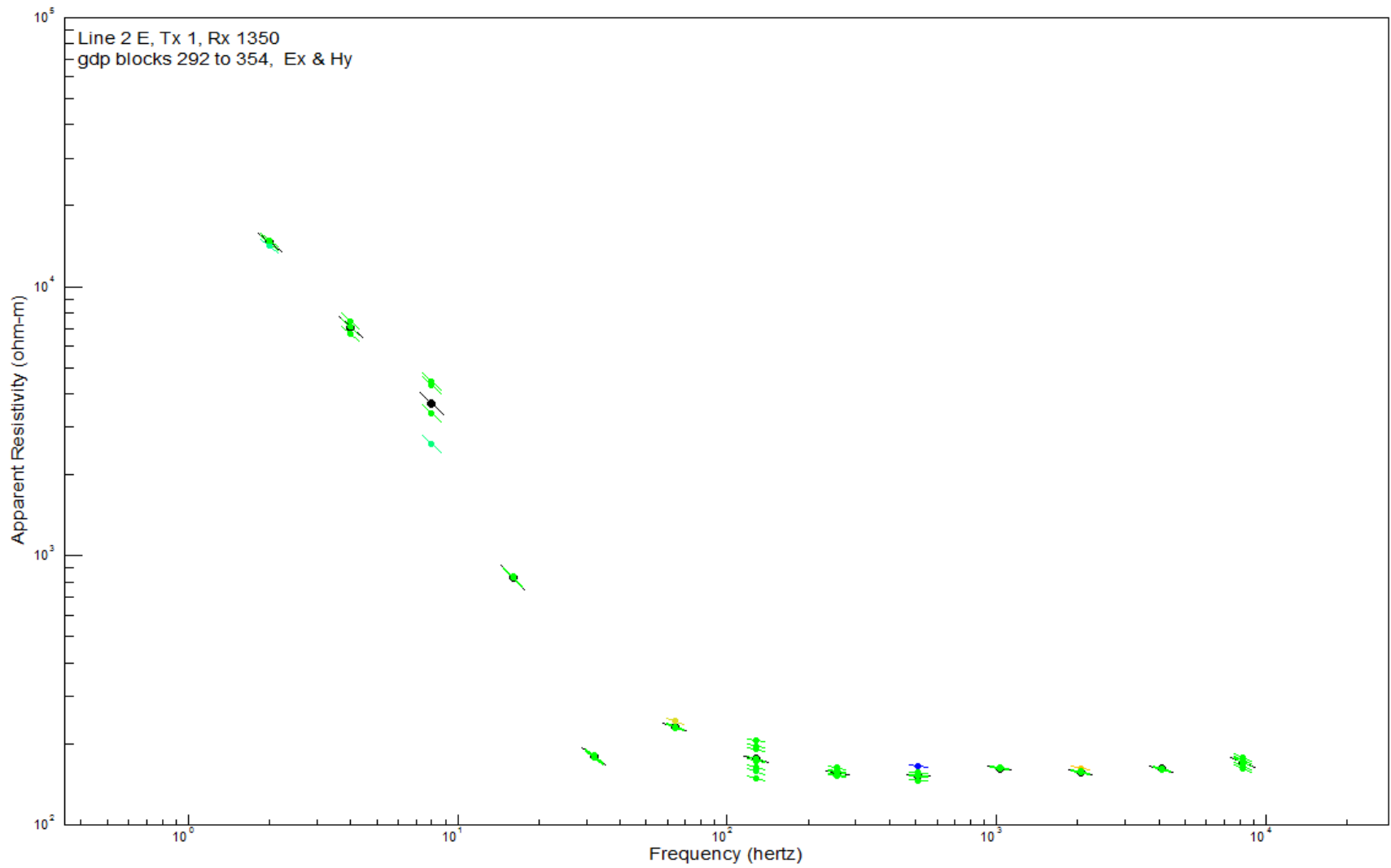
Appendix 4.24 : Line 2 raw sounding data, observing up to the 5th harmonic. Dipole 1350.

Line 2 E, Tx 1, Rx 1350
gdp blocks 292 to 354, Ex & Hy

Apparent Resistivity (ohm-m)

Frequency (hertz)

Appendix 4.25 : Line 2 raw sounding data, observing up to the 5th harmonic. Dipole 1450.

Appendix B

Figures 4.26 and 4.37 are pseudo-sections for Line 1 North and Line 2 produced by the SCS2D program based on the processed data from the CSAVGW program.

Figures 4.27 through 4.52, except for Figure 4.37, are the SCS2D program model's best-fit model responses for each dipole location through both Line 1 North and Line 2. The solid blue triangles with red strikes represent the calculated average at each frequency, as carried over from the CSAVGW program and after processing and user interpretation of the trend. The empty blue triangles connected by a blue line represent the SCS2D inversion model's best-fit dipole trend per frequency, incorporating the varied neighboring dipole trends in resistivity values. The solid red triangles are the averages carried over from the CSAVGW program processing, which the user removed from interpretation by the SCS2D model due to their heavy skewing of the model fit. The vertical dashed line marks the separation between the near-field data and far-field CSAMT data. This study is only concerned with the far-field data and we have set the lowest far-field frequency to be interpreted as 64 Hz.
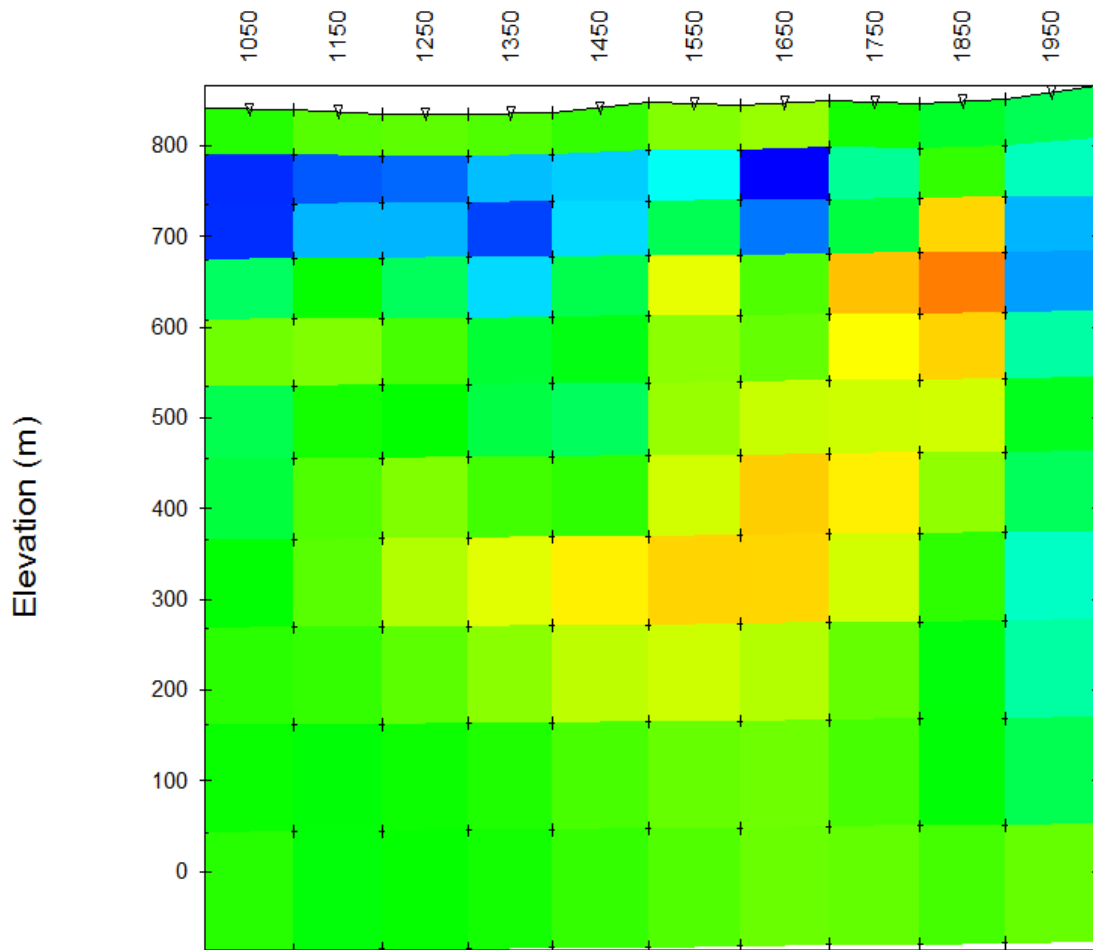
Appendix 4.26 : Inversion model from averaged data. Line 1 North pseudo cross-section.

Appendix 4.27 : Inversion model from averaged data. Line 1 North, Dipole 1050 best-fit model.

Line 1, Station 1150
Blue=TM-mode, residual = 6.95

Apparent Resistivity (ohm-m)

Frequency (hertz)
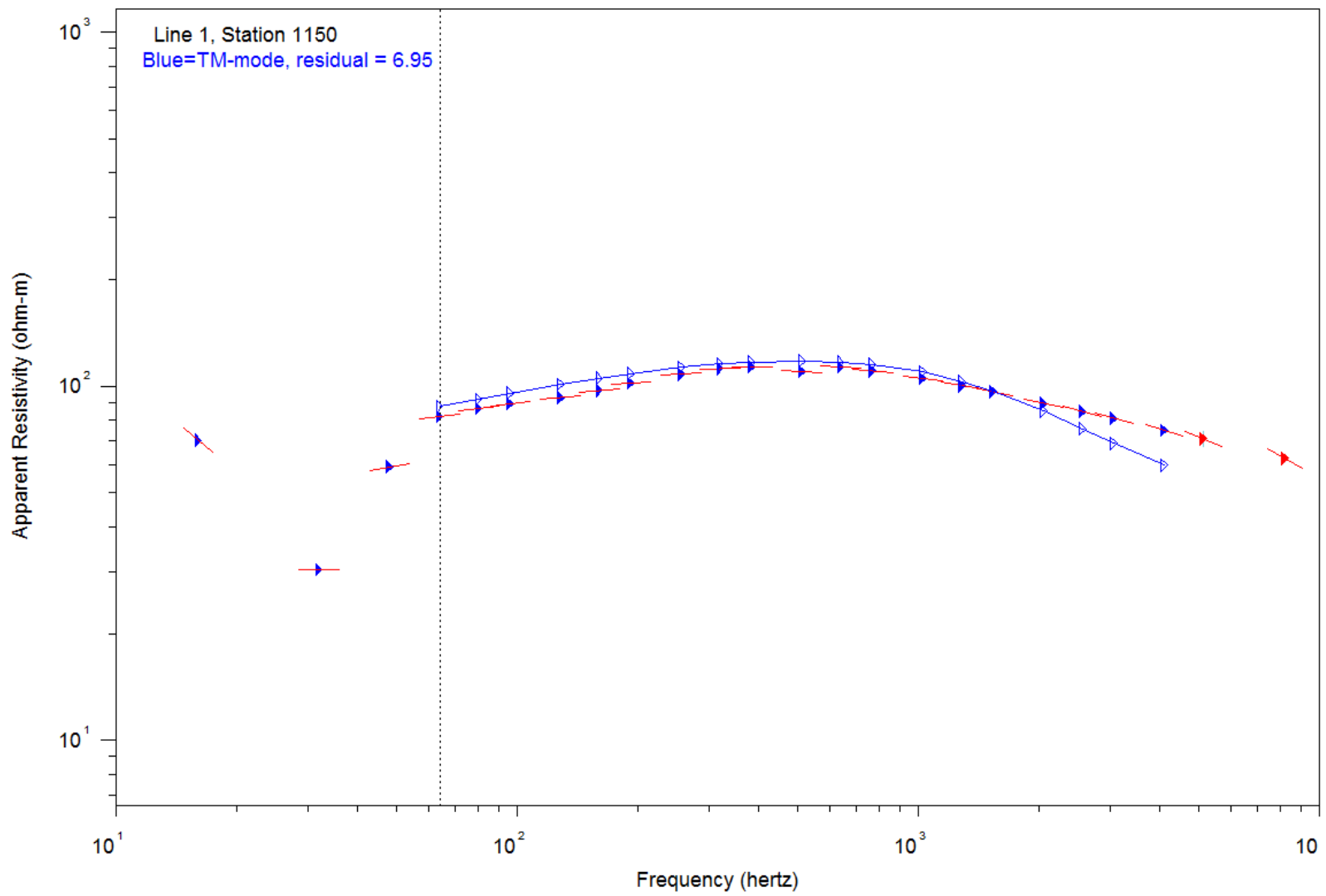
Appendix 4.28 : Inversion model from averaged data. Line 1 North, Dipole 1150 best-fit model.
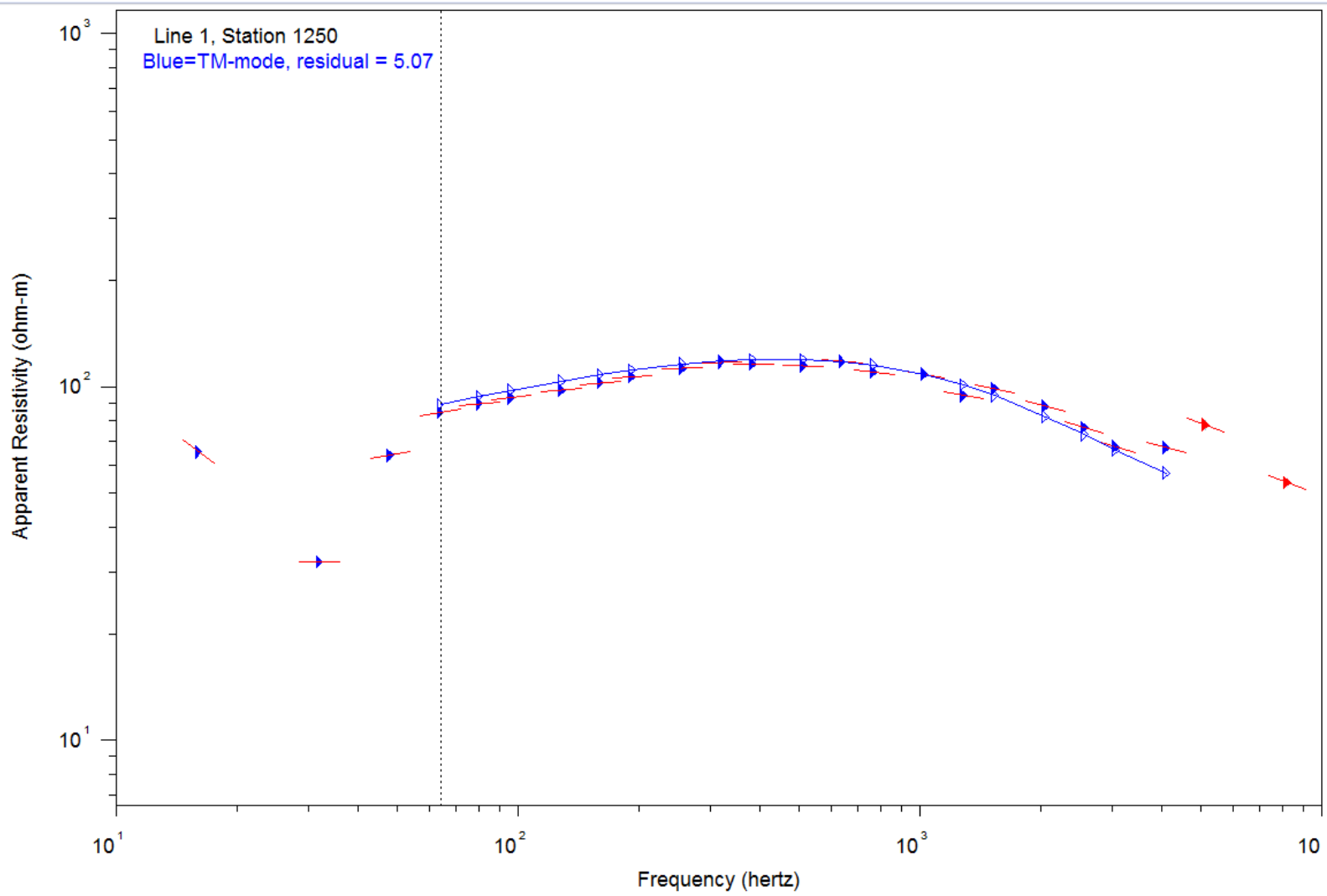
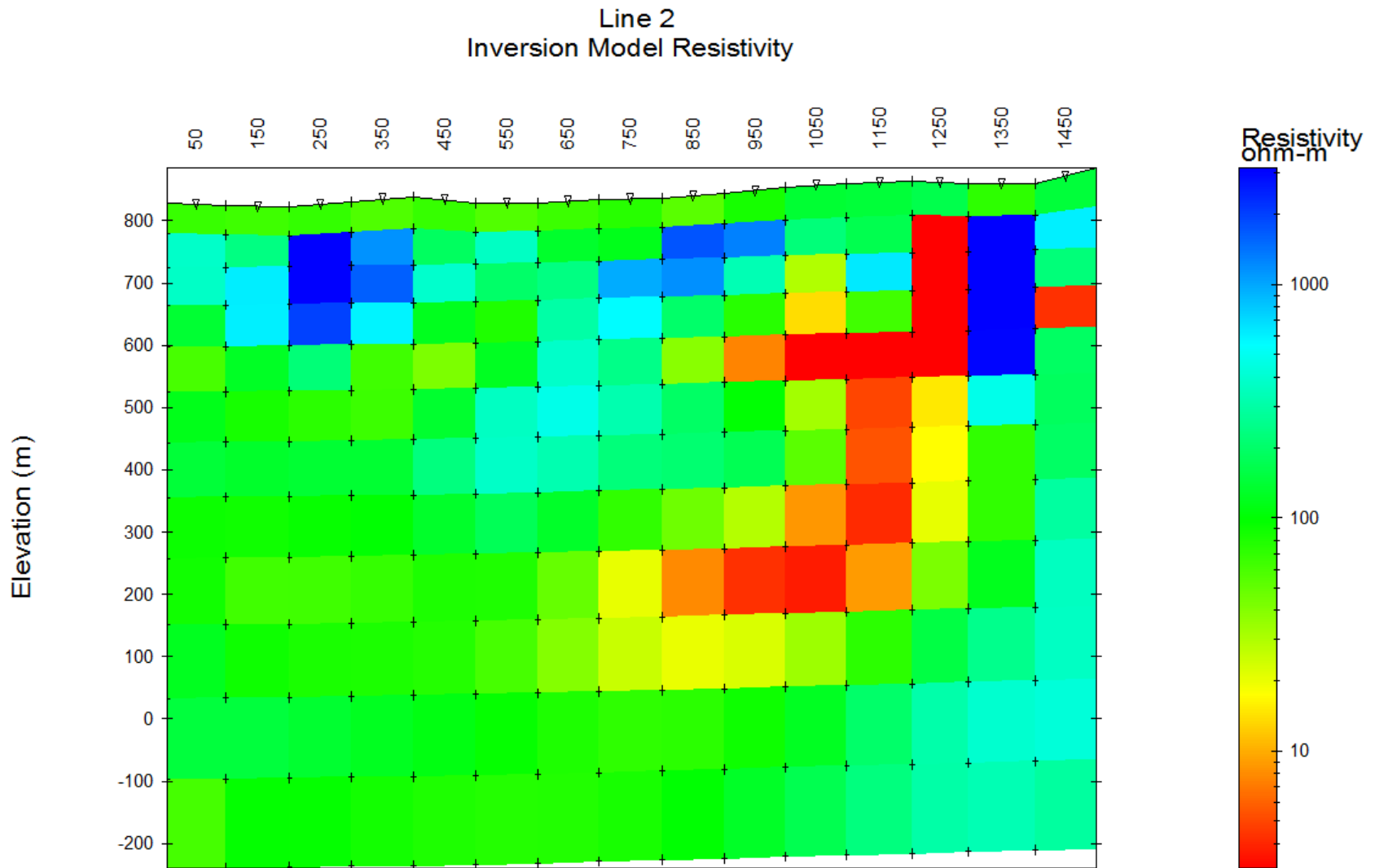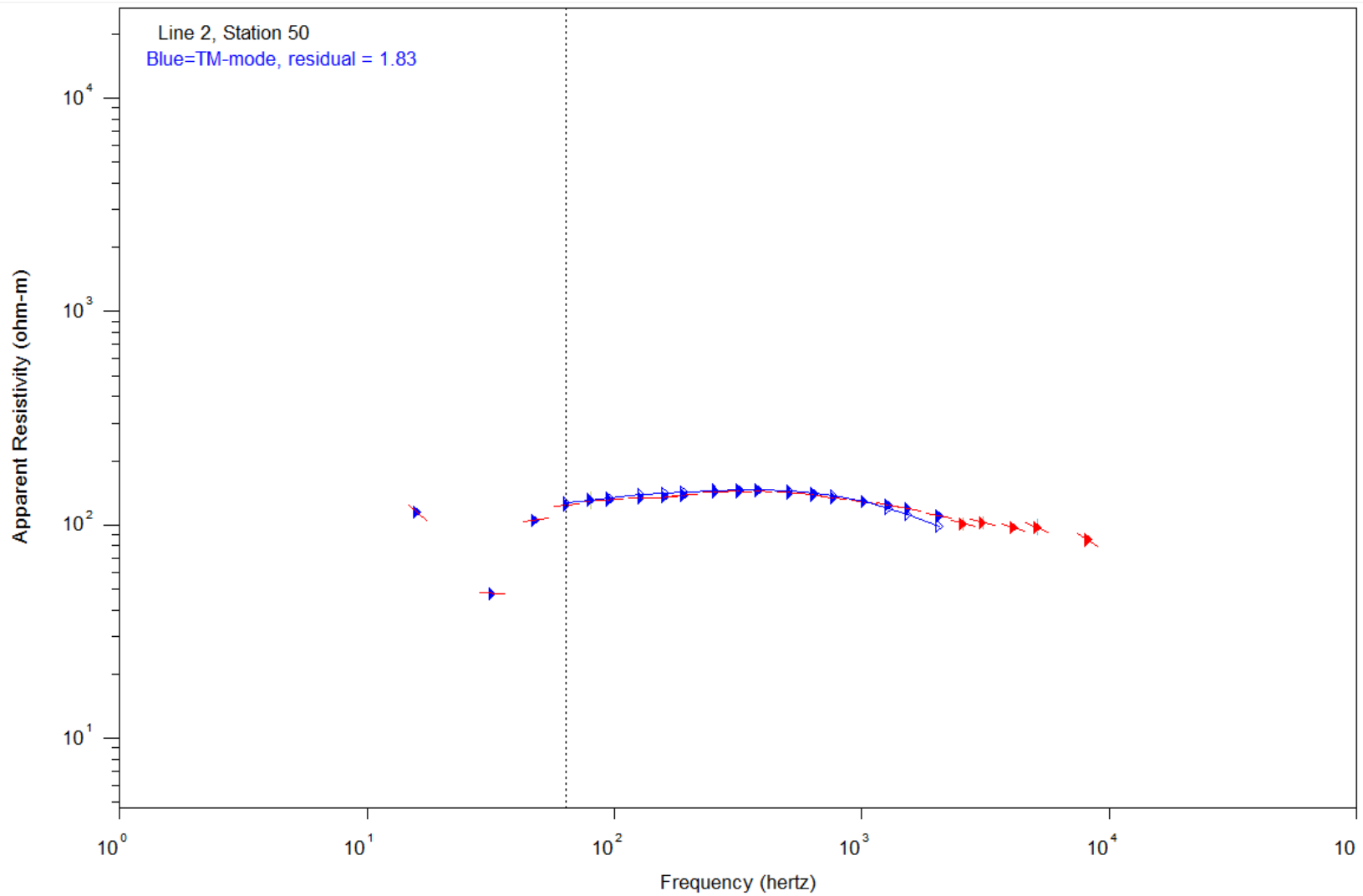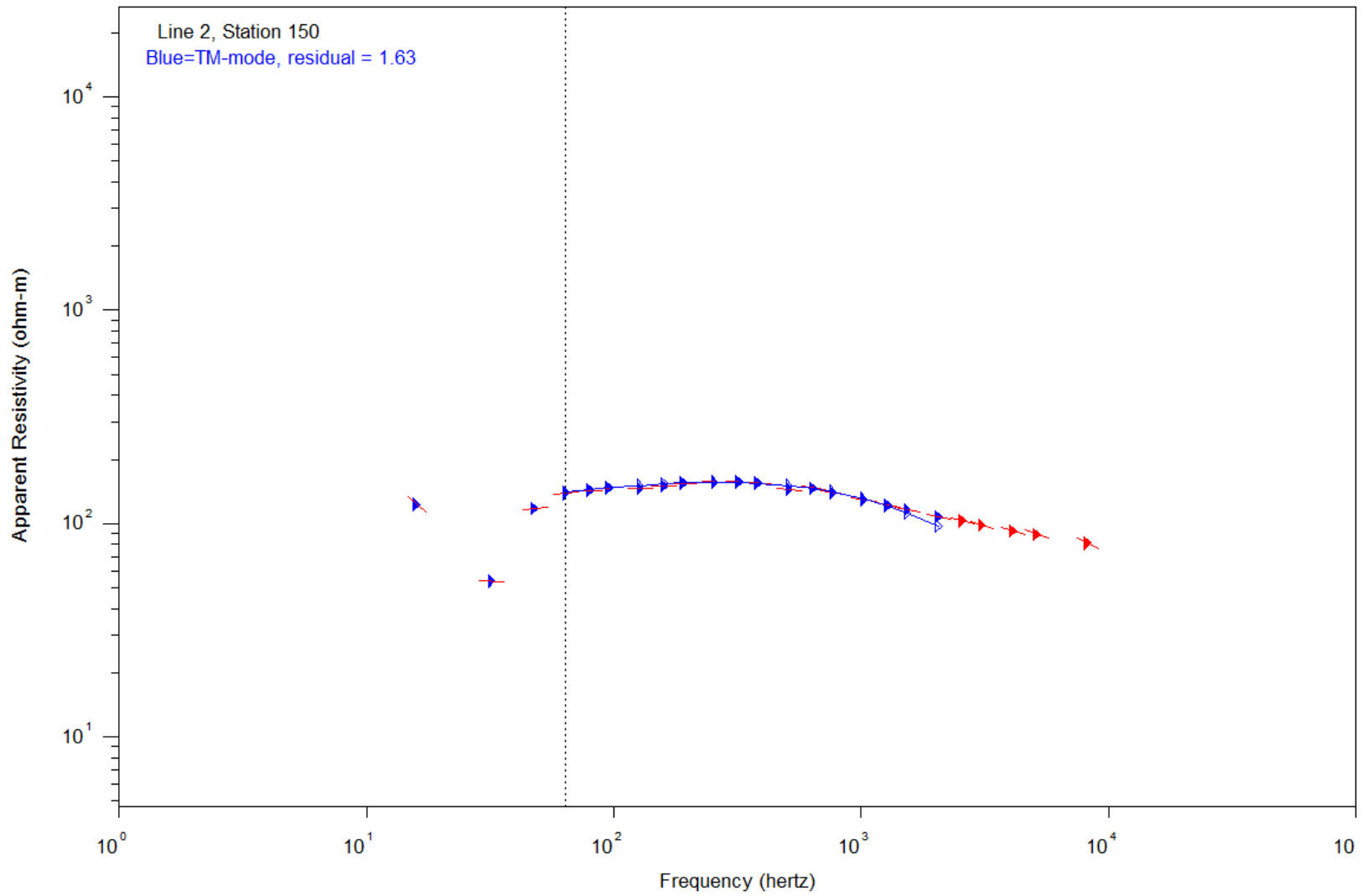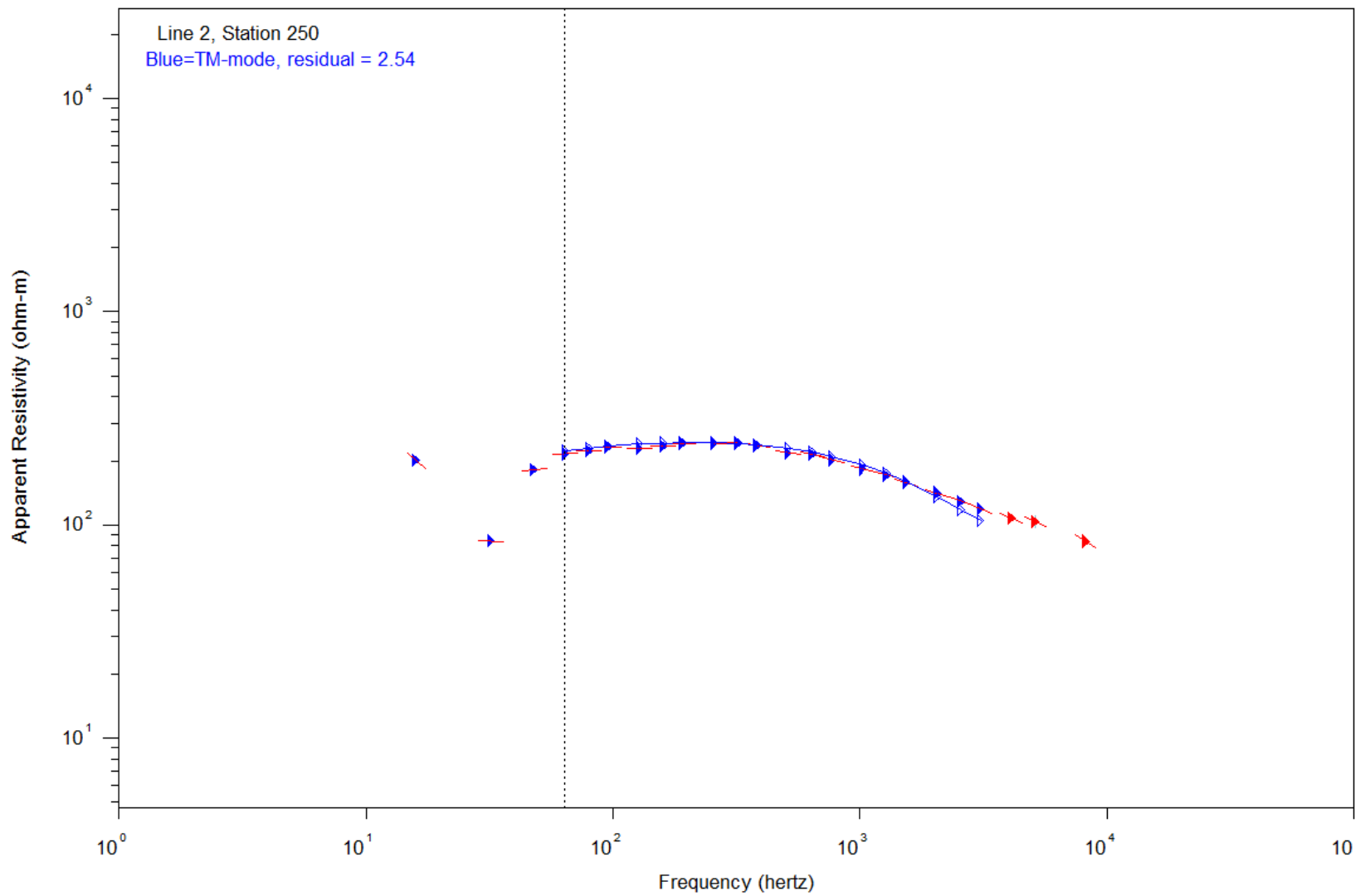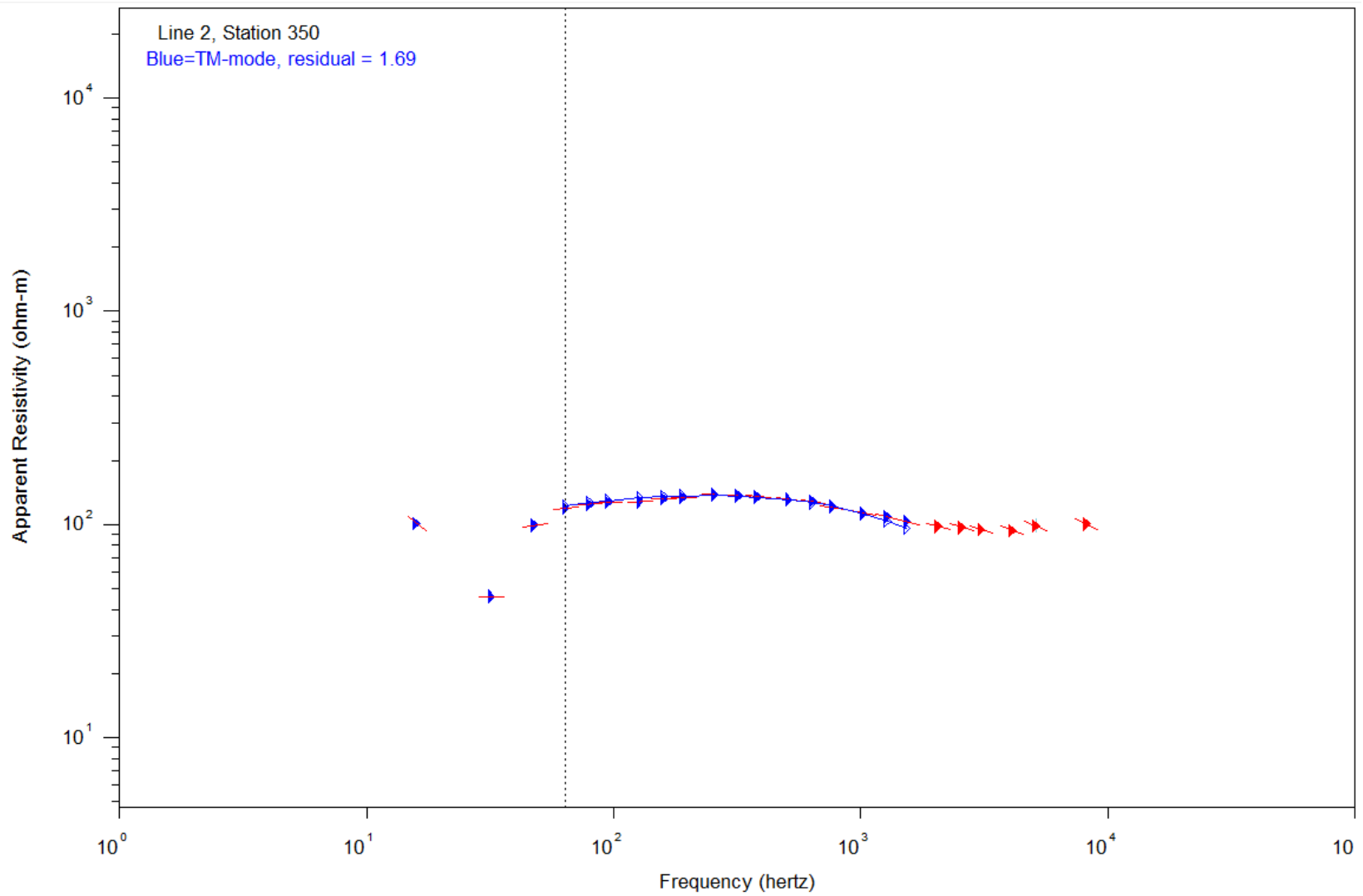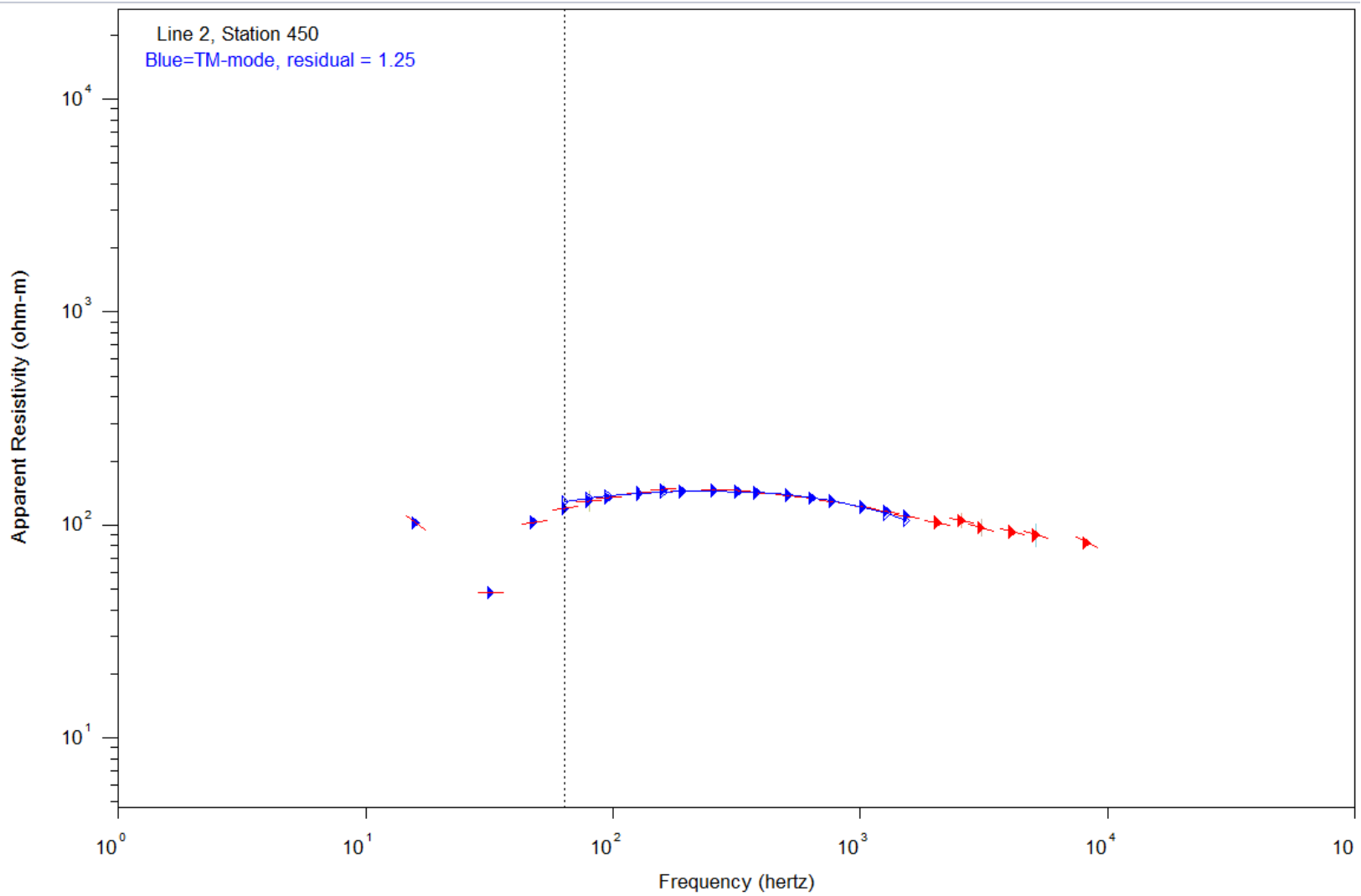Appendix 4.29 : Inversion model from averaged data. Line 1 North, Dipole 1250 best-fit model.
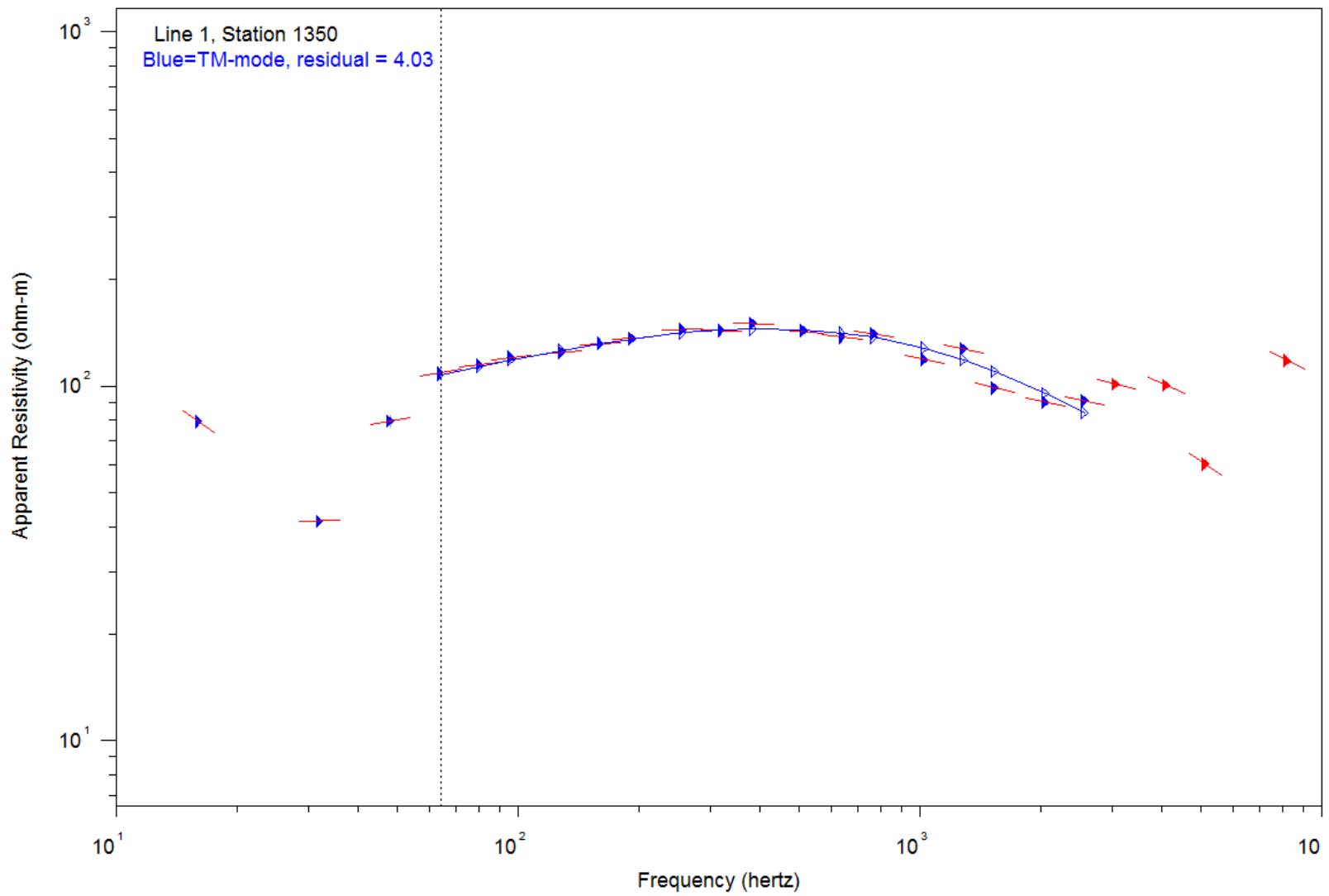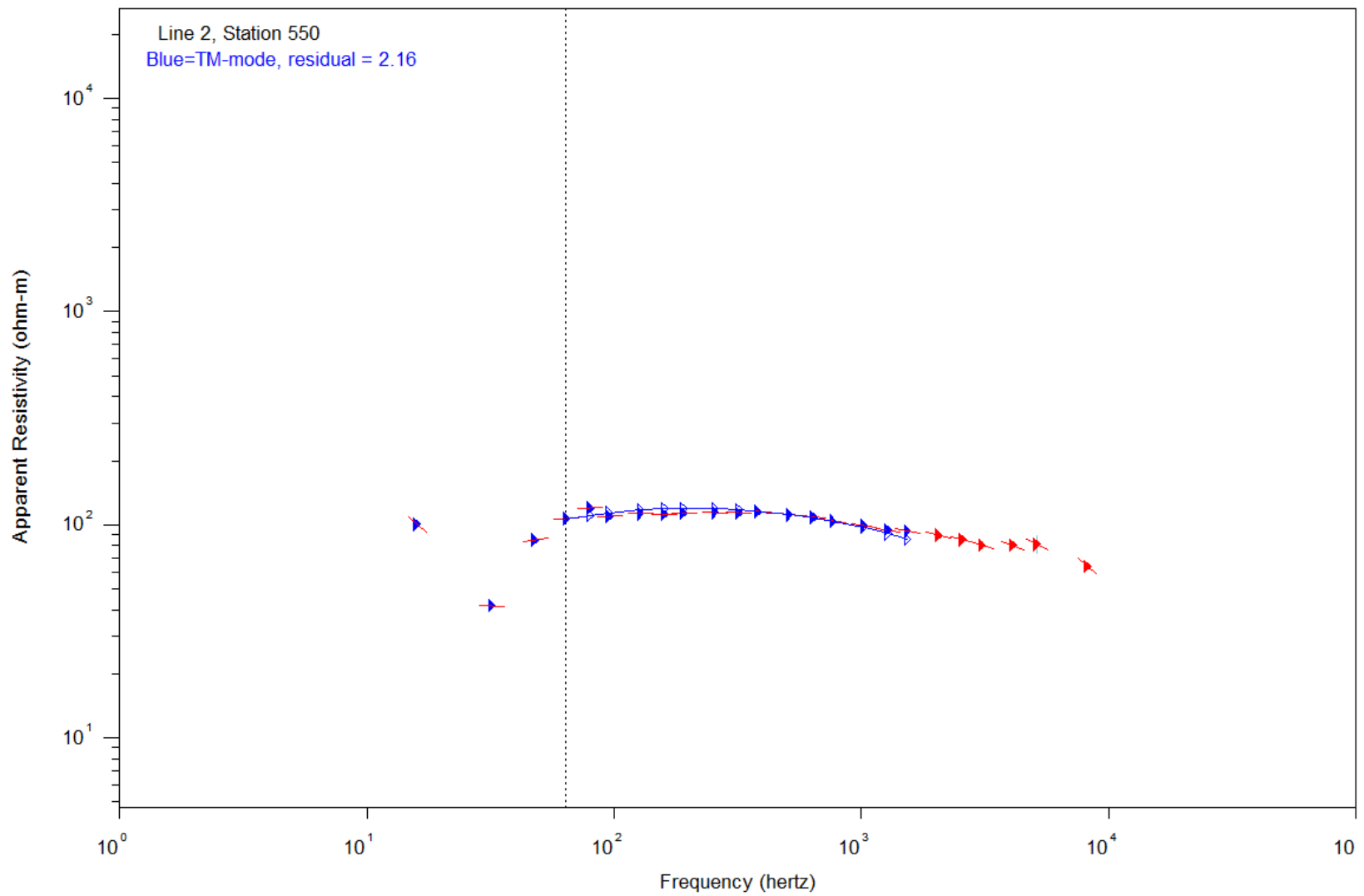
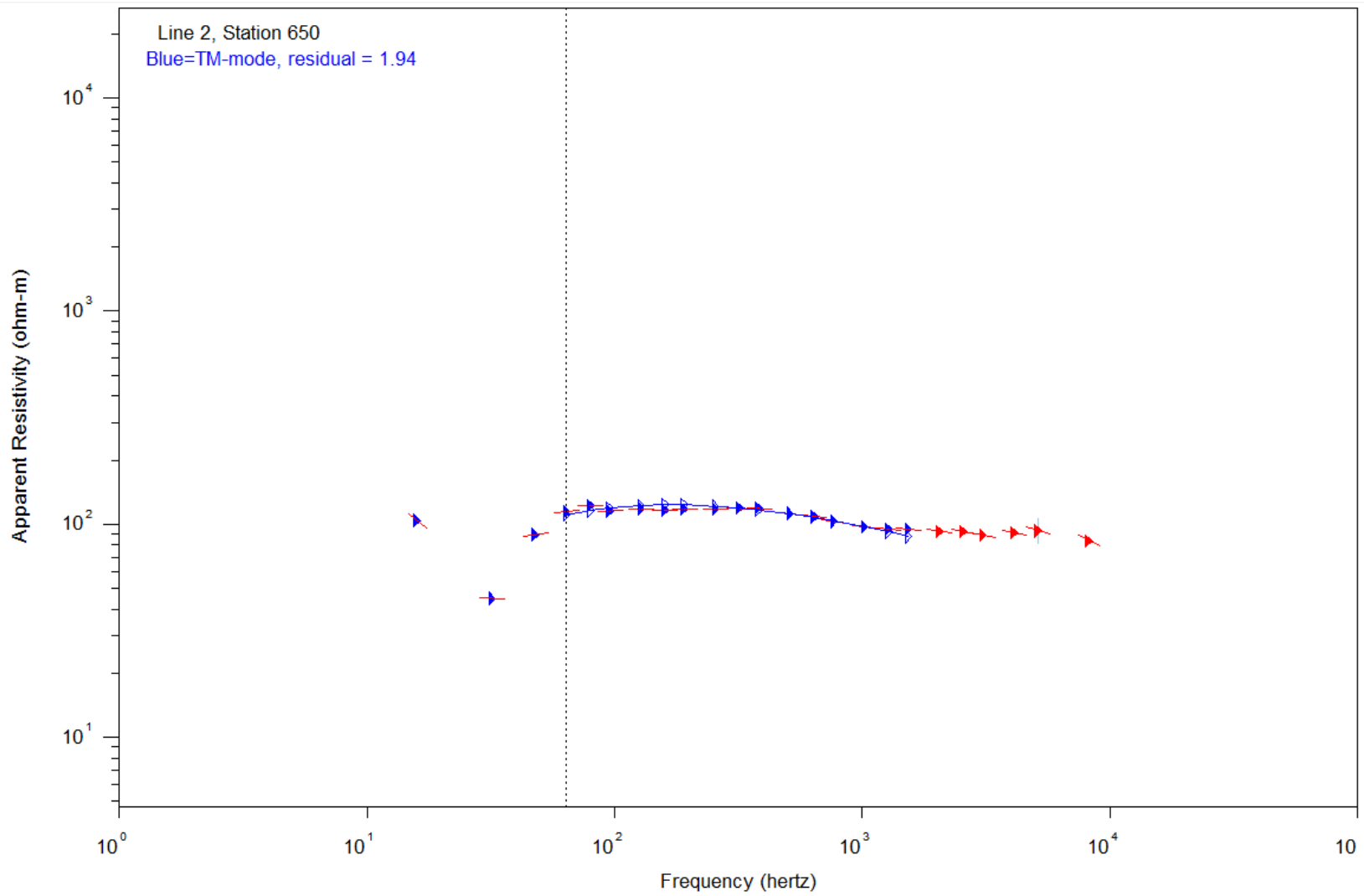Appendix 4.30 : Inversion model from averaged data. Line 1 North, Dipole 1350 best-fit model.
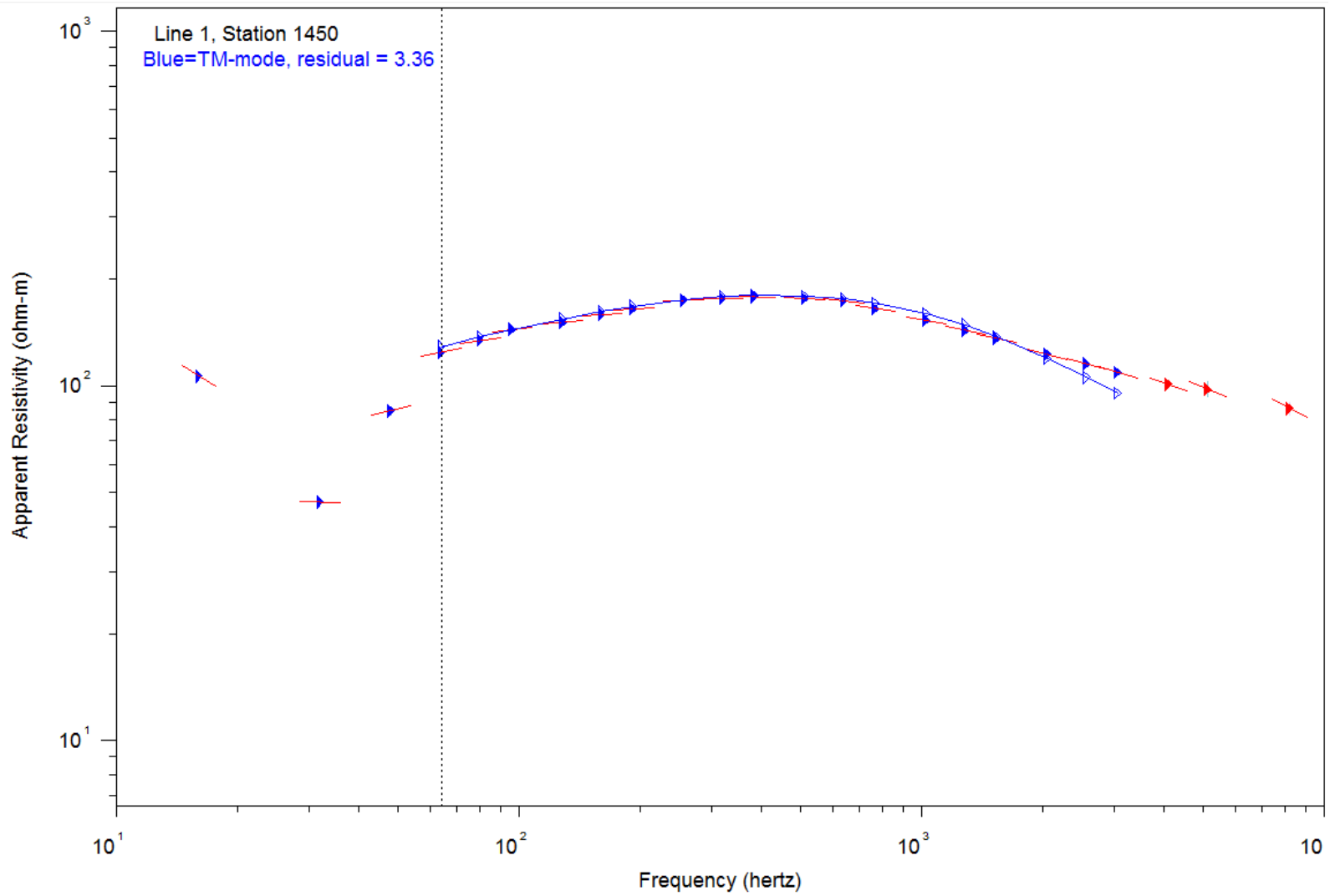
Appendix 4.31 : Inversion model from averaged data. Line 1 North, Dipole 1450 best-fit model.
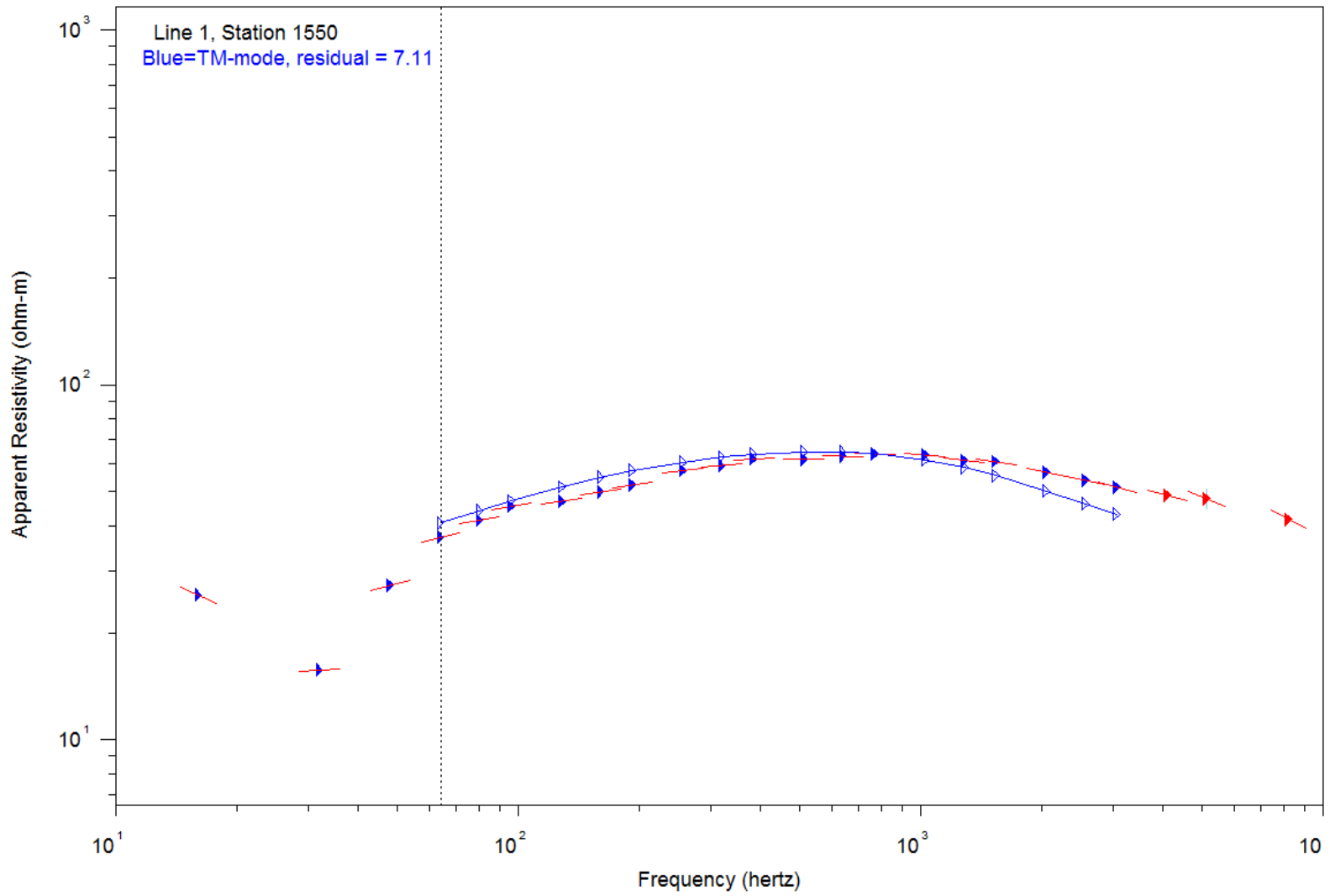
Appendix 4.32 : Inversion model from averaged data. Line 1 North, Dipole 1550 best-fit model.
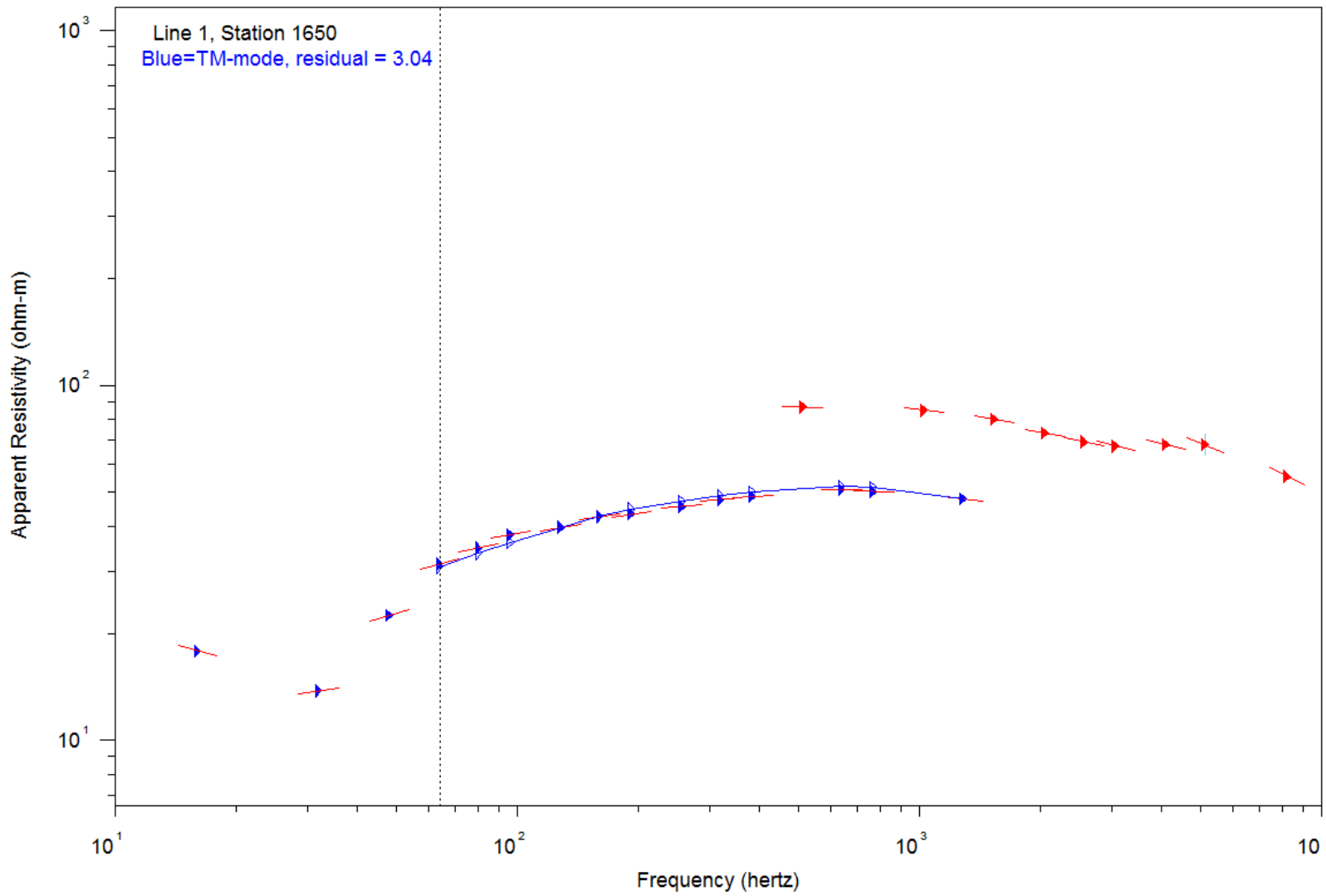
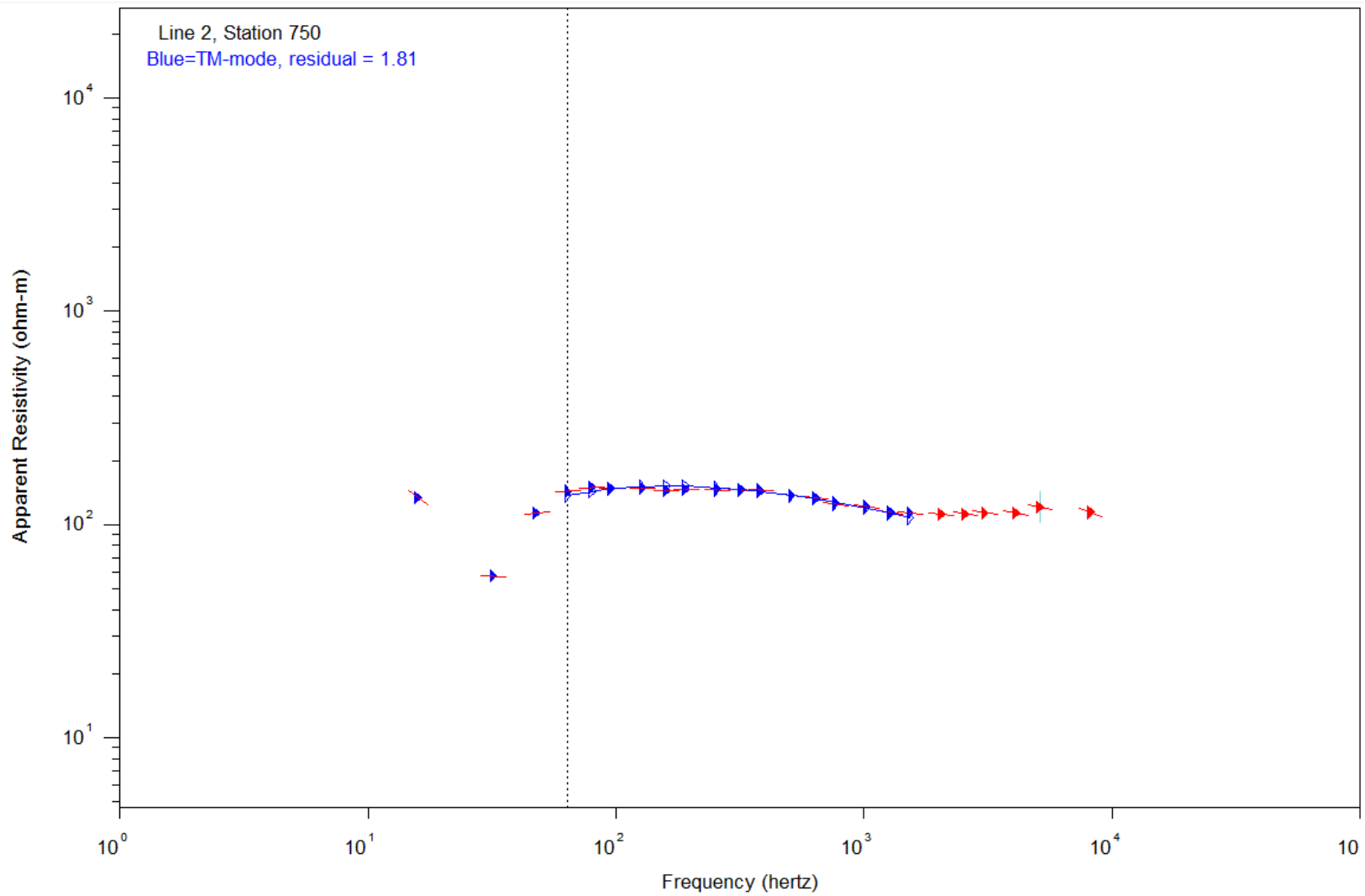Appendix 4.33 : Inversion model from averaged data. Line 1 North, Dipole 1650 best-fit model.
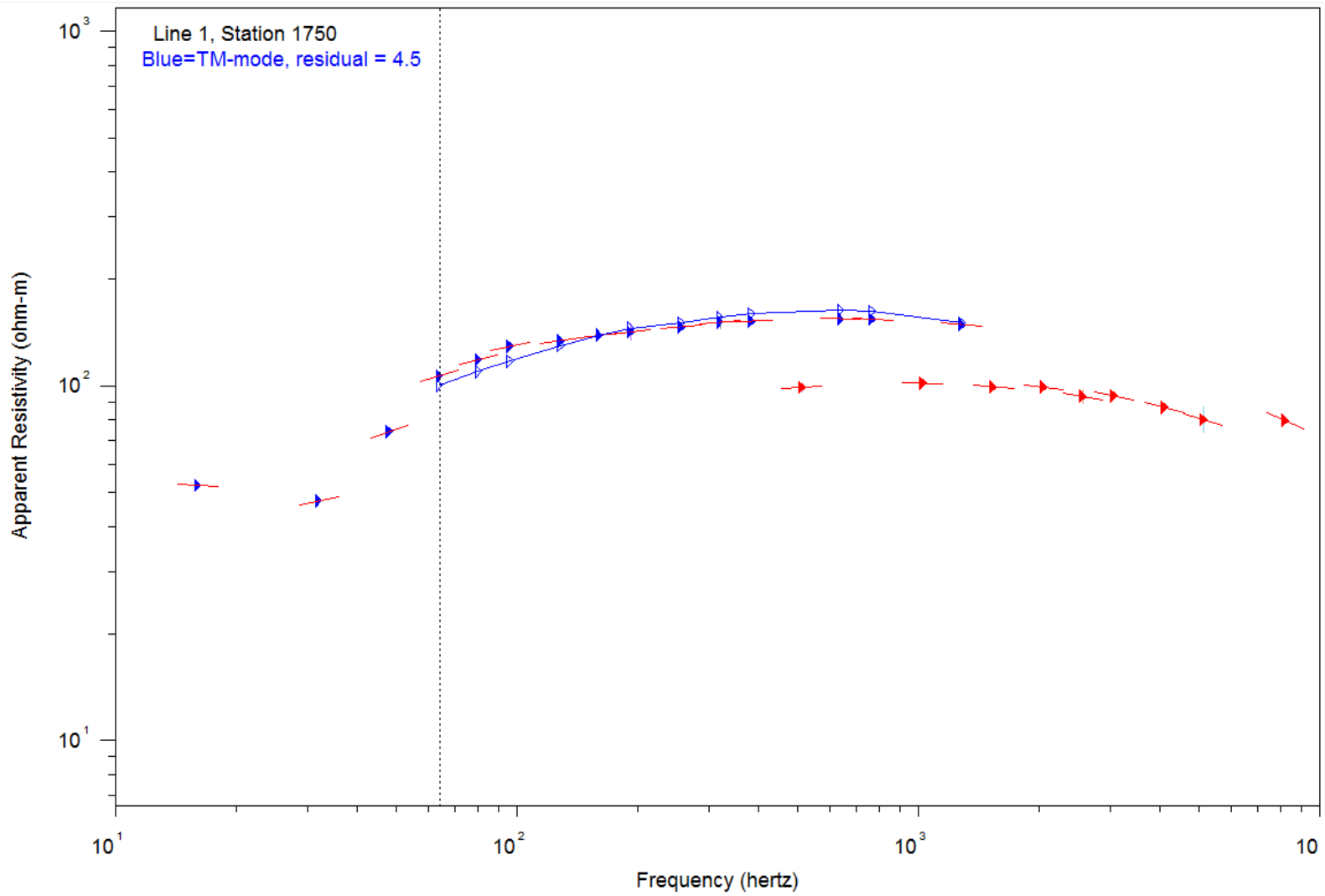
Appendix 4.34 : Inversion model from averaged data. Line 1 North, Dipole 1750 best-fit model.
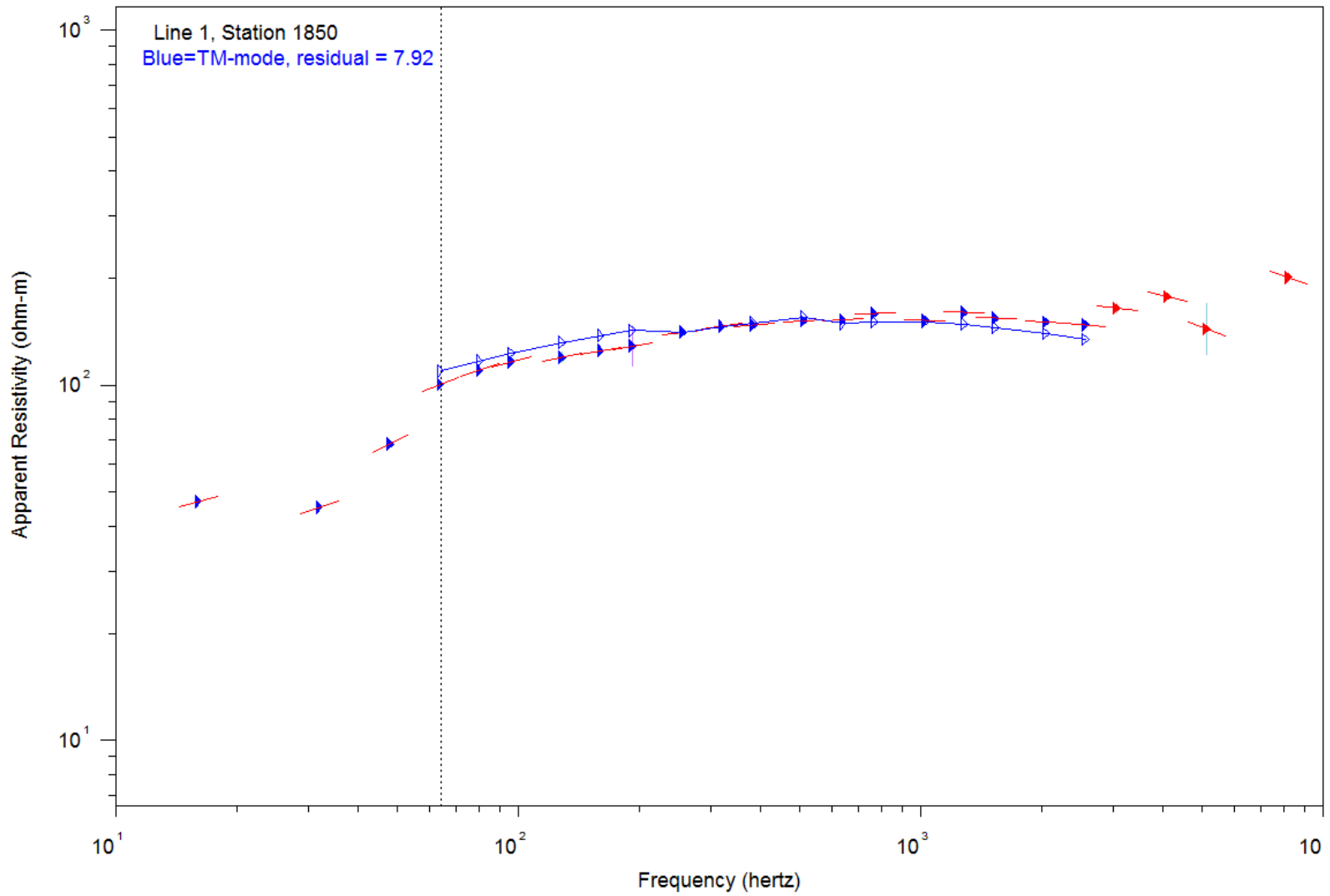
Appendix 4.35 : Inversion model from averaged data. Line 1 North, Dipole 1850 best-fit model.
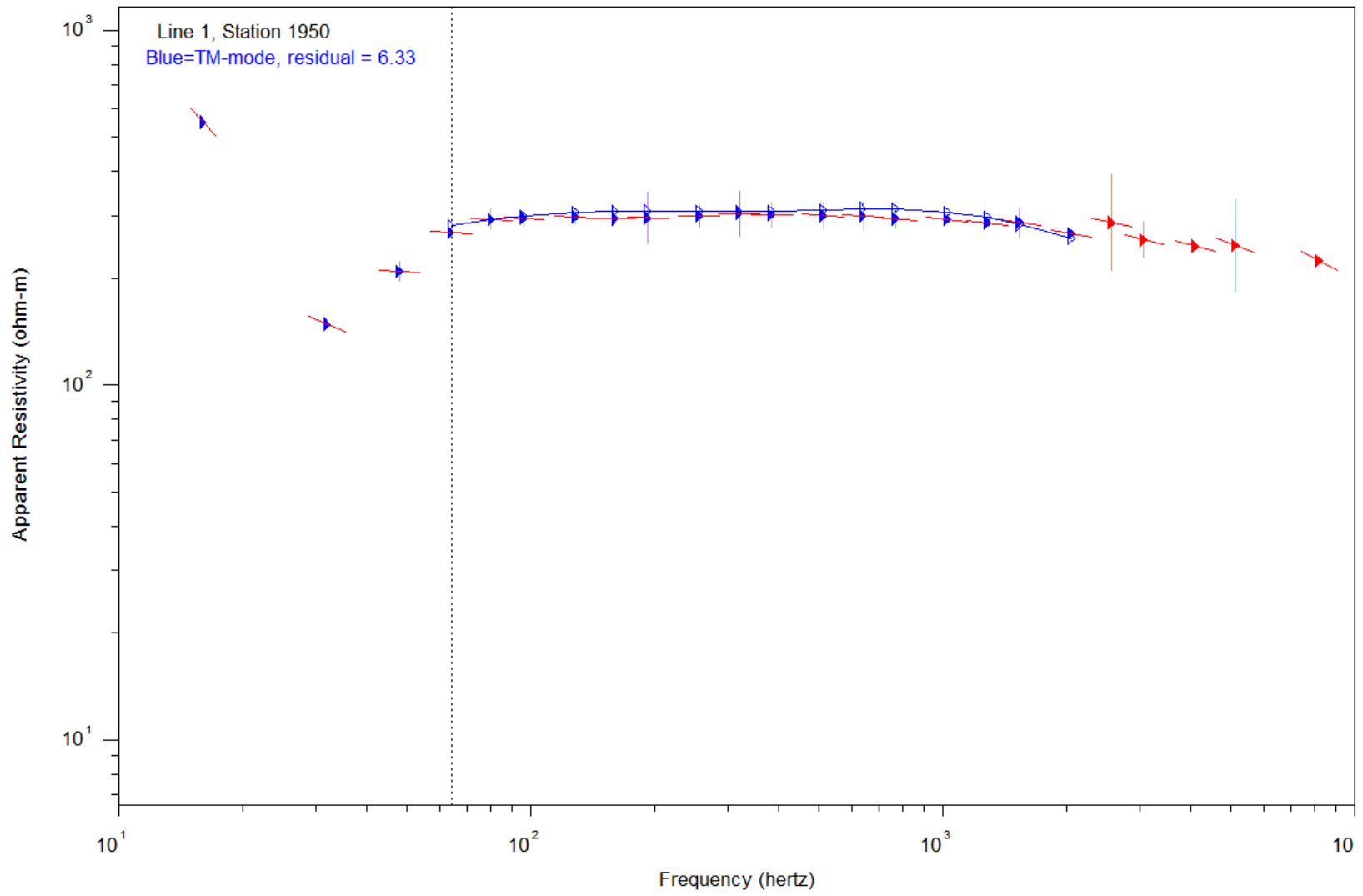
Appendix 4.36 : Inversion model from averaged data. Line 1 North, Dipole 150 best-fit model.

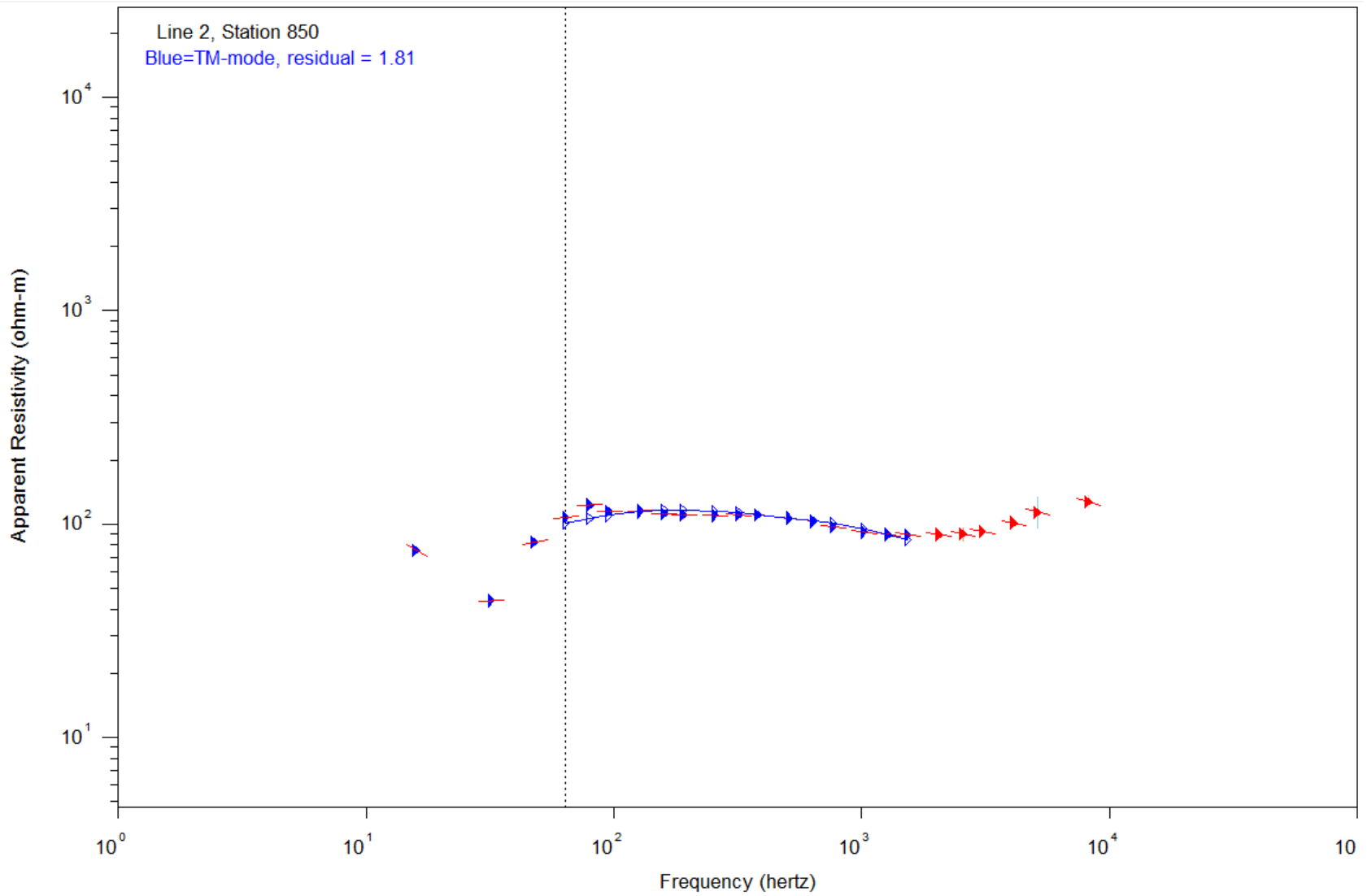Appendix 4.37 : Inversion model from averaged data. Line 2 pseudo cross-section.

Appendix 4.38 : Inversion model from averaged data. Line 2, Dipole 0050 best-fit model.

Appendix 4.39 : Inversion model from averaged data. Line 2, Dipole 0150 best-fit model.
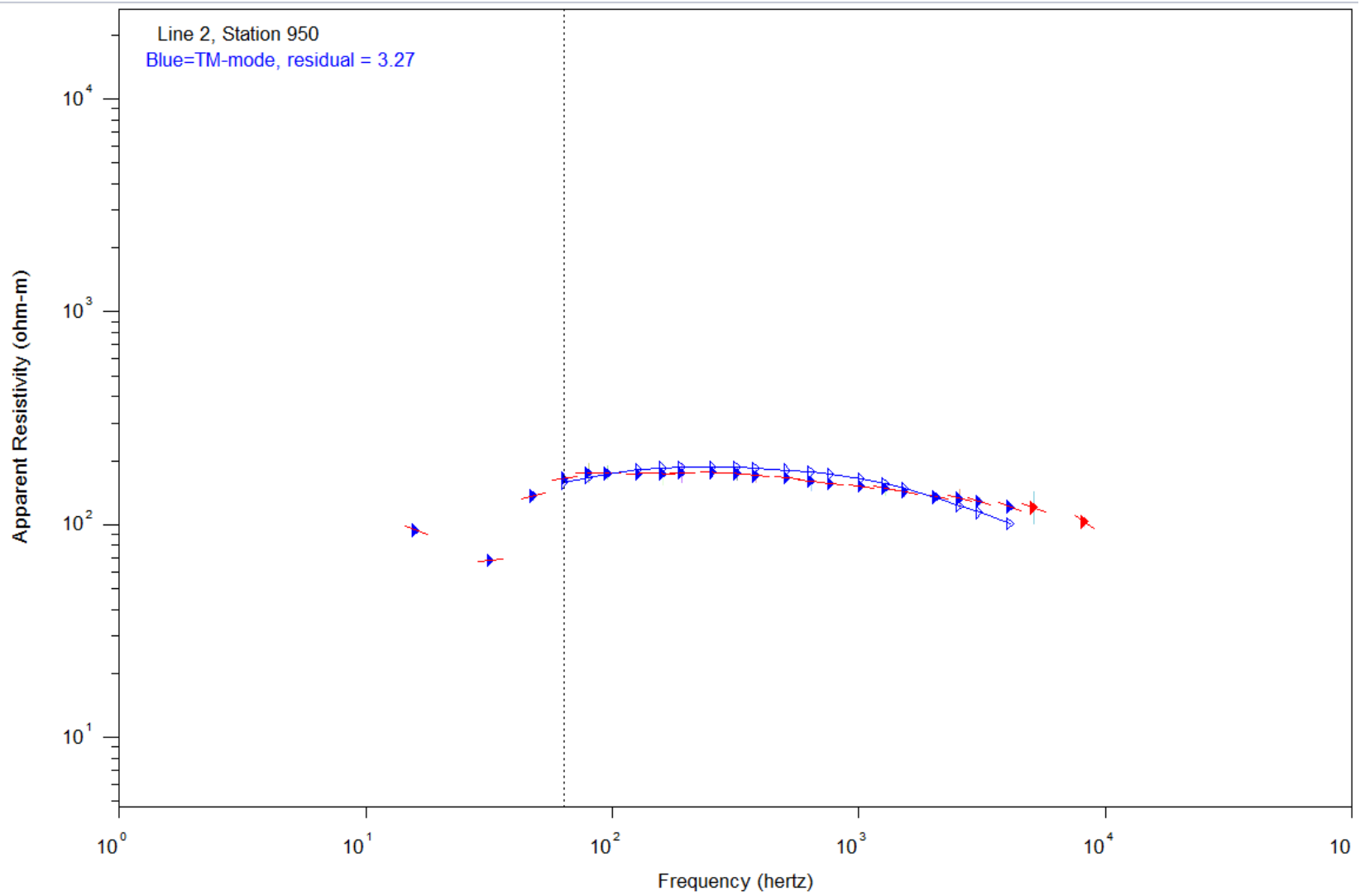
Line 2, Station 250
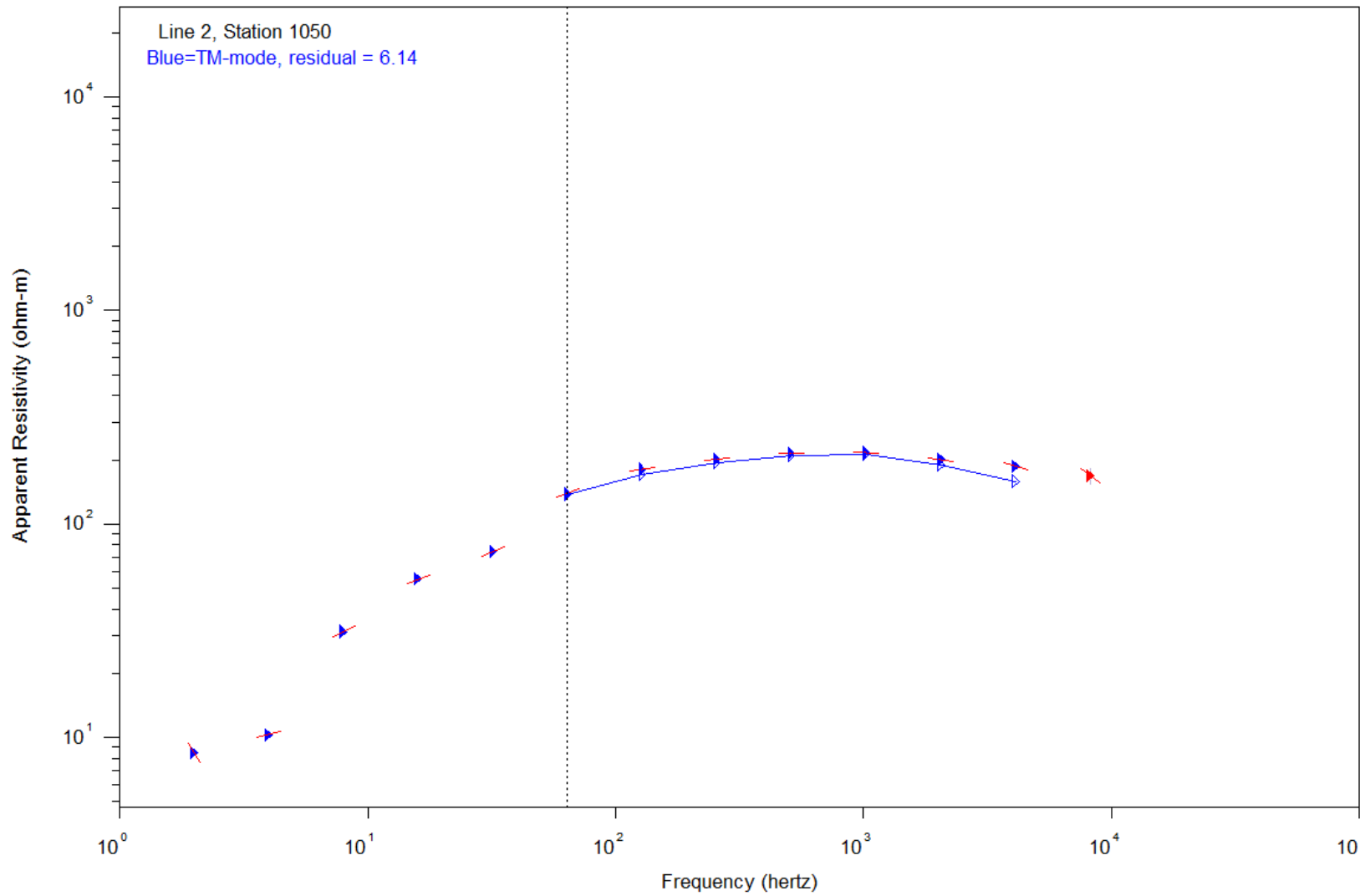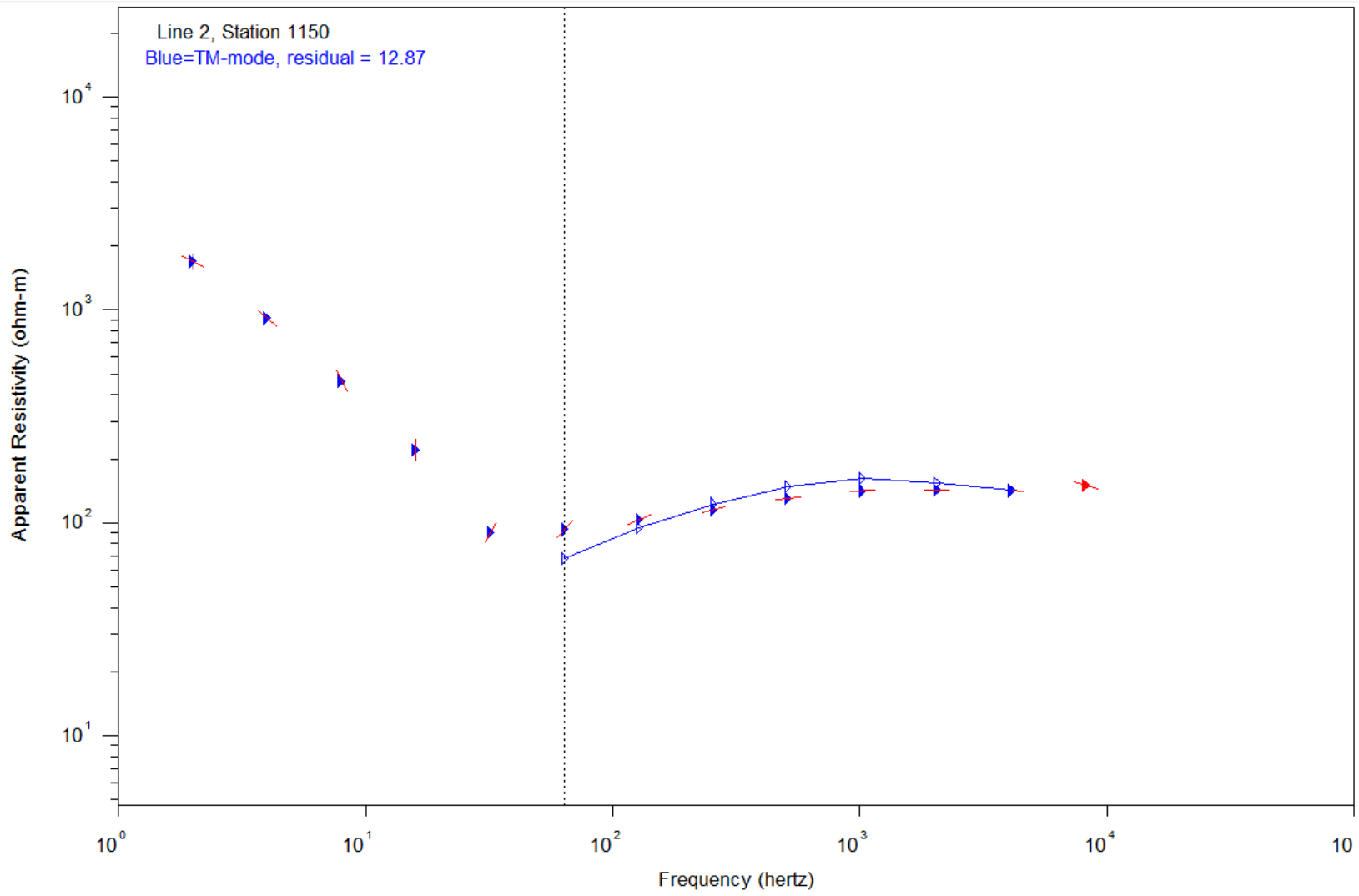Blue=TM-mode, residual = 2.54

Appendix 4.40 : Inversion model from averaged data. Line 2, Dipole 0250 best-fit model.

Appendix 4.41 : Inversion model from averaged data. Line 2, Dipole 0350 best-fit model.
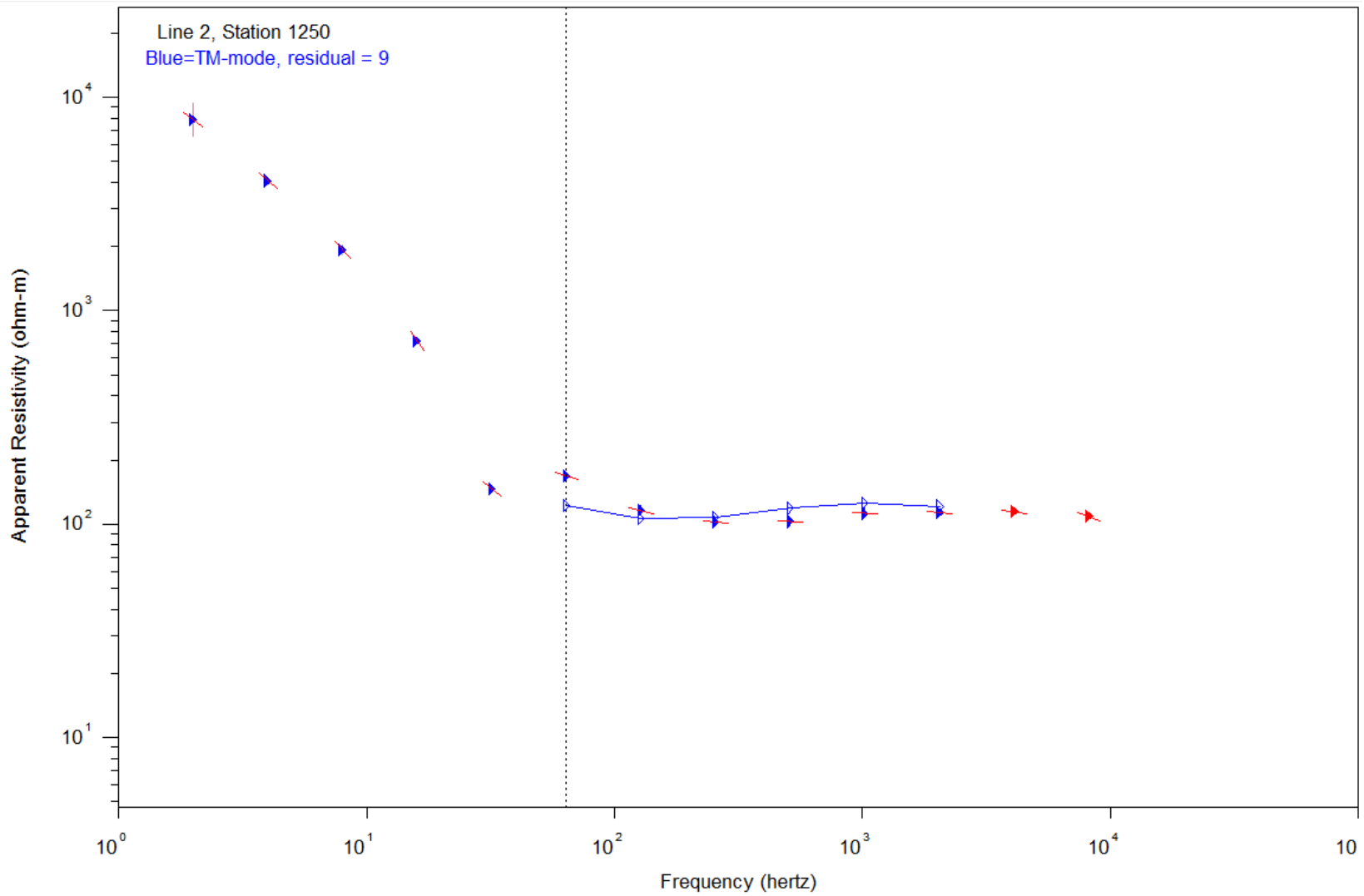
Appendix 4.42 : Inversion model from averaged data. Line 2, Dipole 0450 best-fit model.

Appendix 4.43 : Inversion model from averaged data. Line 2, Dipole 0550 best-fit model.

Appendix 4.44 : Inversion model from averaged data. Line 2, Dipole 0650 best-fit model.

Appendix 4.45 : Inversion model from averaged data. Line 2, Dipole 0750 best-fit model.

Appendix 4.46 : Inversion model from averaged data. Line 2, Dipole 0850 best-fit model.

Appendix 4.47 : Inversion model from averaged data. Line 2, Dipole 0950 best-fit model.
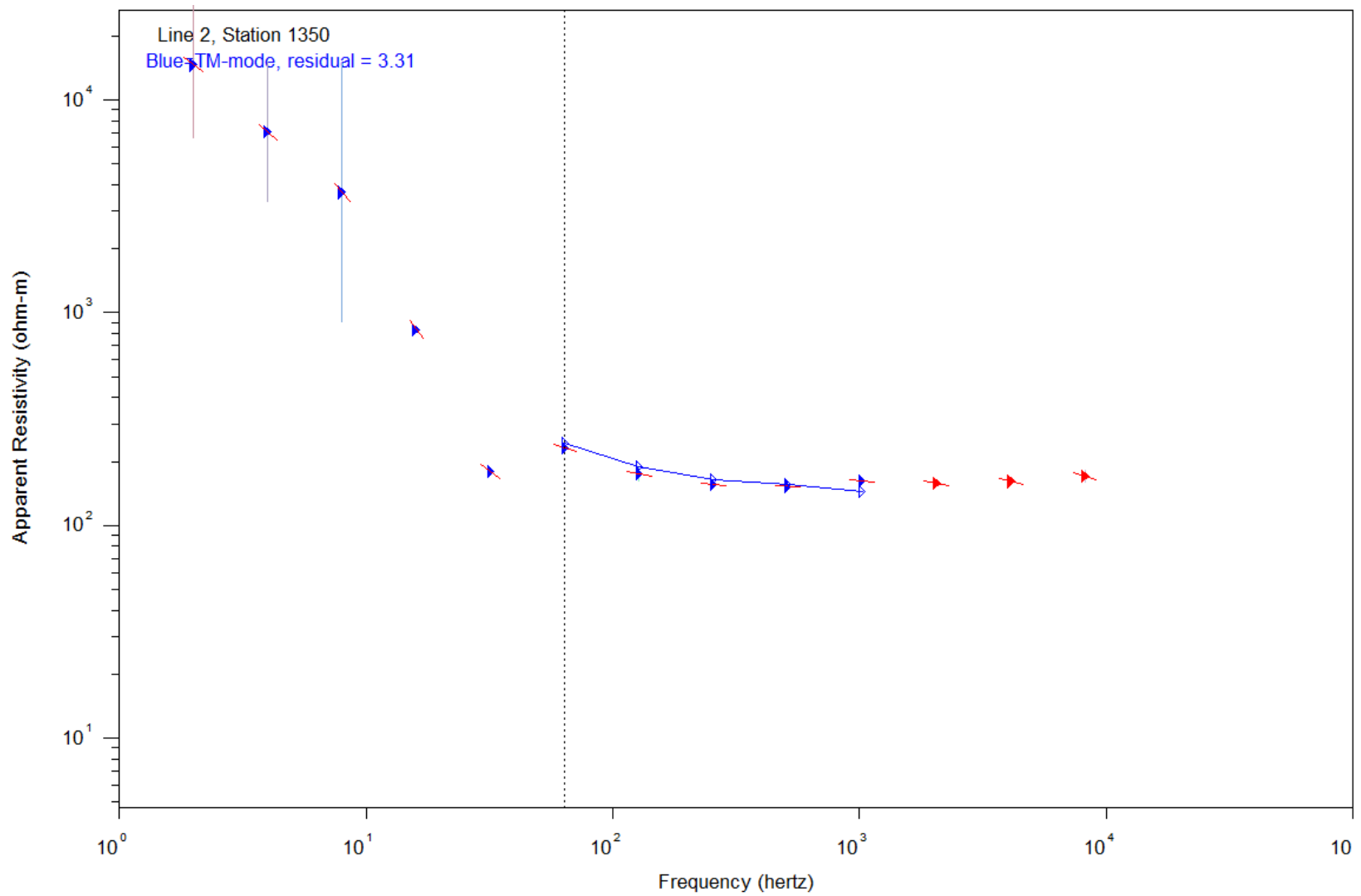
Appendix 4.48 : Inversion model from averaged data. Line 2, Dipole 1050 best-fit model.
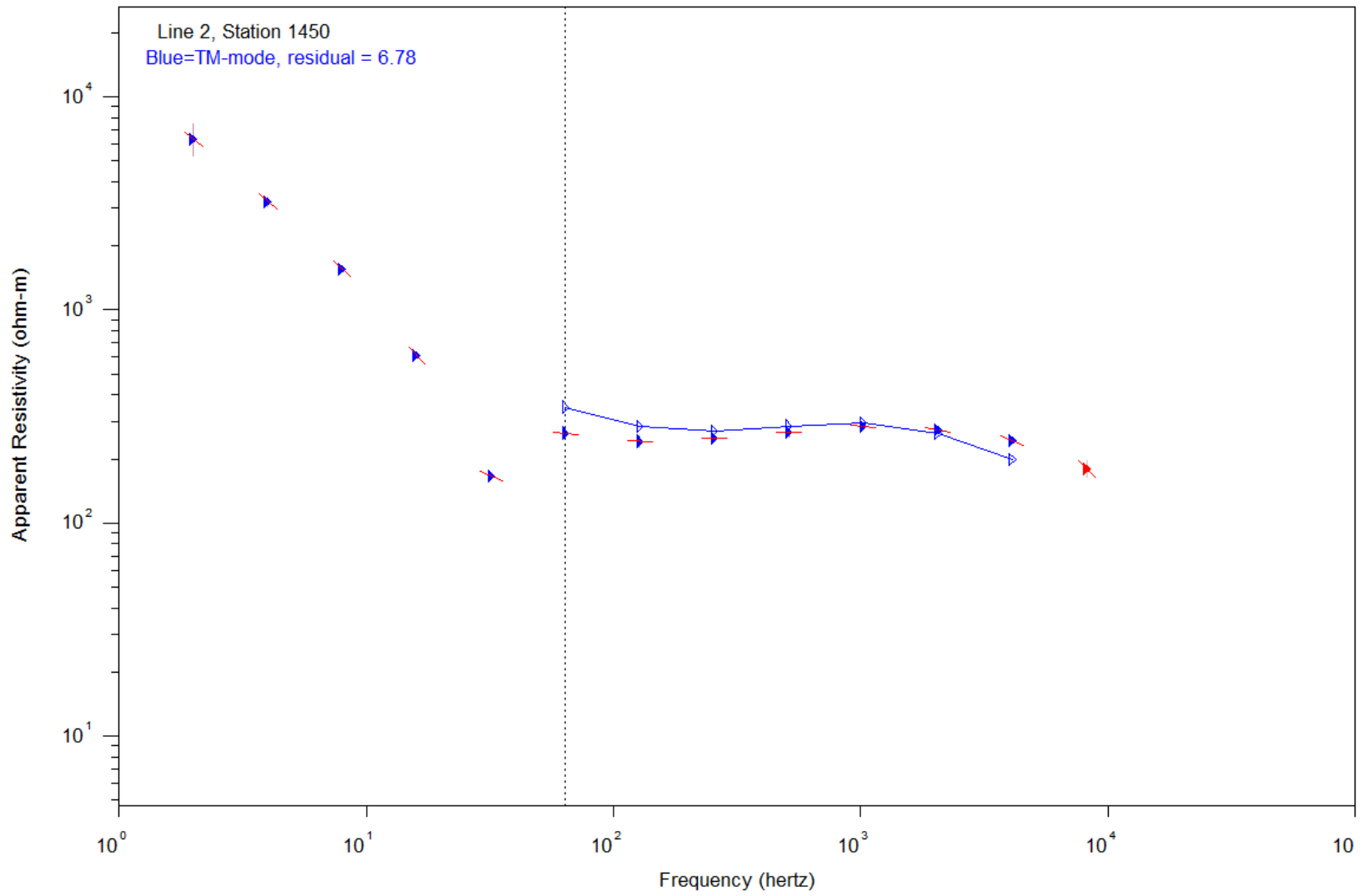
Appendix 4.49 : Inversion model from averaged data. Line 2, Dipole 1150 best-fit model.

Appendix 4.50 : Inversion model from averaged data. Line 2, Dipole 1250 best-fit model.

Appendix 4.51 : Inversion model from averaged data. Line 2, Dipole 1350 best-fit model.

Appendix 4.52 : Inversion model from averaged data. Line 2, Dipole 1450 best-fit model.